TM NT 0110

Effect of Natural Ventilation of Internal Boundary Layer on the Flow Characteristics of a Supersonic Air-Intake

RITU KANCHAN DUBEY, G K SURYANARAYANA
National Trisonic Aerodynamic Facilities

Technical Memorandum NT 0110
June 2010

National Aerospace Laboratories
(Council of Scientific & Industrial Research)
Bangalore 560 017, India

Effect of natural ventilation of internal boundary layer on the flow characteristics of a supersonic air-intake

Ritu Kanchan Dubey and G. K. Suryanarayana

SUMMARY

Experiments were carried out on the model of an isolated supersonic air-intake to study the effect of natural ventilation of the internal boundary layer on the overall pressure distribution, total pressure recovery, intake buzz oscillations and surface-flow patterns in the Mach number range of 2 to 3 at design and off-design conditions. The intake was stared in supercritical condition with benign back-pressure condition; the back-pressure was gradually increased using a butterfly valve driven by a PC-controlled stepper motor. The tests were carried out at the 0.3m supersonic blowdown wind tunnel at the Experimental Aerodynamics Division, NAL, Bangalore. The results show that with ventilation, significant improvement in the total pressure recovery occurs at all back-pressure conditions, with the optimum vent gap of 1.6mm indicating improvement in the pressure recovery efficiency from about 60% to 90% at Mach 3; improvement was observed at Mach 2 also, though of reduced magnitude. Schlieren visualizations suggest a clear delay in the occurrence of critical condition of the intake. Ventilation created a stable oblique shock at the intake cowl lip, in contrast to the bow-wave without ventilation, indicating reduced spillage and improved pressure recovery of the entry flow. Image analyses of video pictures suggest a limit-cycle oscillation of the oblique shock just past the critical region. Numerical simulation for some selected cases was carried out with and without ventilation using a CFD code FLUENT. Reasonable agreement with the experimental data was observed.

CONTENTS

LIST OF SYMBOLS

A_e	:	Area of the exit of the intake (m^2)
A_{th}	:	Area of the geometric throat of intake (m^2)
C	:	Ports located on surface of the cowl
Cp	:	$(P-P_\infty)/Q$
Cp*	:	$(P^*-P_\infty)/Q$
DP	:	Ports located in the dump plane
e	:	Internal energy
F	:	Body forces
g	:	gravitational constant
I	:	Unit tensor
k	:	Kinetic energy of turbulence
$\dot{m}$	:	Mass Flow Rate (Kg/sec)
$\dot{m}_{max}$	:	Maximum Mass Flow Rate (Kg/sec)
M	:	Mach Number
M_∞	:	Free-stream Mach Number
p	:	Static Pressure (psi/ N/m^2)
P_∞	:	Free-stream Static Pressure (psi; N/m^2)
P_S	:	Static Pressure (psi; N/m^2)
P_o	:	Total Pressure (psi; N/m^2)
$P_{o\infty}$	:	Free-stream Total Pressure (psi; N/m^2)
P*	:	$0.5283*P_o$
PR_m	:	Total pressure Recovery measured at 120mm downstream from the cowl Lip, ($P_o/ P_{o\infty}$)
PR_{max}	:	Maximum total pressure Recovery downstream of terminal shock
PR	:	Ports located for pressure recovery measurement
Pi	:	Inlet pressure
Pb	:	Back pressure
Q	:	Dynamic pressure, $0.7*P*M^2$
R	:	gas constant
RM	:	Ports located on surface of the ramp
RS	:	Ports located along the surface of the sideplate

t	:	time derivative
T	:	Static Temperature (°K)
T_∞	:	Free-stream Static Temperature (°K)
T_o	:	Total Temperature (°K)
$T_{o\infty}$	:	Total Temperature (°K) of the free stream
u	:	x-component of velocity
v	:	y-component of velocity
V^T	:	Volume dilation
V	:	Voltage (Volts)
V_∞	:	Free stream Velocity (m/sec)
w	:	z-component of velocity
x	:	x-derivative
X	:	Distance on the surface along flow direction
y	:	y-derivative
z	:	z-derivative
Z	:	Distance on a surface perpendicular to flow direction
ε	:	Dissipation rate
ε_d	:	Mass flow ratio
γ	:	Specific heat ratio
η_d	:	Efficiency of diffuser
η_{PR}	:	Efficiency of pressure recovery
μ	:	Molecular viscosity
μ_t	:	Turbulent viscosity
μ_l	:	Laminar viscosity
θ	:	Angular position of exit valve (deg); 0° - full open; 90° - full closed
ρ_∞	:	Free-stream density (Kg/m^3)
ρ	:	Density (Kg/m^3)
τ	:	Stress tensor

1.0 Introduction

Development of air-breathing propulsion systems is gaining importance in atmospheric flight of launch vehicles to improve the payload fraction. One of the important factors in such systems is the supersonic air-intake design. The air-intake is required to deliver the required amount of mass-flow rate through the intake with the maximum total pressure recovery. For operations at high supersonic Mach numbers, it is always preferred to design the intake ramps to produce finite number of oblique shocks to minimize total pressure losses. Since the shock angle varies with the free stream Mach number, an adjustable ramp, whose turning angle decreases with Mach number so that the ramp shock glances the cowl lip at all Mach numbers is often preferred. It is also essential that the air-intake operates in the supercritical to critical range of operations so that the entry flow remains supersonic at all flight Mach numbers and does not result in unstart, especially when heat and mass addition take place due to combustion downstream of the intake throat. However, the viscous flow developing from the ramp leading edge, the side plates and the intake cowl experiences different initial conditions, pressure gradients, etc, leading to development of secondary flows, corner eddies, etc., along the streamwise direction. Consequently, the real flow tends to become 3-dimensional, depending on the geometrical characteristics such as the height to width ratio, length of the air-intake, etc. Experiments are essential to study the intake performance and to develop suitable strategies for boundary layer control to optimize the intake performance over the range of flight Mach numbers.

Supersonic air-intakes

The basic knowledge available from standard literature about the fundamental operations of the supersonic intakes is summarized below.
Supersonic intakes may be grouped under internal compression, external compression and mixed compression intakes. Internal compression intakes are those in which compression takes place inside the intakes. In external compression intakes, compression takes place outside the intake with help of a wedge or cone, more often known as ramps. In mixed compression intakes the compression is partially inside and partially out side of the intake. Enormous information on the basic performance of intakes can be found (Ref. 1-3). For low supersonic Mach numbers, a pitot intake (also known as single-shock intake) is often used. As the flight Mach number increases, such intakes become more and more inefficient because of occurrence of a normal shock at the intake entry. However, this simple mechanical design is highly suitable for $1 < M < 1.5$. Fig 1.1 and 1.2 show schematic of typical pitot intakes and the performance curve for various modes of operation. Depending on the back-pressure, these intakes exhibit supercritical, critical or sub critical mode of operation. Fig 1.3 shows a typical variation of pressure recovery with Mach number for 1-shock, 2-shock, 3-shock and multi shock intakes. It may be noted that for a pitot intake, the pressure recovery reduces drastically with increase in Mach number, especially for $M > 1.5$. It may also be observed that the pressure recovery increases with Mach number, as the number of oblique shocks increases. Hence, multi shock intakes at higher supersonic Mach numbers are chosen for better performance. It is well known from theory of oblique shocks that compression through a number of oblique shocks is an isentropic process. However, isentropic

intakes are not practical since the intake ramp becomes too long, resulting in heavier mass, viscous losses, etc. Hence, the intake design must consider a finite number of oblique shocks.

A rounded cowl lip causes a bow-wave and hence large losses. Therefore, the cowl lip is normally a sharp wedge to generate an oblique shock. Schematic of such an intake is shown in Fig 1.4. The ramp shock is followed by a normal shock leading to subsonic flow downstream through the intake. The oblique shock generated at the ramp is a function of the free stream Mach number and the turning angle at the ramp leading edge. During the off-design condition ($M_\infty < M_{design}$), the capture area increases with increase in Mach number and shock angle reduces until the ramp shock glances the lip, as shown in Fig 1.5. Effect of flight Mach number on oblique shock intake and its capture area variations with Mach number is shown in Fig 1.5. The various modes of operation of a supersonic air-intake designed for subsonic combustion are schematically illustrated in Fig. 1.6.

In supersonic intakes designed for subsonic combustion, the oncoming flow is decelerated to the desired condition in a subsonic diffuser downstream of the throat, through a weak normal shock, or a terminal shock. The position of this terminal shock is governed by the back-pressure at the exit of the intake. At the critical condition, the terminal shock (occurring at Mach 1 and hence minimum total pressure loss) moves upstream from the diffuser and locates itself at the throat, resulting in the maximum pressure recovery. In the super-critical condition, the normal shock occurs in the subsonic diffuser at a higher Mach number (>1), resulting in reduced pressure recovery. In the sub-critical condition, the terminal shock is expelled out of the intake, giving rise to reduced mass flow through the intake due to subsonic spillage over the lip. Typical variation of total pressure recovery for various modes of operation is shown in Fig. 1.7.

Concept of natural ventilation

Control of internal boundary layer alleviates some of the adverse effects associated with the internal flow (Ref. 2-5). The well known methods of boundary layer bleed make use of perforated plates or slots for blowing or suction using active or passive flow-control [4]. However, these techniques are better suited for long endurance flight at the design Mach number. For short duration missions of launch vehicles and missiles, the existing methods have the following limitations:

- For effective bleed, the bleed holes must be properly aligned with respect to the mean flow on the ramp/cowl. They must have diameters typically of the order of the local boundary layer displacement thickness.
- At high Mach numbers and high altitudes (hypersonic conditions), the boundary layer becomes very thick, leading to reduced aerodynamic throat, thereby requiring increasing amounts of bleed as a function of Mach number.
- Higher stagnation temperatures require the use of heat resistant hoses to duct the bled mass out of the intake.
- The manner in which the bled mass is released out of the intake can have a major influence on the external drag of the vehicle.

- The overall benefits gained by bleed may be easily offset by the internal drag associated with the ducting, increased overall mass and increased external drag.
- In most cases, the ramp is actively controlled through linkage mechanisms located underneath the ramp. Operation of the linkage mechanism without interference with the bleed ducts requires use of the flexible hoses to lead the viscous flow out of the intake.

In order to overcome these practical problems, a concept of passive boundary layer control, termed *natural ventilation*, has been attempted in the present work. The effects of natural ventilation on the flow past spheres have been reported by Suryanarayana, et al (Ref. 5-7). A recent book reports the effects of natural ventilation on bluff bodies (Suryanarayana Ref. 8). In the range of supercritical Reynolds numbers, natural ventilation reduced the drag of a sphere by nearly 70% by increasing the base pressure of the sphere. A strong coupling between the internal vent flow and the external flow, which carry opposite vorticities, caused the base pressure increase and consequent drag reduction.

Natural ventilation of supersonic air-intake

In this concept, the internal boundary layer of the intake is vented to the outer flow through a small vent (gap) obtained by displacing the side-walls away from the assembly of the cowl and ramp by introducing spacers of desired thickness, as shown in Fig 1.8; the gap can be varied by controlling the thickness of the spacers. This arrangement results in gaps at all the four corners between the ramp, side plate and cowl. In a supersonic flow, disturbances can propagate upstream only through the subsonic part of the boundary layer. Proper setting of the vent gap sweeps away a good portion of the subsonic flow from the side wall boundary layer and the corner vertices. Some regions of the boundary layers growing on the ramp and cowl are also bled out because of the favorable span wise pressure gradient created by the gap. This renders the supersonic part of the flow to be more stable and offers better resistance to intake buzz. Since the internal flow (after the shocks) always has a higher pressure compare to external flow, the pressure difference drives the flow out of the intake. The vent-exit geometry in the present case may be expected to result in a jet-like flow exiting from the vent gaps at the side-walls and thereby cause incremental external drag, calling for proper shaping of the exit path, (like a wall-jet). Hence, aerodynamic force measurements with vented air-intake are essential to assess the true performance of the intake. However, since improvement in both mass flow rate as well as pressure recovery is indicated, improvement in overall performance with natural ventilation is expected.

2. Project details

TITLE:	Studies on supersonic air-intakes
PROJECT No.:	N - 8 - 496
SPONSOR:	NAL, Bangalore
OBJECTIVE:	Study the effects of natural ventilation of a supersonic air-intake
FACILITY:	0.3m tunnel, NAL
MACH No.:	1.8 to 3.0

3. Test facility

The experiments were carried out in the 0.3m X 0.3m trisonic wind tunnel of Experimental Aerodynamic Division at NAL. This is an intermittent blow-down type facility, capable of Mach number range 0.5 to 4.0. Supersonic flow is achieved in the test section using a pair of solid block nozzles. Subsonic Mach number can be achieved by choking the second throat in the wind tunnel. Slotted wall test section with diffuser flaps is used to generate transonic Mach numbers. Based on the requirements, model can be sting-mounted, base-mounted as well as side-wall mounted. The angle of attack can be changed during the run with the help of a hydraulic pitch control system. Reynolds number can be achieved from 60 to 80 X 10^6 per meter by varying the total pressure. A schematic of the tunnel is shown in Fig 3.1. In the present studies, all the tests were carried out at supersonic Mach numbers with the model at angle of attack of 0°. Details of the tests carried out are given in table 3.1. More details of the 0.3m wind tunnel are given in Ref. 9.

4. Model details

The model is modular in construction, comprising two interchangeable ramps for Mach 2 and 3. The ramps are designed such that oblique shocks generating from the ramps glance the fixed cowl lip at the respective free stream Mach numbers of 2 and 3. The model has a cowl, a bottom plate and two side plates. The intake flow beyond the throat is smoothly turned downstream across a dump plane. A total pressure rake is placed at the dump plane. A suitable curvature is provided downstream of the throat along the cowl and bottom plate. The intake extends beyond the dump plane with a constant area and terminates in rectangular section at the exit. A rectangular butterfly valve is fitted at the intake exit to vary the exit area. The model is mounted on a specially constructed base plate. The base plate, along with the assembled model is fixed in the test section. Sketches of the Mach 2 and Mach 3 ramps assembled with cowl, side-plates, model base and exit valve are shown in Figs 4.1 and 4.2. Geometric throat of the intake is located at a distance of 50mm from the cowl lip.

Butterfly valve at exit region

Exit of the intake terminates in a rectangular section of dimensions 37.5mm X 74.5mm. The exit area can be varied using a DC stepper motor driven butterfly valve of dimensions of 37mm X 74.0mm X 4mm. The valve is connected to a shaft, which is linked to a reduction gear box with the help of suitable coupling. Valve at $\theta = 0^\circ$ with respect to pitch plane of the intake is considered results in maximum exit area (most benign condition of back pressure). Valve at $\theta = 90^\circ$ with respect to pitch plane of the intake corresponds to fully closed condition (most adverse condition of back pressure). A schematic of the intake exit valve is shown in Fig 4.3. A photograph of the complete assembled model mounted in tunnel with one side opened is shown in Fig 4.4, along with the locations of all the total pressure ports. Exit area control mechanism is shown in Fig 4.5. Motor is placed at the bottom of the tunnel.

Exit Area (Back-Pressure) Control

Fig. 4.6 shows the variation of exit area ratio (A_e/A_{th}) with exit valve rotation angle for both the ramps. The ratios for Mach 3 ramp are greater as compared to that of Mach 2 ramp because of lower throat area at Mach 3. It may be noted that the area ratio reaches a value of 1.0 in the range of $0^\circ \leq \theta \leq 25^\circ$ for the Mach 2 ramp and in the range $0^\circ \leq \theta \leq 40^\circ$ for the Mach 3 ramp. During the wind tunnel tests, the intake was started with the exit valve in full open position (supercritical condition) and gradually closed to obtain critical and subcritical conditions.

5. Instrumentation

5.1 DC Stepper motor and gearbox

A DC stepper motor was used for exit area control. The motor is of permanent magnet hybrid type. It is a bifilar wound, two phase bipolar with eight salient poles and a toothed iron rotor. The rotor is suspended in the stator by means of sealed ball bearings. All parts of the motors are precisely machined for good performance and accuracy of steps. Step angles are $1.80^\circ \pm 0.10^\circ$ non-cumulative. The motor has holding torque of 28 Kg-cm. Insulation is used to avoid heating of the motor parts. For better heat dissipation motor is also duly fitted with heat sinks.

In a stepper motor, the stepping rate (speed of rotation) of the motor is governed by frequency of switching pulses. A single pulse moves the motor shaft by one step only. Thus, number of steps can be precisely controlled by number of input pulses using a PC. When there is no pulse input, the rotor will remain locked in the last step. The motor can be programmed through three parameters viz., direction, speed and number of steps. There is no wear and tear since the motor is brush-less. Load and no load conditions make no difference in running currents of the motor. The gearbox is of reduction ratio 1:15. Bench tests were carried out on the motor-gearbox assembly under maximum torque conditions at the gearbox output shaft. The motor was driven through controlled number of pulses in the specified sequence. Rotation of the gear box output shaft was measured using a digital inclinometer. The motor operates at 200 pulses per revolution, corresponding to 1.8° per step. In conjunction with the reduction gear box, the rotation of the butterfly valve is 0.12° per pulse, which is quite adequate for the present studies. The motor was operated in a closed loop operation mode for accurate control. To get the feedback, the motor shaft is connected to a pair of anti-backlash gears to drive a 10-turn potentiometer. The output of the potentiometer is calibrated and used to determine the valve position during the run. The complete details of the control set-up are given below. Figs 5.1 – 5.3 show a block diagram and flow charts of the complete control set-up.

5.2 Calibration of butterfly shaft rotation

The shaft of the stepper motor is connected to a pair of anti-backlash gears, involving a gear of 260 teeth and a matching gear of 72 teeth, matched to a 10 turn potentiometer. As shaft rotates, anti-backlash gear along with matching gear starts rotating and hence potentiometer rotates. The output from the potentiometer is calibrated against the valve angle. This calibration is used to drive the motor to the

required exit area. The calibration of the valve rotation with the output from potentiometer is shown in Fig 5.4. Sensitivity of the angle was found 0.0049V/deg. A typical history of set angle and achieved angle during the blow down is given in Table 5.1.

5.3 Instrumentation, Data Acquisition and Reduction

Pressures were measured simultaneously at 73 locations in the model, using 5 ESP scanners. For static and total pressure measurements, 5 numbers of 16-port scanners of range ±15psid were used up to Mach 2.0. At higher Mach numbers, 1 scanner of range ±30psid was used for total pressure measurements. The length of the tubes of the connection from model port to the scanner port is about 1.5m. The mapping of model port to scanner port is given in Table 5.2 and 5.3. A special program was developed using MATLAB to analyze the data obtained. The data acquisition system of 0.3m WT at EAD, NAL, based on National Instruments was used. Calibration of the scanners was carried out using NI based labVIEW software. The acquisition system includes signal conditioning, data reduction and online calibration. Block diagram of pressure data acquisition is shown in Fig 5.5.

The tunnel static pressure was measured at nine locations along the wall of the test section using +/-15Psid transducers. The total pressure was measured in the settling chamber using +/-15Psid and +/-150Psia transducers.

6. Numerical simulations

A description of numerical simulation through the intake used in experiments is presented. The simulation methodology, governing equations, convergence criteria and boundary conditions are included in this section.

6.1 Computational study

Supersonic 3D viscous flow through the intake was studied numerically using a commercial CFD package FLUENT. The conservation equations of mass, momentum and energy were solved through this solver using finite volume approach. The governing equations were solved simultaneously using second order discretization and coupled implicit solver. The intake geometry was created in Gambit and solution carried out for M = 3.0 with basic configuration and with 1.6mm vent gap. The computational domain was created into different volumes and later merged in to a single volume. Half of the geometry of the intake about the vertical plane was modeled and symmetry condition was applied to achieve the complete geometry. The complete volume was discretized into 4.5 lakh cells. This grid was adapted within the interested area of shock locations within the intake. This gave a total number of cells of about 10 lakh. The first node of the grid was at a distance of $2x10^{-3}$ mm from the wall. The grid was made coarser above the cowl region and further coarser away from the cowl top wall in the perpendicular direction to minimize the computations. A successive ratio of 1.05 was used for gradual increment of the distance between the two nodes. A view of simulated geometry is shown in Fig. 6.1. The back pressure at the intake exit was imposed by defining a patch volume. The computational geometry and grid through the model at the symmetry is shown in Fig.

6.2 and Fig 6.3. Before arriving at final computation domain, selection of grid was made for 2D simulation after examining several grids. The results obtained for all the grids were compared and based on the comparison one grid was chosen. Selection of turbulence model was performed by studying the computation with k-ε, Spallart-Allamaras and k-ω model. It was observed that results obtained do not differ significantly with the turbulence model used. Hence, all the studies were carried out using k-ε model.

6.2 Assumptions

The following assumptions have been made while formulating the governing equations to simplify the analysis procedure:

- The flow is considered to be 3D, hence cowl and ramp and side plate of the intake geometry is considered for simulation. The complete experimental model of the intake was simplified.
- Air was taken as working fluid, treated as ideal gas.
- Transport properties of the fluid are considered to be constant at every point in the computational domain.
- Gravitational effects are negligible.
- Steady operation of the intake was considered in most of the runs.

6.3 Governing Equations

Conservation equations for mass and momentum and energy were solved. Additional transport equations were also solved when the flow is turbulent.

Mass conservation Equations

The equation for conservation of mass for compressible flows can be written as:

$$\frac{\partial \rho}{\partial t} + \nabla.(\rho V) = 0$$

Where ρ is the density and V is the velocity vector.

Momentum Conservation Equations

Conservation of momentum in an internal reference frame can be described as:.

$$\frac{\partial(\rho V)}{\partial t} + \nabla.(\rho VV) = -\nabla p + \nabla.(\bar{\bar{\tau}}) + \rho\vec{g} + \vec{F}$$

$$\frac{\partial(\rho u)}{\partial t} + \nabla.(\rho u V) = -\frac{\partial p}{\partial x} + \frac{\partial}{\partial x}(\lambda \nabla.V + 2\mu\frac{\partial u}{\partial x}) + \frac{\partial}{\partial y}\left[\mu(\frac{\partial v}{\partial x} + \frac{\partial u}{\partial y})\right] + \frac{\partial}{\partial z}\left[\mu(\frac{\partial u}{\partial z} + \frac{\partial w}{\partial x})\right]$$

$$\frac{\partial(\rho v)}{\partial t} + \nabla.(\rho v V) = -\frac{\partial p}{\partial y} + \frac{\partial}{\partial x}\left[\mu(\frac{\partial v}{\partial x} + \frac{\partial u}{\partial y})\right] + \frac{\partial}{\partial y}(\lambda \nabla.V + 2\mu\frac{\partial v}{\partial y}) + \frac{\partial}{\partial z}\left[\mu(\frac{\partial w}{\partial y} + \frac{\partial v}{\partial z})\right]$$

$$\frac{\partial(\rho w)}{\partial t} + \nabla.(\rho w V) = -\frac{\partial p}{\partial z} + \frac{\partial}{\partial x}\left[\mu(\frac{\partial u}{\partial z} + \frac{\partial w}{\partial x})\right] + \frac{\partial}{\partial y}\left[\mu(\frac{\partial w}{\partial y} + \frac{\partial v}{\partial z})\right] + \frac{\partial}{\partial z}(\lambda \nabla.V + 2\mu\frac{\partial w}{\partial z})$$

where, $\lambda = -\frac{2}{3}\mu$

here $\mu = \mu_l + \mu_t$

μ_t is related to the kinetic energy of turbulence(k) and its dissipation rate (ε) as

$\mu_t = \frac{C_\mu \rho k^2}{\varepsilon}$ and

$C_\mu = 0.09$

Body forces and gravitational forces are neglected in the present studies. For steady and viscous flow this equation can be expanded as

$$\bar{\bar{\tau}} = \mu\left[(\nabla\vec{V} + \nabla\vec{V}^T - \frac{2}{3}\nabla.\vec{V}I\right],$$

I is the unit tensor and the second term to the right hand side is the effect of volume dilation.

Equation of state:

$p = \rho RT$

Energy Equation

$$\rho\frac{D(e+V^2/2)}{Dt} = \rho\overset{*}{q} + \frac{\partial}{\partial x}\left[k\frac{\partial T}{\partial x}\right] + \frac{\partial}{\partial y}\left[k\frac{\partial T}{\partial y}\right] + \frac{\partial}{\partial z}\left[k\frac{\partial T}{\partial z}\right]$$

$$-\nabla.pV + \frac{\partial(u\tau_{xy})}{\partial x} + \frac{\partial(u\tau_{yz})}{\partial y} + \frac{\partial(u\tau_{zx})}{\partial z} + \frac{\partial(v\tau_{xy})}{\partial x} + \frac{\partial(v\tau_{yz})}{\partial y} + \frac{\partial(v\tau_{zx})}{\partial z} + \frac{\partial(w\tau_{xy})}{\partial x} + \frac{\partial(w\tau_{yz})}{\partial y} + \frac{\partial(w\tau_{zx})}{\partial z}$$

6.4 Boundary Conditions

$v = 0$

$w = 0$

The details of boundary conditions are shown in Fig 6.1.

Pressure far-field condition:

The test section static pressure, Mach number and Temperature were specified. The free stream conditions are the same as in the wind tunnel, shown in Tables 6.1 and 6.2. Tunnel total temperature was considered as 298K.

Outlet conditions:

The free stream pressure and total temperature were specified upstream of the model. For subsonic flow at the exit of the inlet, known back pressure was specified. Apart from pressure at the intake exit, roughly estimated by velocity at the intake exit was also imposed by considering the mass flow rate.

Wall:

At the cowl wall and ramp wall, no-slip conditions were imposed. Boundary conditions for the cases with ventilation are same as for the basic configuration. A vent is created between the cowl, ramp and side wall. Pressure outlet conditions were applied at the exit of the vent.

6.5 Convergence criterion

The criteria used was that the value of sum of the residue considered for the variables of mass, velocity, energy, k and ε < $1X10^{-6}$. Apart from the residue, the net

mass flow rate is also monitored where it reaches $\leq 1X10^{-3}$. In order to provide the stability to the iterations the courant number of 0.5 was used.

7a. Test programme

Table 7.1 gives summary of experiments carried out. In addition, oil flow tests at M = 1.8, 2.0, 2.5 & 3.0 at discrete area ratios and schlieren recordings of Buzz with and without ventilation using a high speed camera were also carried out at M = 3. Buzz visualization was carried out with a high speed Phantom v-series camera with a resolution of 800X600 pixels. Even though the camera is capable of capturing frames at a rate of about 6000 frames per second, in the present investigations speeds of 1000 to 2000 frames per second were found to be adequate.

7b. Results highlights

Before proceeding to the results obtained at the mentioned Mach number a summary of the expected pressure coefficients values is given in table 7.2 for comparison. Table 7.2 gives the theoretical pressure coefficient, obtained from oblique shock relation for the Mach numbers and wedge angles which are covered in the present investigation. Table 7.3 gives the theoretical pressure recovery values for a typical three shock system based on available literature.

7.1 Results on Mach 3 ramp

Pressure Measurements at M = 3.0; Effects of back pressure

Figure 7.1 shows the pressure distribution along the ramp in the range $2.72 \geq A_e/A_{th} \geq 0.65$: results from forward (F) and reverse (R) scans are included to bring out hysterisis effects. The pressure measured at first port on the ramp is in good agreement with the theoretical values (C_{P2}), as mentioned in Table 7.1 As shown in Fig. 7.1a, after the ramp shock, even though one would expect a constant pressure corresponding to the turning angle at the ramp, the pressure on the ramp increases along the downstream direction and reaches a pressure peak just upstream of the throat. The pressure peak is followed by a rapid expansion of flow along the intake. The expansion terminates in a region of constant pressure ($0.07 < x < 0.12$), which might indicate separated flow. In the region $0.12 < x < 0.13$, a small pressure rise is noted at $A_e/A_{th} = 2.72$, possibly due to a weak terminal shock. This is followed by a constant pressure plateau along the rest of the flow channel, suggesting large-scale separation of flow. As A_e/A_{th} is reduced from 2.72 to 1.4 (Fig. 7.1a), systematic rise in strength of the terminal shock and upstream travel of the foot of the shock is seen from 0.13 to about 0.07m. The pressure levels in the pressure plateau also show systematic increase. Practically no change is seen in the pressure distribution on the ramp from the leading edge till the throat. As A_e/A_{th} is further reduced from 1.4 towards 0.65 (Fig. 7.1b), peak pressure in the intake occurs at $A_e/A_{th} = 1.2$. Further reduction in A_e/A_{th} clearly shows a reduction in the pressure in the intake, suggesting the occurrence of critical condition at $A_e/A_{th} = 1.20$. Increasing influence of the exit area reduction is seen along the ramp for $A_e/A_{th} < 1.4$, apparently because of the increasing thickness of the boundary layer. Hysterisis of static pressures in the separated flow, as expected, is clearly noted.

It seems likely that the pressure rise on the ramp is due to compression waves caused by the growing boundary layer, until the point of separation. Gradual thickening of the ramp boundary layer, as affected by shock-boundary layer interaction can result in compression waves. The interaction can also add to the adverse pressure gradient on the ramp, leading to flow separation.

Pressure distribution along the length of the cowl is shown in Fig 7.2a and 7.2b for $2.72 \leq A_e/A_{th} \leq 0.65$ when valve is operated in forward and reverse directions. Little evidence of hysterisis can be seen. The pressure distributions show insignificant changes for $2.72 \leq A_e/A_{th} \leq 2.5$. The pressure measured at the first port on the cowl is higher than that on ramp at same location, possibly due to the detached bow-shock ahead of the cowl leading edge. Drop in pressure along the flow direction is seen, possibly due to expansion fans. As seen in case of ramp, the accelerated flow beyond the throat, and pressure rise due to the terminal shock are noted. A pressure plateau around the throat region is clearly noticeable. The terminal shock moves upstream as the back pressure is increased, with the terminal shock close to the throat at $A_e/A_{th} = 1.2$; the static pressure levels are the highest at this area ratio.

Figs 7.3 and 7.4 show the static and total pressure distributions in the dump plane region along the side wall. At any area ratio, constant pressure plateau, suggestive of separated flow is noted. However, the pressure levels show a systematic rise up to $A_e/A_{th} = 1.2$ and then drop off, indicating the criticality of flow conditions, as observed on the ramp and cowl at this ratio; similar features are observed in the total pressure distributions across the dump plane as well (Figs. 7.4a and b).

Pressure measurements were carried out on the ramp along the centre line as well as along a side line away from the center. A comparison of the pressure distribution along these two locations is shown in Fig. 7.5 at $A_e/A_{th} = 2.72$ and 1. The pressure along the side is consistently lower than that along the center, suggesting a cross-flow across the ramp (hence 3-dimensionality), possibly aided by the separated flow. Fig 7.6 shows the pressure values across the ramp at a distance 39.75mm from cowl lip. Higher values of pressure are seen along the center as compared to those at the side.

To determine the critical area ratio accurately, the exit valve was varied in finer steps, providing reduced incremental area ratio of about 0.1. A typical variation of the pressure obtained near the critical range with smaller step size is shown in Fig 7.7 in the range $1.4 \leq A_e/A_{th} \leq 1$. Criticality is observed at $A_e/A_{th} = 1$, close to the value of 1.2 obtained from coarse scan. However, as shown in Fig 7.7b and 7.7c, distribution on the cowl and in the dump plane shows insignificant differences between are ratio of 1.1 and 1.2, indicating that criticality may not occur along all the components at the same back pressure condition.

Fig. 7.8 show the pressures measured on the ramp and the cowl at various area ratios at the section where the throat lies. C_p^* based on total pressure measurement downstream of the throat is also compared. Supersonic flow at the ramp and cowl is indicated at all the area ratios.

Effect of ventilation

Total pressure downstream of the throat was measured using three probes. The averaged data from these ports is used to calculate the mean pressure recovery in the intake, defined as the ratio of measured total pressure to that of the free stream.

$$PR_m = \frac{P_{om}}{P_\infty}$$

Efficiency of the pressure recovery may be defined by non-dimensionalizing the measured pressure recovery with the ideal theoretical value for a typical 3-shock intake.

$$\eta_{PR} = \frac{PR_m}{PR_{Th}}$$

The expected pressure recovery for a 3-shock intake system at different Mach numbers is given in table 7.3. Fig 7.9 compares the variation of pressure recovery efficiency with area ratio for various vent gaps and without any vent. It is noted that even a small vent gap shows significant improvement in pressure recovery at all back pressures. Out of the various vents tried, the optimum vent was 1.6mm, which shows a remarkable improvement in the efficiency from about 60% (unvented) to 91%, at the critical condition. Apart from this, overall rise in pressure on other surfaces of the configuration is observed with natural ventilation. Fig 7.10 compares the pressure distributions on the ramp, cowl, side-plate and dump plane at A_e/A_{th} =1.0, with and without ventilation. Interestingly, ventilation causes lower pressures on the ramp upstream of the cowl lip and increased pressures downstream of the intake, as compared to the unvented intake, which is the desirable performance from the intake. Higher pressures along the cowl, with ventilation are observed. Because of the vent, viscous effects and corner vertices are reduced from the intake, which helps to improve the intake performance. The measurements also suggest that flow through the intake is decelerated more efficiently with ventilation.

Fig. 7.11a shows Schlieren photographs for various A_e/A_{th} in the absence of ventilation. Interactions between oblique shock from the ramp, bow-shock at the cowl lip and oblique shock from the side plate are clearly seen in all the pictures. As the area ratio is reduced towards 0.85, a patch of orange shade, indicating buzz oscillations can be seen. As shown in Fig 7.11b, when a shock interacts with boundary layer, the pressure rise in the shock becomes extreme for the inner layer; some flow is driven upstream and becomes eddy flow of a separation zone. The general flow separates from the surface to accommodate this pressure; the shock takes the shape of an inclined shock, leading to bifurcation of the lower part of the shock. In this situation, a part of the flow passes through the main shock while a part of the flow passes through the bifurcated shock system. This causes a differential in total pressure and the velocity downstream of the shock; this difference is reconciled to through a vortex sheet. The flow from the vortex sheet to edge of boundary layer forms a supersonic tongue. Now, the flow area at the entry of the intake is not sufficient for the flow to go through it. The upstream pressure tries to push it inside whereas the downstream pressure tries to eject the whole shock system out. Hence, the main shock does not touch at the cowl lip. Instead, a bow shock originates from the cowl lip.

The photographs in Fig 7.11b show that boundary layer on the ramp separates upstream of the impingement point of the reflected shock from the cowl. The separated shear layer and reflected shock appear to intersect each other ahead of the throat. A spillage of the flow can be observed from the cowl lip. This spilled flow causes reduction in the mass flow rate through the intake. As the back pressure is increased, the shock travels upstream. At near-critical condition, the terminal shock is thrown out of the intake. From a careful study of the photographs, it appears that at supercritical condition, Dailey instability dominates, whereas at near-critical and subcritical operation, the flow filed is accompanied by Ferry type instability.

Fig 7.11c compares Schlieren photographs of the intake without and with vent gaps of 0.5, 1 and 1.6mm at various area ratios. Without ventilation, occurrence of bow shock can be observed even at supercritical condition. As the vent gap is increased to 1.6mm, the bow-shock at the cowl lip is replaced by the oblique shock emanating from the ramp leading edge. These observations also suggest that ventilation delays the onset of subcritical operation of the intake. Another major advantage observed in the present experiments is the ability to reduce the intake unsteadiness and stabilize the flow. The video movies recorded show high amplitude buzz oscillations of the shock without ventilation; with ventilation, there was a remarkable reduction in the amplitude of oscillations around critical region. Visual observations show that ventilation leads to delayed occurrence of critical condition, or an extended supercritical operation. Since the effects of back-pressure are transmitted upstream only through the subsonic portion of the boundary layer, removal of some amount of the boundary layer causes the intake to be relatively less sensitive to increase in back pressure. Thus, improvement in the mass flow rate is also expected (not measured in the present experiments).

Oil flow patterns

Surface flow visualizations were carried out at M = 3 and 2.5 for the Mach 3 ramp configuration. Figs. 7.12 show the oil flow pattern on the surface of the model with Mach 3 ramp. On the ramp, flow separation, local reattachment and a final separation, leading to a bubble formation are observed (Fig 7.12a and 7.12b) at area ratios of 2.98 and 1.0 respectively. This type of feature is observed at other area ratios also. Downstream of the throat and around the sharp corner of the ramp, final separation of the flow is seen. Flow separation at the corresponding location on the side plates is also observed, as shown in Fig 7.12a and 7.12c. Surface flow patterns inside the cowl show three lines (Fig 7.12d) caused by the intersection of the ramp shock (most upstream location), reflected shock (intermediate location) and the terminal shock (most down stream location) to the cowl. As the exit area is reduced the latter two lines progressively move upstream, while the first line is relatively undisturbed. At the smaller A_e/A_{th}, the shock occurs close to the cowl lip. The flow pattern in Fig 7.12e suggests clear oscillations of the shock between the two positions. Other results obtained at this Mach number showed upstream movement of the shock, as exit area is reduced. Fig 7.12f (i)-(iv) shows the flow pattern on the side plate indicating traces of terminal shock at the side plate of the intake. As area ratio is reduced, upstream movement of the shock is observed.

Results of Buzz Visualization

At the critical condition, the terminal shock reaches the intake throat where it is close to neutrally stable condition. A small increase in back pressure pushes the normal shock into the upstream convergent flow passage. In this position shock is unstable and is pushed out of the air-intake. This sets up a subsonic flow in the intake, accompanied by spillage of the mass flow ingested by the intake and consequent pressure loss. The spilled normal shock ahead of the intake tries to re-enter the intake, but the back pressure condition pushes it forward.

Visualization of buzz was carried out using a high speed camera and the images were recorded at a rate of 2000 frames per second. Shown in Fig 7.13 are some of the instantaneous images corresponding to one cycle of oscillation at M = 3 and A_e/A_{th} = 0.65. Close observations suggest that the buzz oscillations for fully open condition of valve, a mild oscillation of the shock occurs without vent; with vent, these oscillations do not appear. Similar oscillation is observed at A_e/A_{th} > 0.85 without vent. It is evident from the videos that with the vent, the onset of buzz gets postponed and consequent delay in subcritical operation of the intake. The periodicity is found to be about 100 Hz based on correlation between the frame count and the time of exposure.

The video movies were further analyzed to quantify the frequency of the shock oscillations. In a single video of about 1500 frames, a sample of 150 frames was considered for analysis. Each image from the sample has a resolution of 800X600X3 pixels. This gives a matrix of 600X800X3 and corresponds to an RGB image. The RGB image was converted to a gray scale image (resolution = 800 x 600) to simplify the analysis. A program was developed in Matlab to read these images and divide each image in to different segments along horizontal axis. Intensity was measured along each of these segments. It was observed during the analysis that maximum intensity was at the point of shock location. These points have been picked up to obtain the shock location. By choosing a reference length and corresponding number of pixel in that region, the displacement of the shock can be obtained. Thus, the shock locations at different time instants with respect to cowl lip can be established. Fig. 7.14a and 7.14b show the shock locations at various time instants. A repetitive oscillation of the shock can be clearly observed from the figures. In order to quantify the frequency of the oscillation, the time-based data obtained from the image analysis was converted to frequency data by using DFT techniques to obtain the frequency spectrum function. If *X(k)* is the FFT of *x(j)* following formulation is used:

$$X(k) = \sum_{j=1}^{N} x(j)\omega_N^{(j-1)(k-1)} \quad \&$$

$$x(j) = \frac{1}{N}\sum_{k=1}^{N} X(k)\omega_N^{-(j-1)(k-1)}$$

where

$$\omega_N = e^{(-2\pi i)/N}$$

N = root of unity

The amplitude spectrum is shown in Fig 7.14c. The data obtained show dominant frequency of 102.4 Hz. Based on the time-interval of 500 μs between successive images (specified by the camera hardware), the shock speed can be estimated. The

shock speed is plotted against shock location to determine the phase trajectories, as shown in Fig. 7.14d. The averaged trajectory, shown in Fig. 7.14e indicates a limit cycle oscillation of buzz.

Van der Pol equation is well known for modeling of nonlinear oscillations (e.g., Karman vortex shedding). The above analysis can be further extended to empirically evaluate the damping factor, which reproduces the experimentally determined mean phase trajectory.

Results of Numerical Simulation

Limited numerical simulation of the flow through supersonic intake was made using commercially available software FLUENT for Mach number of 3 with and without ventilation. Fig 7.15a shows the Mach number and pressure contours, for exit pressure equal to 10 times the free stream pressure. Oblique shock, flow spillage from the cowl and terminal shock are clearly seen. The interaction of shock and boundary layer is clearly shown from the Mach number contours. Mach number contour also shows the compression waves at the ramp ahead of throat and separation bubble. Velocity vector near the cowl and ramp are shown in Fig 7.15b. The separated boundary layer is noticed at the ramp and cowl. This observation was made from the oil flow visualization also. Fig 7.15c shows the contour of Mach number without and with ventilation (1.6mm gap). Good qualitative agreement is seen with the experiments. In the absence of ventilation, flow spillage is observed from the cowl, whereas with ventilation the shock glances the cowl lip. Fig 7.15d shows the comparison of computed data with experiments. Reasonable agreement is seen on the variation of pressure recovery efficiency with and without vent.

7.2 Pressure Measurements at M = 2.5, Mach 3 Ramp

Tests were carried out at M = 2.5 to study the off design performance of the intake model with Mach 3 ramp. The results are similar, as obtained for Mach number of 3.0. Fig 7.16a show the pressure distribution along ramp centerline as area ratio (A_e/A_{th}) is reduced from 2.5 (supercritical) to 0.85 (subcritical) condition. The pressure coefficient is shown along the ramp surface. The pressure value from the first port from the ramp obtained is slightly lower compared to the value (C_{P2}) at Mach number of 2.5 and turning angle 15° from oblique shock theory, mentioned in Table 7.2. After the shock, from first two ports on the ramp measured pressure is constant, where as pressure increases as the distribution is progressed towards cowl lip, because of boundary layer growth on the ramp. As the throat is approached (X = 0.05m), rise in pressure is observed because of compression waves originated due to shock and boundary layer interaction on the ramp. Similar observations were obtained in case of M = 3 also. Rise in pressure is lower at M = 2.5 as compared to that for M = 3 at the same area ratio. As back pressure is increased, the terminal shock moves forward, as indicated from rise in pressure gradient. Supersonic flow on the ramp is unaltered when back pressure is varied up to A_e/A_{th} = 1.3. A consistent pressure rise is observed in subsonic part of the diffuser. Maximum pressure occurs near the area ratio of 1.3, which could be considered as critical area ratio for this Mach number. The critical conditions for M = 3 with this ramp was observed nearly at A_e/A_{th} = 1-1.2. Fig 7.16b shows the pressure distribution on cowl. Pressure at the first port on the cowl is higher compared to that on ramp at this

location, apparently because of strong bow shock at the cowl lip. Upstream movement of the terminal shock is observed with decrease in area ratio.

Effect of ventilation was studied at M = 2.5 also for the vent gap of 0.5mm, 1mm and 1.6mm. All the vents seem to be effective at this Mach number. The improvement is indicated by pressure distribution on various surfaces and pressure recovery. Fig 7.17a-d shows the effect of ventilation on the static pressure distribution along ramp, cowl, side plate and total pressure distribution in the dump plane. Improvement in overall pressure distribution through the intake is observed from the measured value. But it is noted that the separation downstream of the throat is not suppressed by the vent. Out of the entire vents examined, 1.6mm vent showed maximum improvement in terms of efficiency. The Pressure recovery efficiency is shown in Fig 7.17e. The critical area ratio is around 1~1.5. All the vents showed increment in pressure recovery. The maximum improvement is observed of about 23% with 1.6mm vent, a value much lower compared to that observed at M = 3.

Schlieren visualization at M = 2.5

Fig 7.18 shows schlieren photographs taken at M = 2.5 for various exit area ratios and vent gaps. At this Mach number, the ramp shock does not touch the cowl lip, as shown by the shock pattern. Shock pattern is same for the area ratio up to 1.6. Normal shock is thrown out of the intake and bow shock can be seen from the ramp for A_e/A_{th} = 1.0. The effect of different vent gaps on the shock pattern for the A_e/A_{th} = 2.72, 1.6 and 1 show that spillage from the cowl lip is less for 1 and 1.6mm vent compared to that without vent and 0.5mm vent. For A_e/A_{th} = 1.0, the effects of vent are clearly noticeable. Bow shock is seen without vent whereas with vent, the bow wave is replaced by an oblique shock. With 1 and 1.6mm vent the shock remains oblique even at area ratio of 1.0.

Oil flow at M = 2.5, Mach 3 Ramp

Surface flow pattern on the ramp surface with Mach 3 ramp is shown in Fig 7.19a at M = 2.5 and area ratios of 2.67 and 1.77. It is observed that on the ramp, first separation takes place ahead of the throat. The flow reattaches and the reattached flow again separates ahead of second diffuser. This reattachment is seen at the sharp corner of the ramp at M = 3.0. For A_e/A_{th} = 1.77, the ramp surface shows the origin of a pair of counter rotating vortices springing from downstream of the first diffuser. Fig 7.19b shows the traces of terminal shock on the cowl for A_e/A_{th} = 2.67, 1.77 and 1.45. The flow pattern on the side wall of the model at various area ratio is shown in Fig 7.19c. The upstream traverse of the shock is visible from the flow pattern on the side wall also. A sharp separation from the side wall junction at the second diffuser is also evident from the flow pattern on the side wall. Some of the features observed at this Mach number are similar to that at M = 3.0

7.3 Results of Mach 2 ramp; pressure Measurement at M = 2.0

Experiments were carried with and without ventilation at M = 2 with Mach 2 ramp. Fig. 7.20a shows the pressure distribution on the ramp center line. Pressure near the leading edge of the ramp agrees well with the theoretical value. As seen in earlier

cases, for this configuration also, the pressure on the ramp shows a continuous increase, as against the expected constant pressure, apparently due to 3-dimensional effects. The qualitative features of the flow observed at Mach 3 are generally observed at M = 2 also, and hence not repeated here. Critical condition on the ramp of the intake is seen at A_e/A_{th} = 1.24, below which the terminal shock is spilled out of the intake. Fig 7.20b shows the pressure distribution on the cowl. Criticality of the flow condition is shown at A_e/A_{th} = 1.24, as shown on the ramp. Fig 7.20c and 7.20d show the static and total pressure distribution in the dump plane. The differences between the total pressure and static pressures in the dump plane region are marginal especially for x < 0.2, suggesting large scale separated flow; Oil flow visualizations also support this observation. Similar observation were made in case of M = 2.5 & 3.0 with Mach 3 ramp configuration.

Fig. 7.21a-e show the effect of ventilation on the static pressure distribution along the ramp the cowl and side plate, as total pressure recovery at the dump plane as well as pressure across the ramp at A_e/ A_{th} = 1.24. The pressure distribution on the ramp shows a tendency to reach the expected theoretical value for a short distance, suggesting improved quality of flow with ventilation. The static pressures on the components, as well as total pressure in the dump plane show improvements for any vent, as compared to the unvented flow, clearly demonstrating the usefulness of natural ventilation. The reduced pressure at the cowl lip of the vented configuration also suggests the alleviation of the bow-shock with ventilation. 7.21f shows the efficiency of pressure recovery for various vent gaps. While any vent is effective, a gap of 1.0 mm appears to be the optimum, indicating improvement from about 78% to 96% at near-critical condition. For higher vent gap, the recovery drops, apparently because of the potential flow bleeding out of the intake. It may be recalled that for Mach 3 condition, the optimum vent gap was 1.6mm.

Schlieren Visualization at M = 2.0

The effectiveness of bleed by ventilation is very clearly demonstrated in the schlieren photographs on the intake flow at various area ratios in Fig. 7.22. At all the back-pressure conditions, it is apparent that the bow-shock at the lip is replaced by an attached oblique shock, with the most dramatic change for vent gaps of 1.0 and 1.6mm.

Oil flow Visualization at M = 2.0

Figs. 7.23 show the surface flow visualization at M = 2.0 in the range of $1.77 \leq A_e/A_{th} \leq 1.45$. As evident from the Fig 7.23a, the surface flow along the components is highly three dimensional. The side wall flow pattern shows that nearly a third of dump plane flow is separated (also confirmed by pressure measurements). Flow separations on the ramp and corner vortices are visible in Fig 7.23a-(ii). Presence of a terminal shock inside the cowl as well as side plate is also seen. Terminal shock can thus be traced across the entire width of the cowl and on a part of the side walls. Interestingly, trace of terminal shock on side wall does not extend all the way up to bottom of the ramp. Instead, it ends at less than half the height of the local of the ramp, suggesting a channel shape, with the top and sides bounded while the bottom is on the separation bubble. In such a case, two streams of the

flow inside the intake may be expected. Fig 7.23b and 7.23c shows the flow pattern for the area ratio of 1.59 and 1.45. The flow pattern is similar to that at area ratio of 1.77 but terminal shock moved upstream for these area ratios.

7.4 Pressure measurements at M = 1.8; Mach 2 Ramp

At M = 1.8, experiments were carried out without ventilation with Mach 2 ramp. Since this is off design condition for the intake, capture area is lesser compared to that at M = 2.0. At this condition, more spillage is expected. Fig 7.24a shows the pressure distribution on the ramp middle surface. The variation of pressure distribution along the surface is similar to that obtained at M = 2.0. Pressure near the leading edge of the ramp agrees well with the theoretical value at this M = 1.8 and 8° flow turning angle. Pressure distribution on the ramp shows a continuous increase after the second port because of boundary layer growth. Further, pressure drops because of expansion and than rises suddenly for x > 0.05, downstream to the throat. This suggests the occurrence of the terminal shock aft of the diffuser as compared to that for M = 2. Pressure distribution for the supersonic flow remains constant up to x = 0.05 for $1.62 < A_e/A_{th} < 1.36$. As area ratio is reduced, rise in the pressure in the subsonic part of the diffuser is observed. For $A_e/A_{th} > 1.36$, the pressure distribution suggests that the shock is thrown out of the intake. The effect of hysterisis is shown in Fig 7.24a, with significant differences between forward (F) and reverse (R) movement of the valve. Figs 7.24b to 7.24d show the pressure distribution on the cowl and the side wall. Effect of back pressure variation is observed at all the other surfaces of the configuration also. Fig 7.24e shows the variation of efficiency of pressure recovery with area ratio. In the range of 1.25 to 1.5 maximum pressure recovery is observed.

Schlieren visualization at M = 1.8; Mach 2 Ramp

Schlieren pictures obtained for M = 1.8 with Mach 2 ramp are shown in Fig 7.25. As it is off- design operation of the intake a detach shock is expected at the cowl lip. As the back pressure is increased the shock is moved forward and increase in the flow spillage form the cowl lip can be observed. For $A_e/A_{th} < 0.83$, bow shock in front of the intake can be seen. For curiosity's sake, when the back pressure was further increased, a dangerous condition of standing normal shock in front of the intake was observed.

Oil-flow visualization at M = 1.8; Mach 2 Ramp

Surface flow pattern at off design conditions are presented in Fig 7.26a-c at M = 1.8. It is observed that extent of separated flow inside the intake is lesser at M = 1.8 than that at M = 2.0, especially at $A_e/A_{th} = 1.59$. Traces of corner vertices are observed at this Mach number also.

7.5 Mach 2.5 Results, Mach 2 Ramp

Fig. 7.27 shows typical results obtained for Mach 2 ramp at M = 2.5. At this condition, the oblique shock from the ramp is fully inside the cowl lip. Fig 7.27a shows the pressure distribution along the ramp centre line for various area ratios. From the figure, a mild rise in pressure along the ramp surface is observed. Other

features are similar as obtained for M = 2. Pressure rises upstream of the throat, followed by expansion. Rise in pressure beyond throat indicates occurrence of terminal shock and constant pressure region occurs downstream. For area ratio lesser than 1.1, the pressure distribution starts changing on the ramp, probably due to normal chock getting thrown out of the intake. Maximum pressure occurs at the area ratio of 1.1. Pressure distribution on cowl is shown in Fig 7.27b. It indicates a lower pressure from the first three ports for $A_e/A_{th} > 1.1$ where oblique shock is inside the cowl lip and higher for $A_e/A_{th} < 1$ where shock is thrown out of intake. After terminal shock, the pressure distribution in the subsonic part of the intake increases as back pressure is increased. Fig. 7.27c shows the effect of ventilation on pressure distribution on ramp. It can be observed from the curves that 1mm vent and 1.6mm vent show almost same effectiveness in improvement of pressure recovery in the intake. Improvement in the pressure recovery is observed in this condition also, for all the vent gaps investigated. 1mm vent and 1.6mm vents show similar improvement in pressure recovery of about 15% as shown in Fig. 7.27d.

8.Conclusions

The experiments have established hat the total pressure recovery of the supersonic air-intake can be substantially improved in the range of Mach numbers 1.8 to 3.0 by using the concept of natural ventilation. At all the design and off-design Mach numbers, ventilation substantially improved the efficiency of total pressure recovery. The improvement increased with Mach number, with the optimum vent gap of 1.6mm improving the pressure recovery efficiency from about 61% to 91% at critical condition under Mach 3.0 freestream. Ventilation replaced the bow-shock at the cowl lip seen with the basic intake, with an attached oblique shock, suggesting improved stability of the intake flow. High-speed video recordings of intake buzz oscillations clearly show that the ventilation reduces the severity of buzz at any back pressure ratio; in particular, the onset of buzz is delayed, leading to extended supercritical operation of the intake. Digital processing of images obtained from the high-speed camera suggests that the shock oscillation has a limit cycle oscillation, with a dominant frequency of about 102 Hz. Surface-flow visualizations clearly show the leakage of viscous flow from the vent gaps, onto the sides of the ramp. Thus, the concept of ventilation clearly brings out the physics that disturbances propagate upstream in a supersonic flow within the subsonic portion of boundary layer. Since natural ventilation removes a reasonable portion of the boundary layer, the intake flow becomes more stable to downstream disturbances, such as back pressure. Since the vented intake removes the viscous flow, greater amount of potential flow enters through the intake. This leads to improvement in the total pressure recovery. Since this technique is passive, it is much simpler to adopt in practical applications compared to some of the known methods (boundary layer bleed, suction, blowing, etc). Numerical simulations carried out for selected cases indicate satisfactory qualitative agreement with the experimental data.

ACKNOWLEDGEMENTS

The authors express sincere thanks to Dr. A R Upadhya, Director, NAL and Mr. V Nagarajan, Head, NTAF, NAL for approving the in-house research project, which enabled the present studies. The support extended by and Dr Sajeer Ahmed, EAD by offering the 0.3m wind tunnel and technicians for the present work is acknowledged with thanks. Special thanks to Dr V Mudkavi, Head, CTFD for discussions on numerical simulations. Our sincere thanks to Prof KPJ Reddy, Prof. G Jagadish and their research students at AE Department, Indian Institute of Science, Bangalore for supporting our effort with a high speed camera, without which clear visualization and understanding of buzz phenomenon would not have been possible. The assisstance of the Instrumentation and Controls group of 1.2m and 0.3m wind tunnels. Mr. Periyanagam of 0.3m wind tunnel was extremely helpful in setting up the models and in conducting the tests. The cooperation and help extended by the Model shop staff of NAL is thankfully acknowledged. The efforts of Mrs. Anju Sharma, Scientist NTAF was mainly instrumental in developing the necessary software tools for stepper motor control and hand-shake operation with the wind tunnel data acquisition system is acknowledged. General assistance provided by colleagues Mr. Nitin Khamesra, Mr. Rajan Kurade and Mr. Tushar Panpate is acknowledged with thanks.

REFERENCES

1. "Air-Intake for High-Speed Vehicles", AGARD-AR-270, 1991

2. Seddon, J & Goldsmith, E.L., "Intake Aerodynamics", AIAA Education Series, 1985

3. Jeil, C.S.,"Course on Missile Aerodynamics", AGARD R754

4. Fukuda, M.K. Hingst and W.G. and Reshotko E, "Control of Shock Waves-Boundary layer Interactions by Bleed in Supersonic Mixed Compression Inlets", NASA CR-2595

5. Suryanarayana, G. K., Henning Pauer & Meier, G. E. A., "Bluff body drag reduction by passive ventilation ", Experiments in Fluids 16 (1993), 73-81

6. Suryanarayana, G. K. & Meier, G. E. A., "Effect of ventilation on the flow-field around a sphere", Experiments in Fluids 19 (1995), 78-88

7. Suryanarayana, G. K. & Prabhu, A., "Effect of natural ventilation on the boundary layer separation and near-wake vortex shedding characteristics of a sphere", Experiments in Fluids 29 (2000), 582-591

8. "Aerodynamic Drag Reduction of Bluff Bodies – Application of Natural Ventilation", G K Suryanarayana, Lambert Academic Publishers, Cologne, Germany, ISBN 978-3-8383-1103-6, Dec 2009

9. Manual for 1ft X 1ft trisonic wind tunnel, EAD, NAL

Table

Table 5.1: Deviation of set valve angle from achieved valve angle

Set angle (deg.)	Achieved Angle (deg.)	Difference (deg.)
10	10.021	0.021
32	32.119	0.119
34	34.093	0.093
36	36.029	0.029
38	38.029	0.029
40	40.022	0.022
42	42.021	0.021
44	44.115	0.115
46	46.009	0.009
48	48.007	0.007
50	50.113	0.113

Table 5.2 MAPPING FOR SCANNER AND MODEL PORTS (Mach2 Ramp)

SCANNER-1		SCANNER-2		SCANNER-3		SCANNER-4		SCANNER-5	
Scanner Port	**Cowl Port**	**Scanner Port**	**Ramp Port**	**Scanner Port**	**Ramp Port**	**Scanner Port**	**Sideplate Port**	**Scanner Port**	**Total pressure Port**
1	C1	1	RM1	1	RS1	1	SP1	1	PR1
2	C 2	2	RM 2	2	RS 2	2	SP2	2	PR 2
3	C 3	3	RM 3	3	RS 3	3	SP3	3	PR 3
4	C 4	4	RM 4	4	RS 4	4	SP4	4	PR 4
5	C 5	5	RM 5	5	RS 5	5	SP5	5	DP 1
6	C 6	6	RM 6	6	RS 6	6	SP6	6	DP 2
7	C 7	7	RM 7	7	RS 7	7	SP7	7	DP 3
8	C 8	8	RM 8	8	RS 8	8	SP 8	8	DP 4
9	C 9	9	RM 9	9	RS 9	9	SP 9	9	DP 5
10	C 10	10	RM 10	10	RS 10	10	SP 10	10	DP 6
11	C 11	11	RM 11	11	RM 16	11	SP 11	11	DP 7
12	C 12	12	RM 12	12	RM 17	12	SP 12	12	DP 8
13	C 13	13	RM 13	13	RM 18	13	SP 13	13	DP 9
14	C 14	14	--	14	RM 19	14	SP 14	14	--
15	C 15	15	--	15	--	15	SP 15	15	--
16	REF1	16	REF2	16	REF3	16	REF4	16	REF5

Table 5.3 MAPPING FOR SCANNER AND MODEL PORTS (Mach3 Ramp)

SCANNER-1		SCANNER-2		SCANNER-3		SCANNER-4		SCANNER-5	
Scanner Port	**Cowl Port**	**Scanner Port**	**Ramp Port**	**Scanner Port**	**Ramp Port**	**Scanner Port**	**Sideplate Port**	**Scanner Port**	**Total pressure Port**
1	C1	1	RM1	1	RS1	1	SP1	1	PR1
2	C 2	2	RM 2	2	RS 2	2	SP2	2	PR 2
3	C 3	3	RM 3	3	RS 4	3	SP3	3	PR 3
4	C 4	4	RM 4	4	RS 5	4	SP4	4	PR 4
5	C 5	5	RM 5	5	RS 6	5	SP5	5	DP 1
6	C 6	6	RM 6	6	RS 7	6	SP6	6	DP 2
7	C 7	7	RM 7	7	RS 8	7	SP7	7	DP 3
8	C 8	8	RM 8	8	RS 9	8	SP 8	8	DP 4
9	C 9	9	RM 9	9	RS 10	9	SP 9	9	DP 5
10	C 10	10	RM 10	10	RM 16	10	SP 10	10	DP 6
11	C 11	11	RM 11	11	RM 17	11	SP 11	11	DP 7
12	C 12	12	RM 12	12	RM 18	12	SP 12	12	DP 8
13	C 13	13	RM 13	13	RM 19	13	SP 13	13	DP 9
14	C 14	14	RM 14	14	--	14	SP 14	14	--
15	C 15	15	RM 15	15	--	15	SP 15	15	--
16	REF1	16	REF2	16	REF3	16	REF4	16	REF5

Table 6.1 Free stream conditions

M_∞	P_o (psi)	P_∞ (psi)
3	60	1.633

Table 6.2 Conditions of numerical simulation

Mach No M_∞	Exit Pressure Pe (in Pa)	Vent Gap (mm)
3.0	$10P_\infty$	0, 1.6
3.0	$12P_\infty$	0, 1.6

Table 7.1 Summary of run conditions

Mach No	Configuration	θ Start	θ End	$\Delta\theta$ Steps	Vent Gap (mm)
1.8	M2 Ramp	0°	50°	5°, 10°	0, 1.6
2.0	M2 Ramp	0°	50°	5°, 10°	0,0.5, 1.0 1.6
2.5	M2 Ramp	0°	50°	2°, 4°, 5°, 10°	0,0.5, 1.0 1.6
2.5	M3 Ramp	0°	50°	2°, 4°, 5°, 10°	0,0.5, 1.0 1.6
3.0	M3 Ramp	0°	50°	2°, 4°, 5°, 10°	0,0.5, 1.0 1.6

Table 7.2 Flow properties obtained from oblique shock theory

M_1	P_{01}	P_{S1}	Q	δ	β	P_{S2}	M_2	C_{P2}
3	60	1.6334	10.2906	15°	32.24	4.6095	2.2549	0.2892
2.5	45	2.6337	11.5226	15°	36.95	6.4988	1.8735	0.3354
2.5	45	2.6337	11.5226	8°	30.01	4.36359	2.1685	0.1501
2	35	4.4732	12.5248	8°	37.21	6.8882	1.7137	0.1928
1.8	30	5.2212	11.8417	8°	41.67	7.8545	1.5225	0.2224

Table 7.3 Theoretical pressure recovery for three shock intakes

M	No. of Shocks	PR
3	3	0.75
2.5	3	0.89
2	3	0.9
1.8	3	0.99

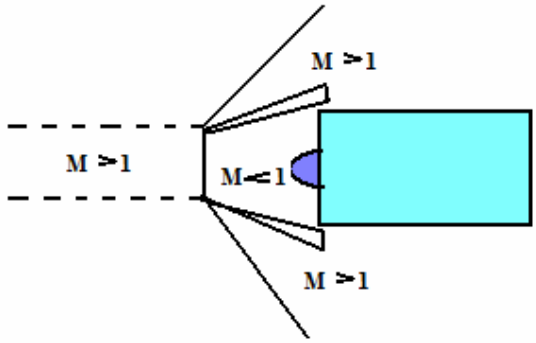

Fig. 1.1: Schematic of a pitot supersonic Intake

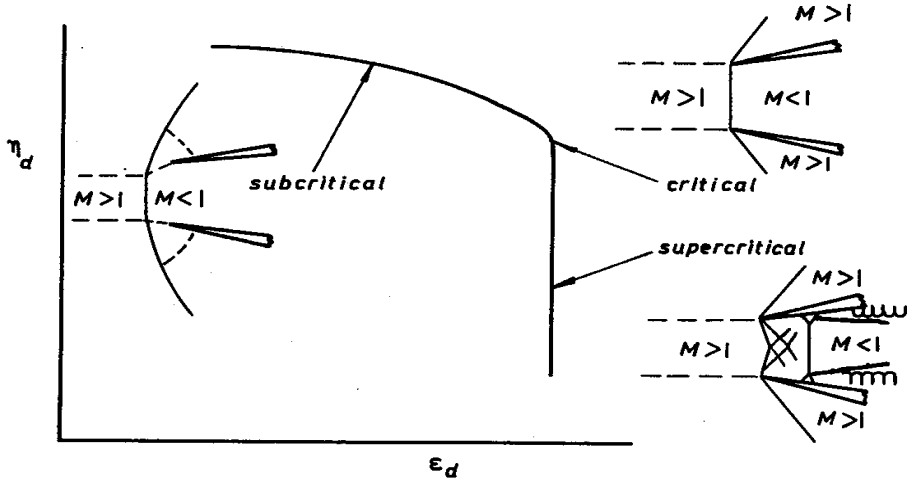

Fig. 1.2: Modes of Operation of a supersonic Intake

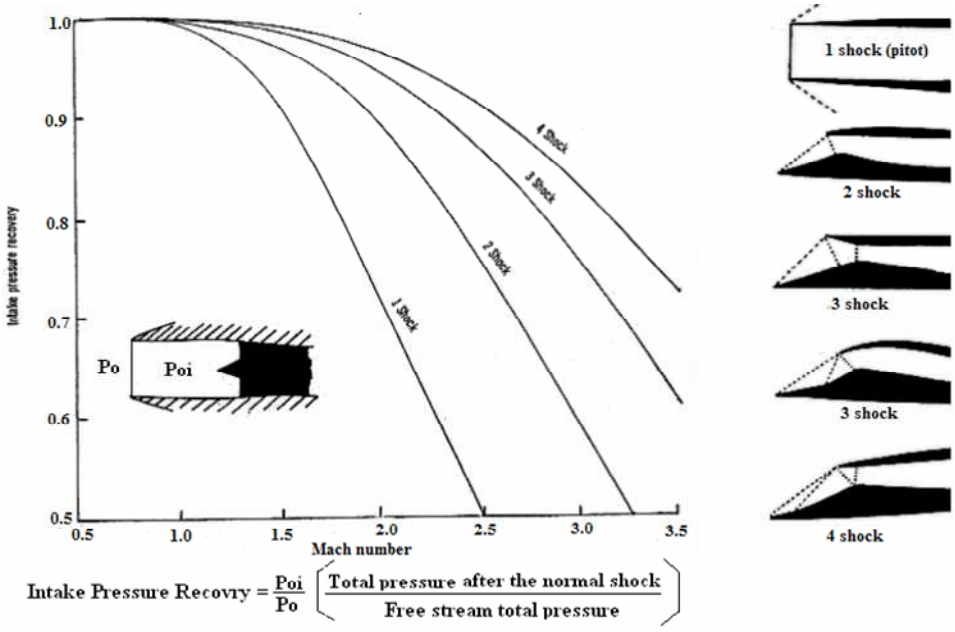

Fig. 1.3: Pressure recovery variation with Mach number for supersonic intakes

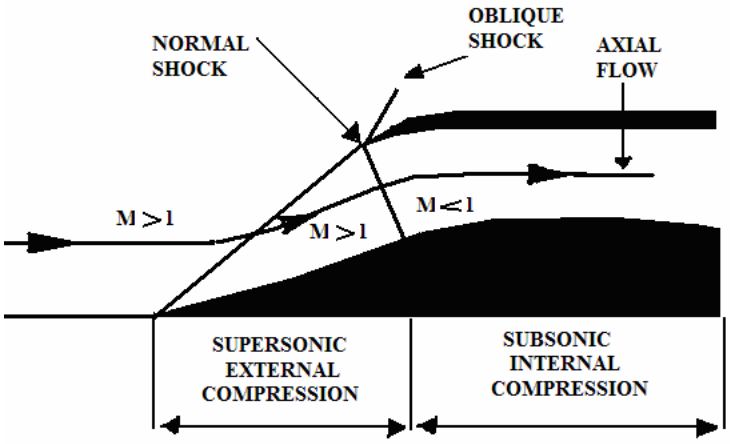

Fig. 1.4: Oblique shock compression Intake operation

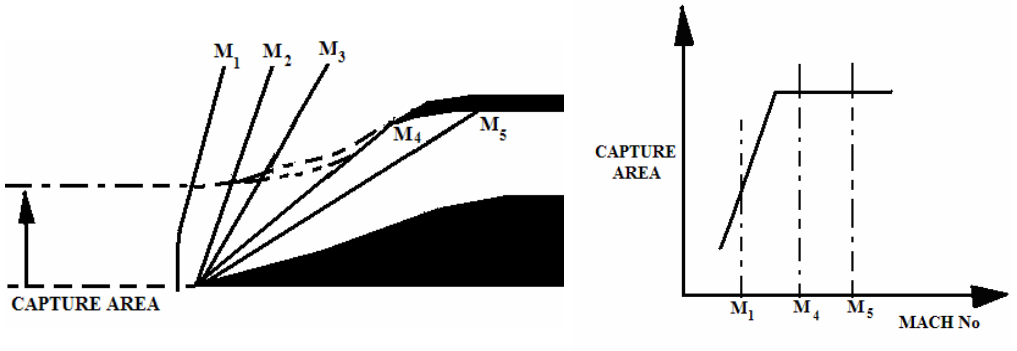

Fig. 1.5: Effect of flight Mach number on oblique shock intake and Capture area variations

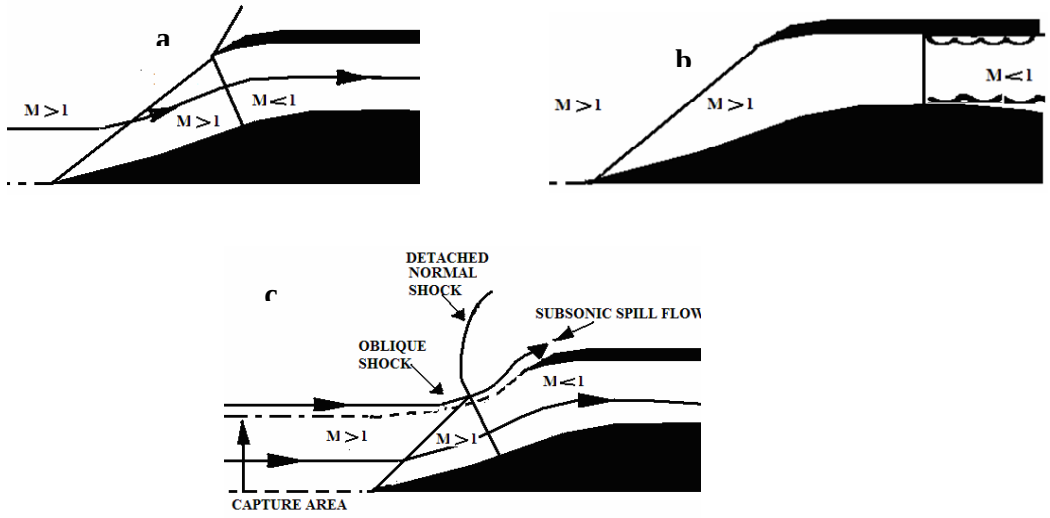

Fig. 1.6: a) Critical, b) supercritical and c) subcritical operation of the intake

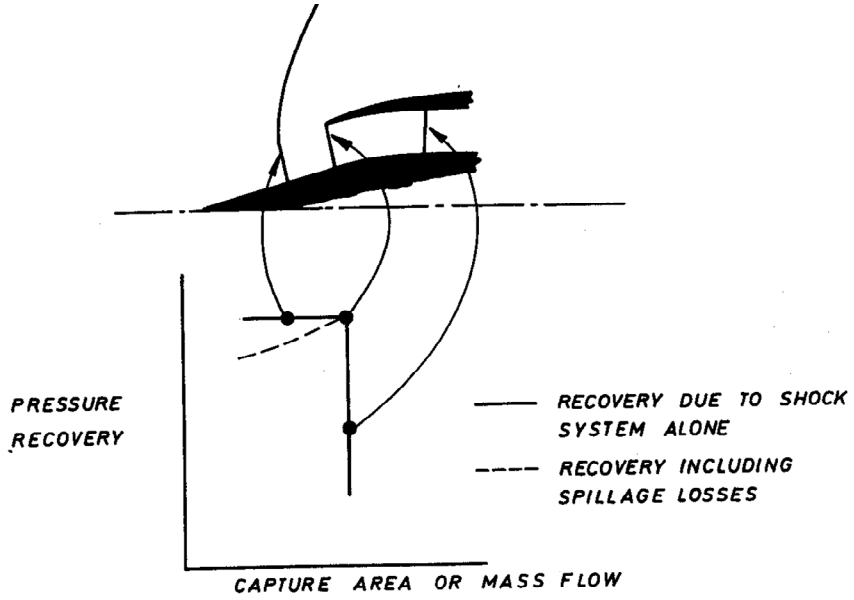

Fig. 1.7: Pressure recovery of the intake for different mode of operation

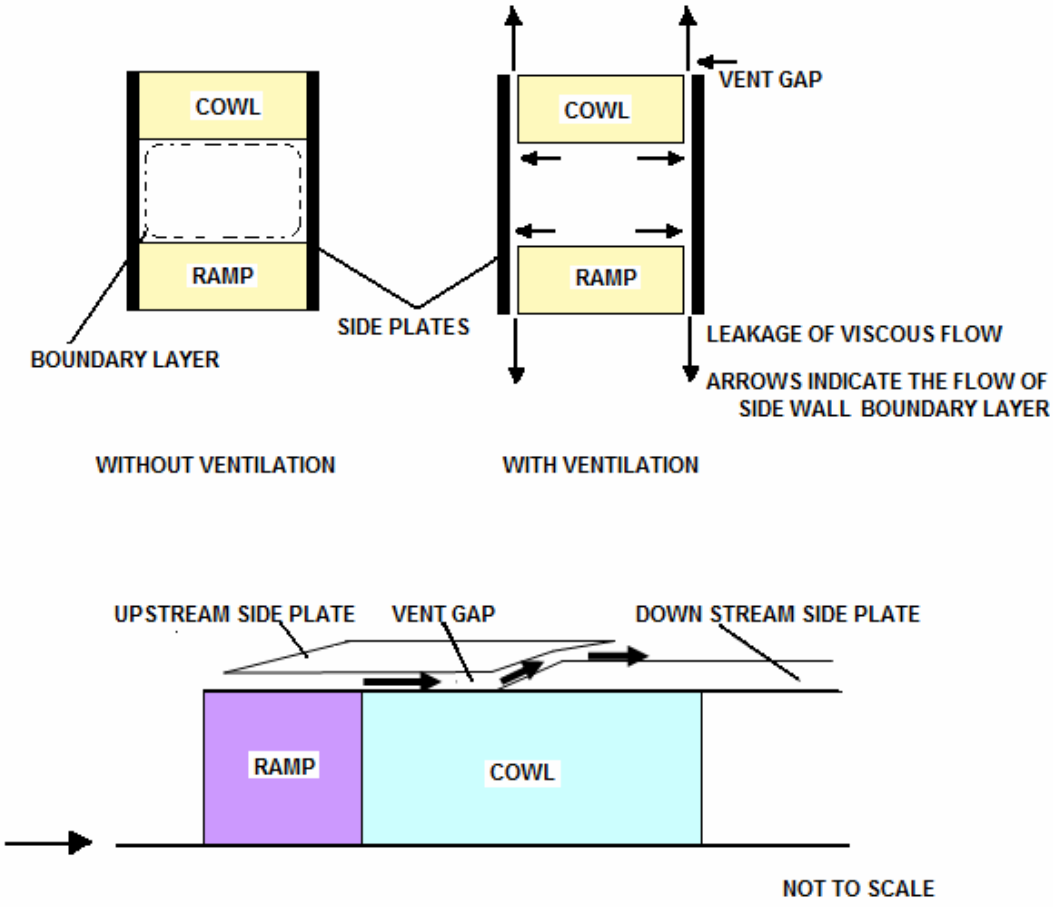

Fig. 1.8: Scheme of natural ventilation

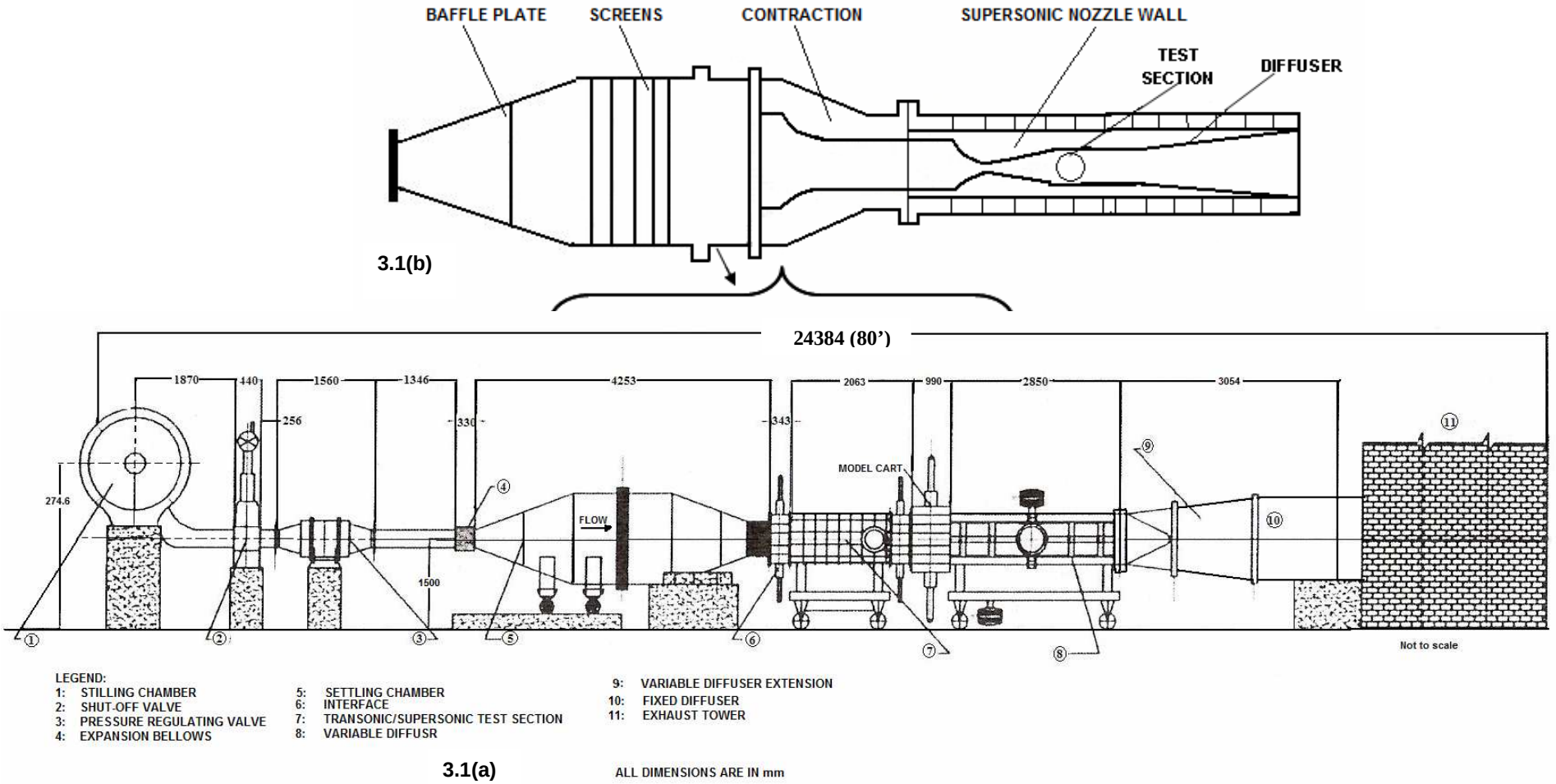

Model Roll = 0°

Fig. 3.1: (a) Schematic of 0.3m trisonic wind tunnel; (b) Expanded view of nozzle and test section

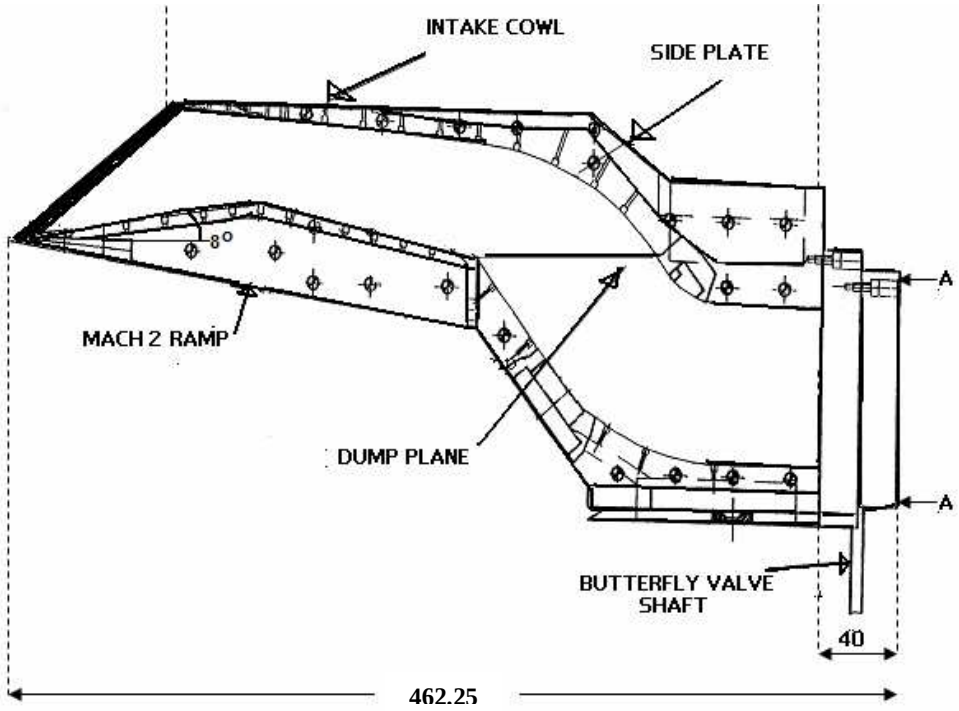

Fig. 4.1: Schematic of the model with Mach 2

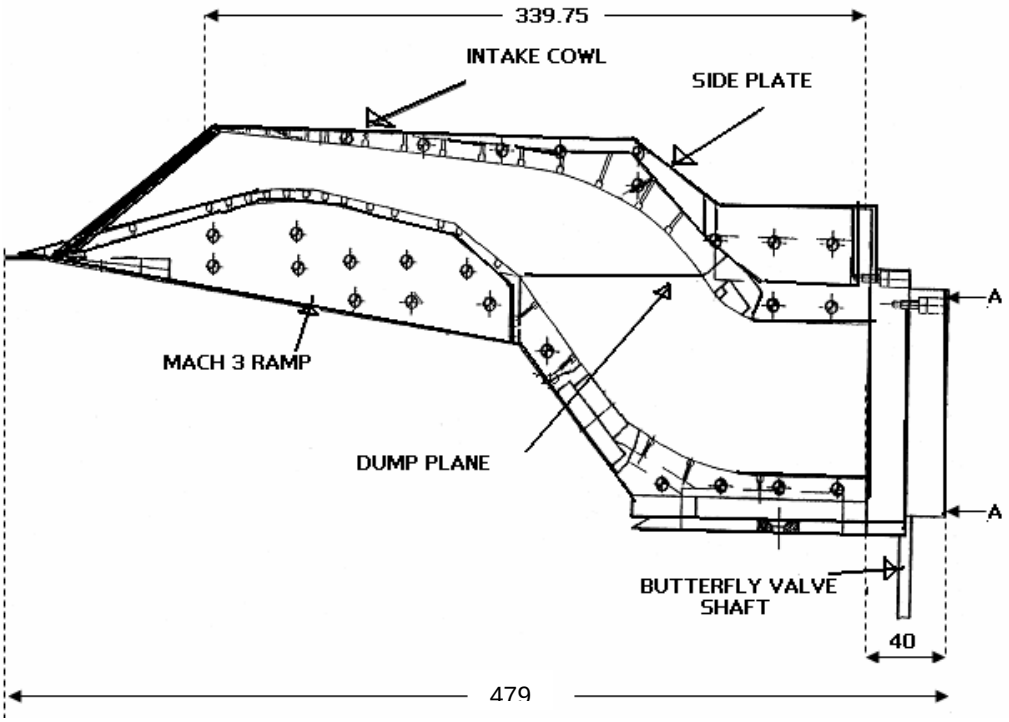

Fig. 4.2: Schematic of the model with Mach 3 Ramp

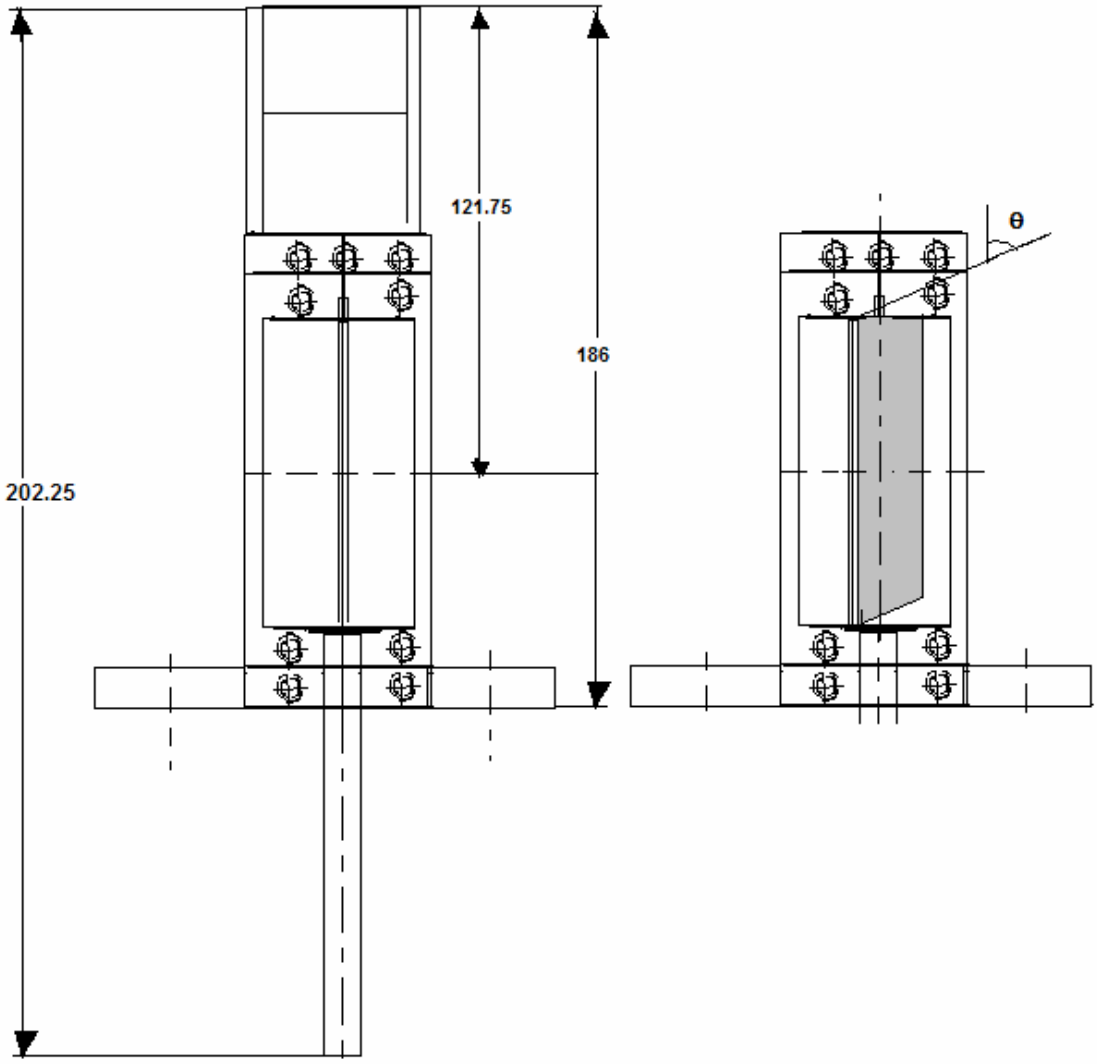

Fig. 4.3: Schematic of the exit at fully open condition and partially open condition

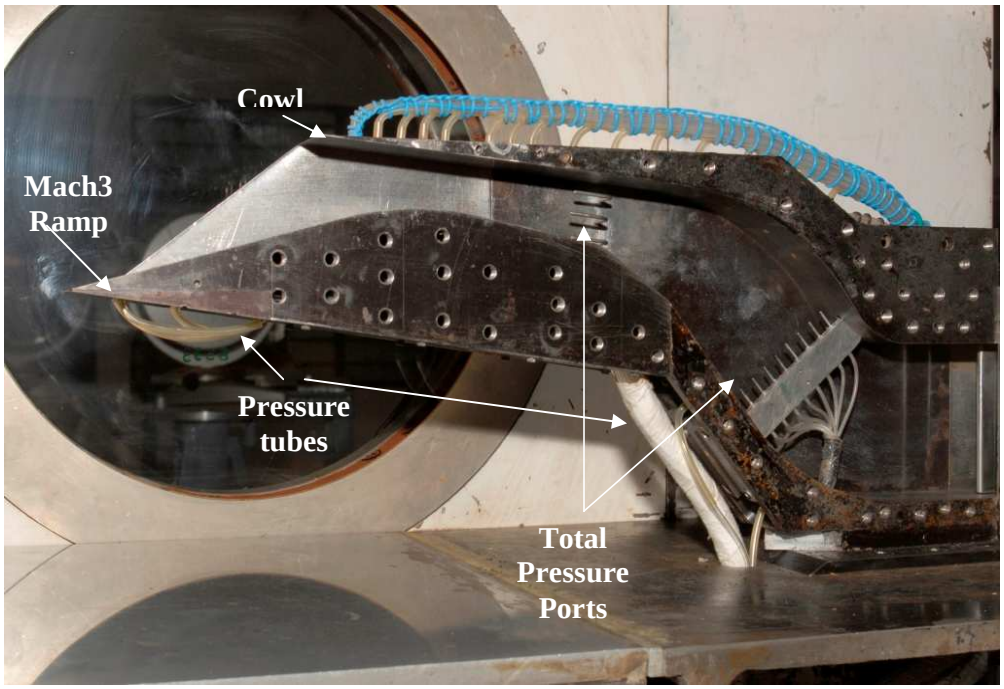

Fig. 4.4: Photograph of the model mounted in 0.3m tunnel of NAL

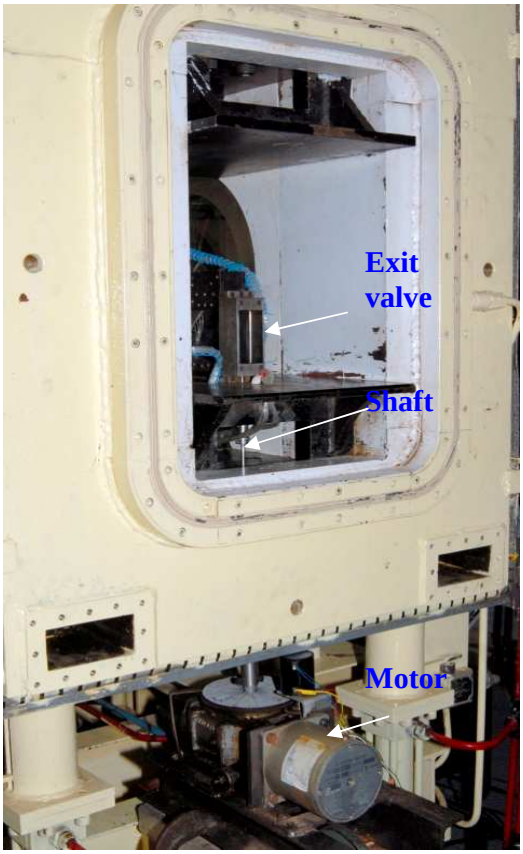

Fig. 4.5: Photograph of exit area control unit

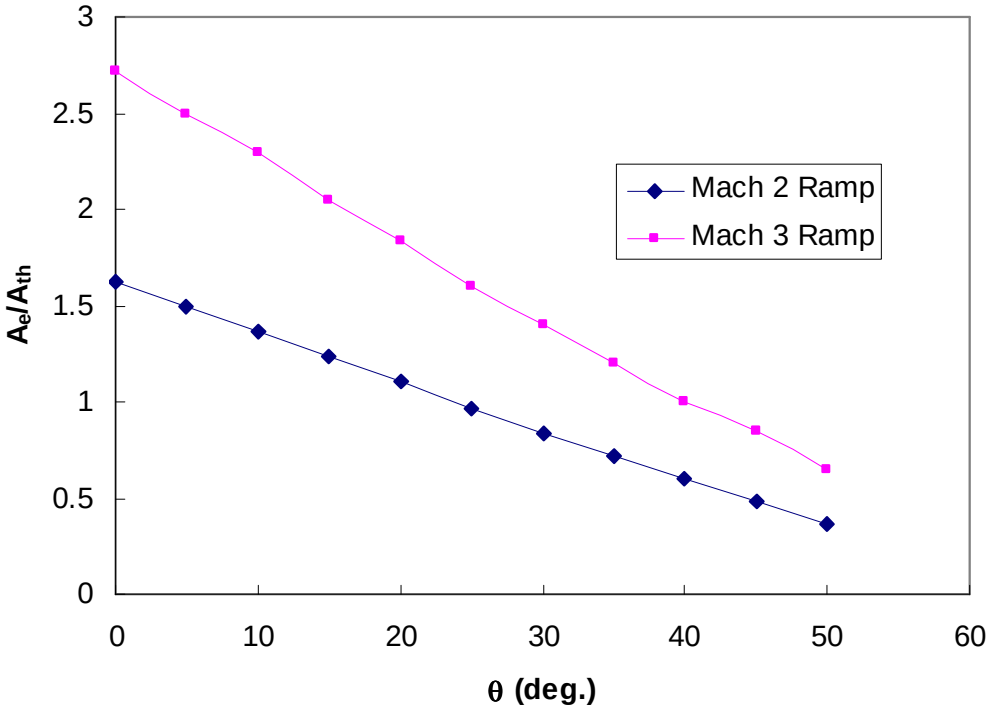

Fig. 4.6: Variation of exit area ratio with valve angle

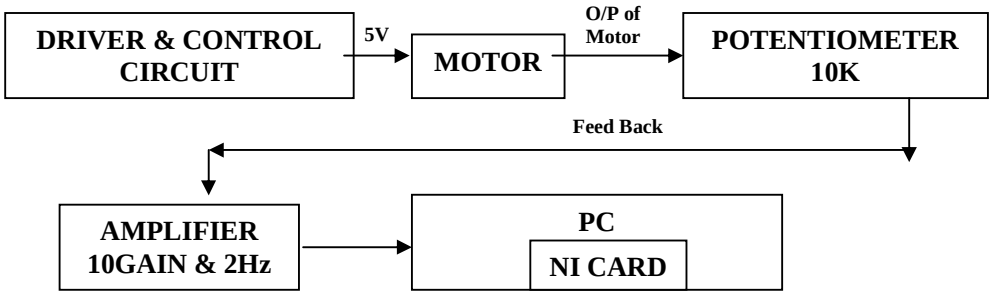

Fig. 5.1: Block diagram for exit area control set-up

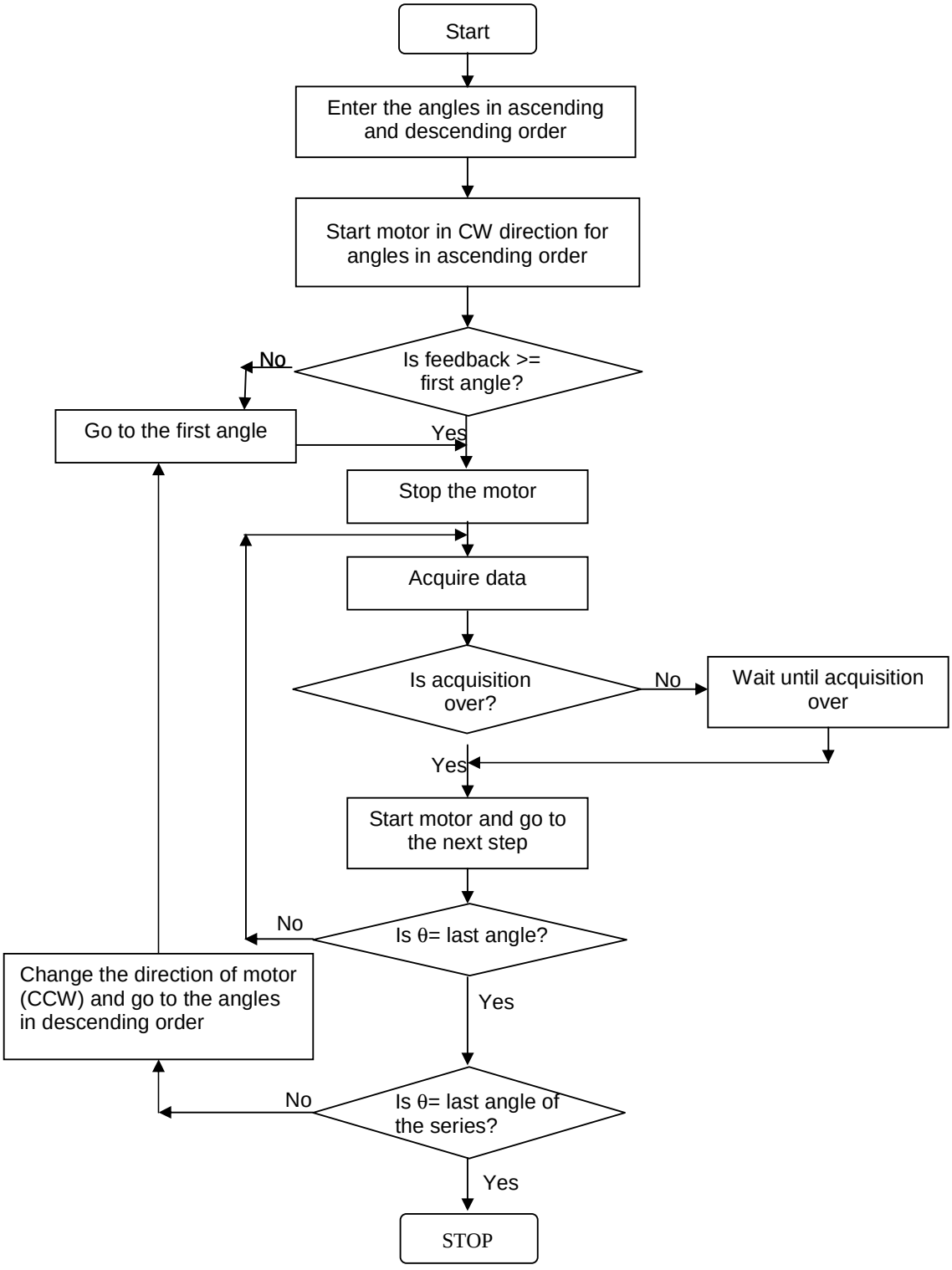

Fig. 5.2: Flow chart of the control program

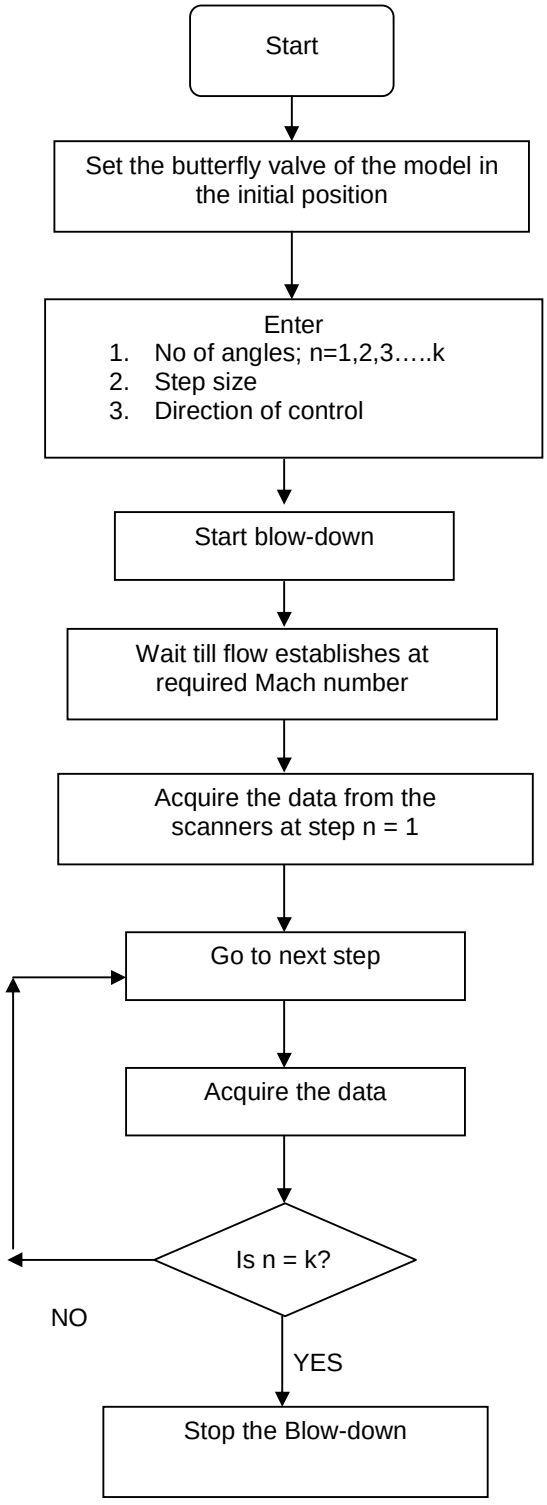

Fig. 5.3: Flow chart for complete valve operation

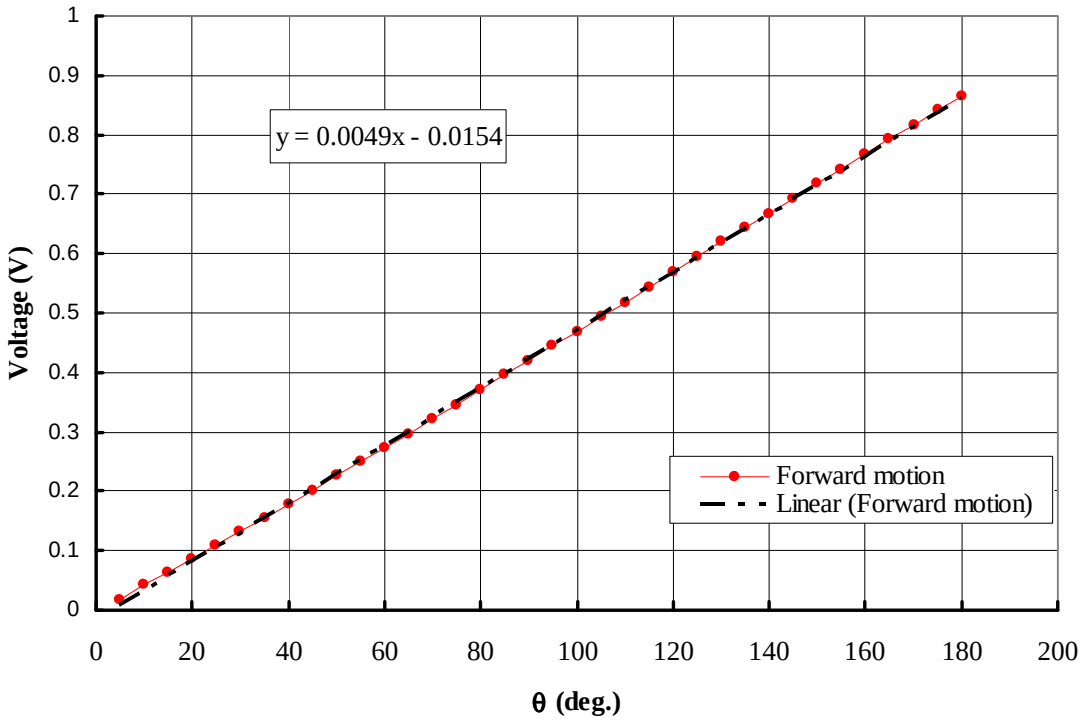

Fig. 5.4: Variation of voltage with valve angle

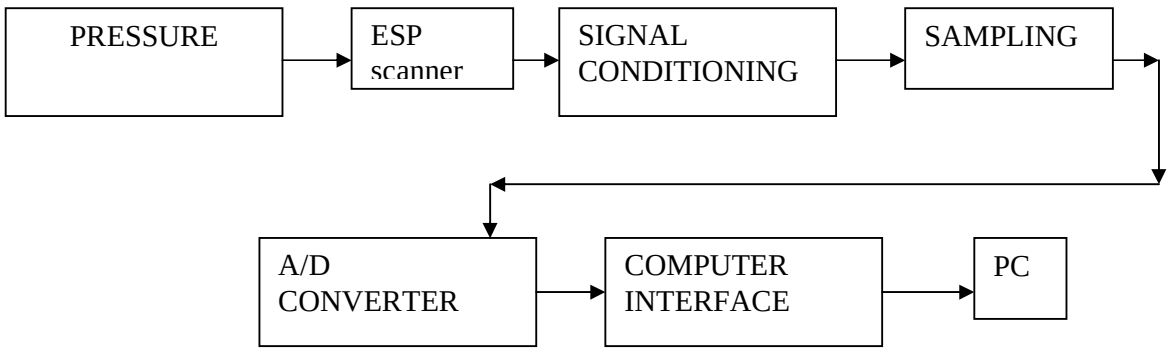

Fig. 5.5: Block diagram for pressure acquisition

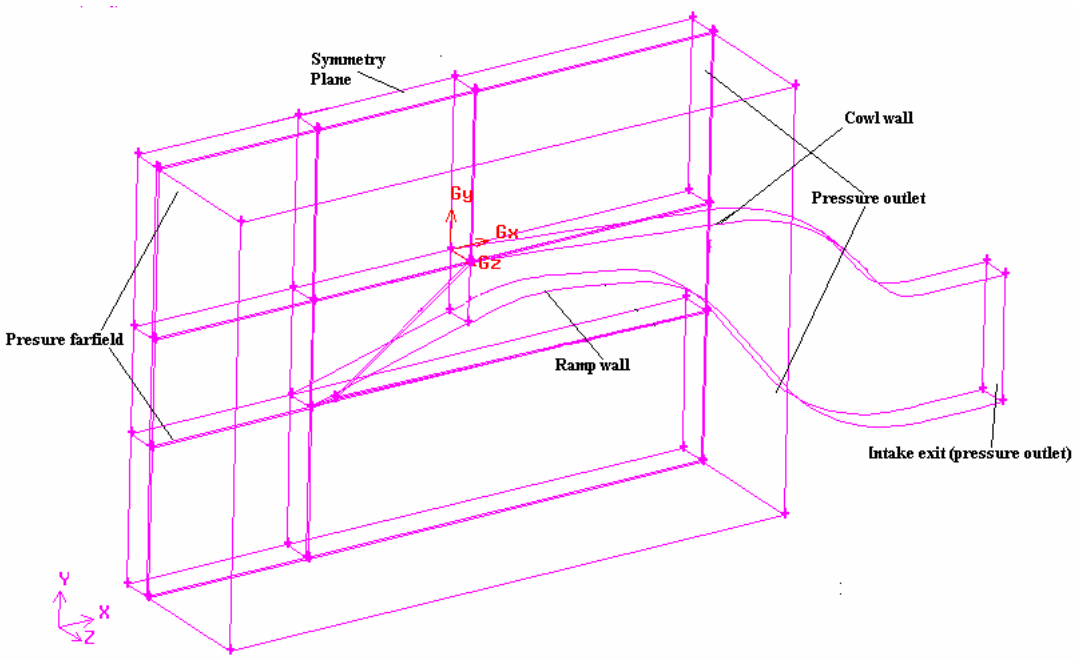

Fig. 6.1: Half of the computational domain for 3D simulation

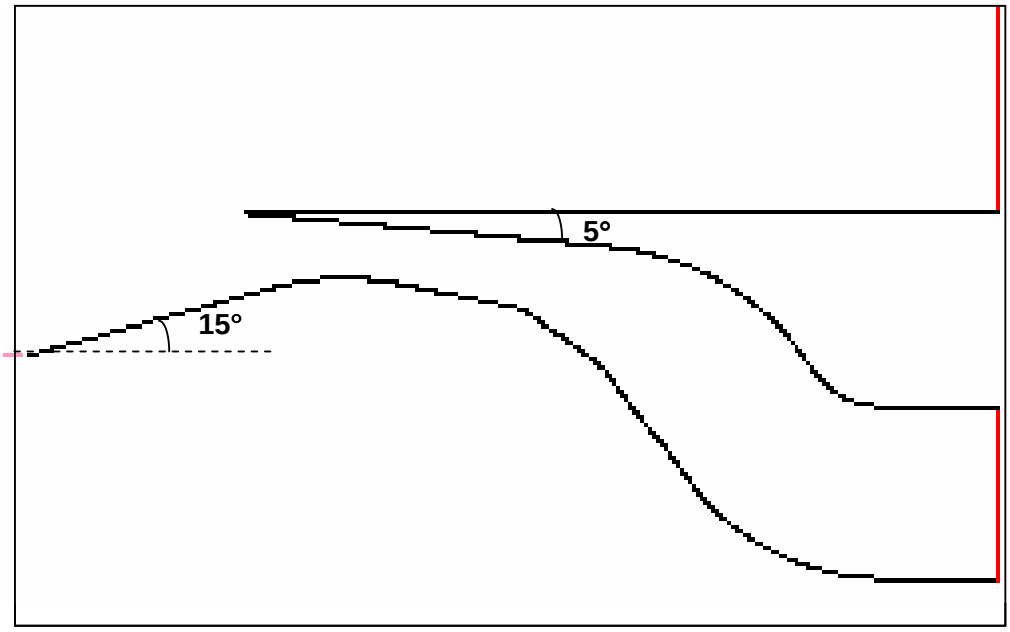

Fig. 6.2: Geometric details of Mach 3 ramp intake model

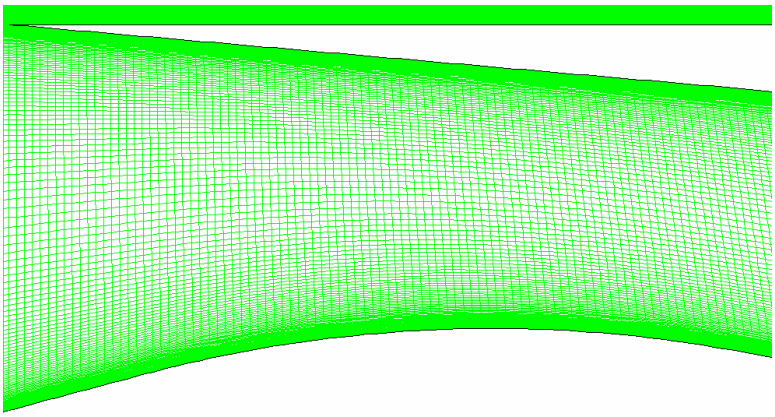

Fig.6.3: Grid within the intake model

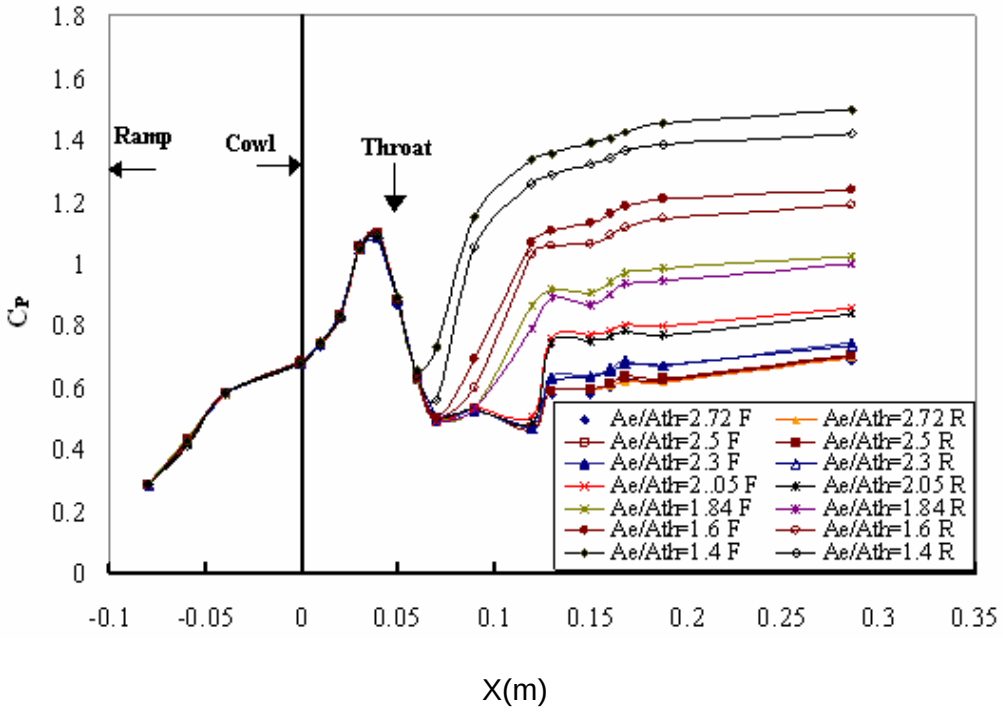

Fig. 7.1a Pressure distribution on Ramp centerline, M =3.0

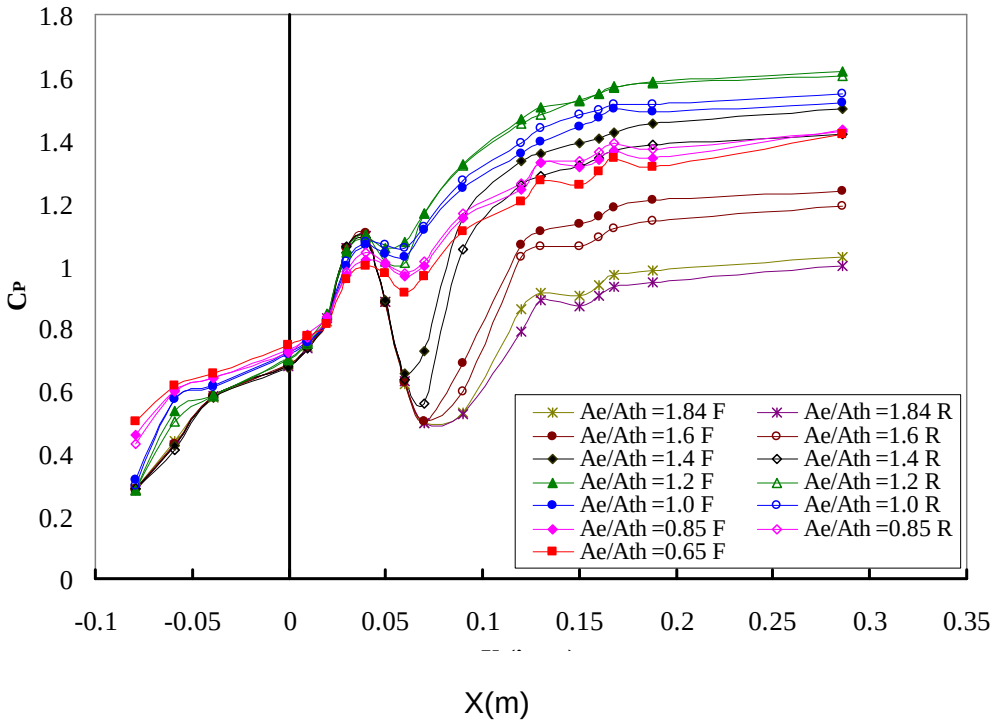

Fig. 7.1a Pressure distribution on Ramp centerline, M =3.0

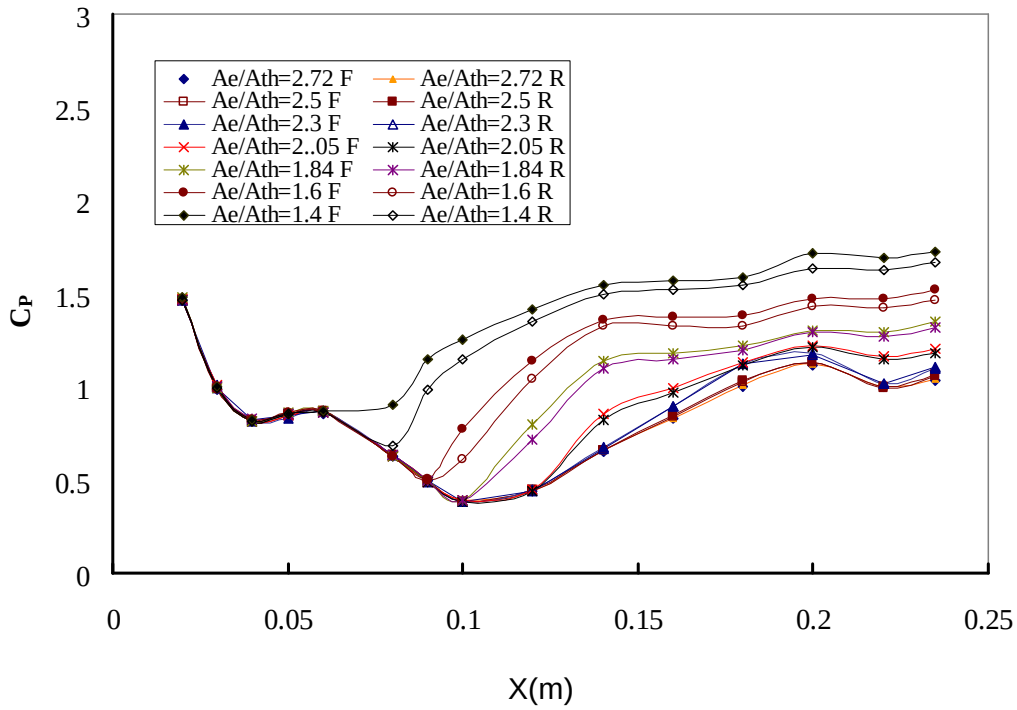

Fig. 7.2a Pressure distribution on Cowl centerline, M =3.0

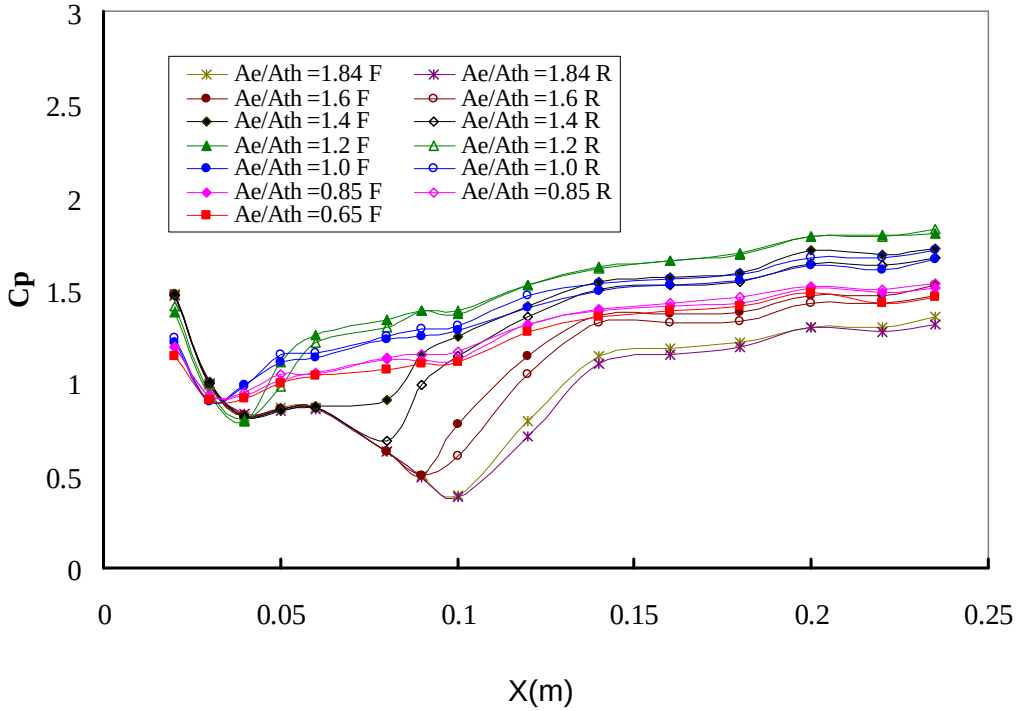

Fig. 7.2a Pressure distribution on Cowl centerline, M =3.0

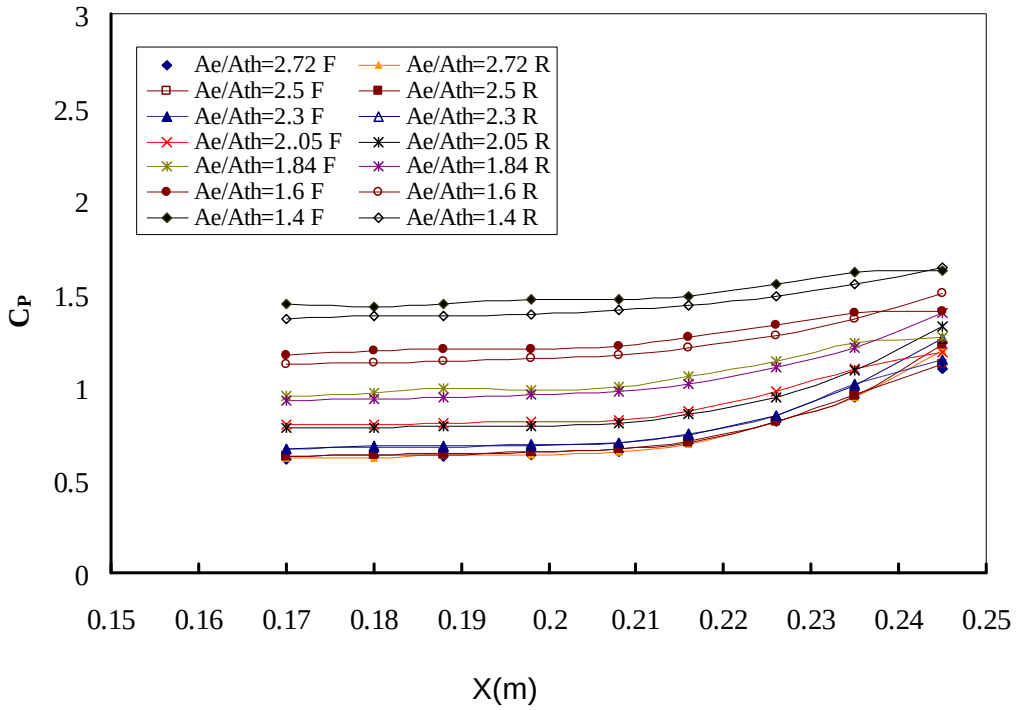

Fig. 7.3a Pressure distribution on Side-Plate, M =3.0

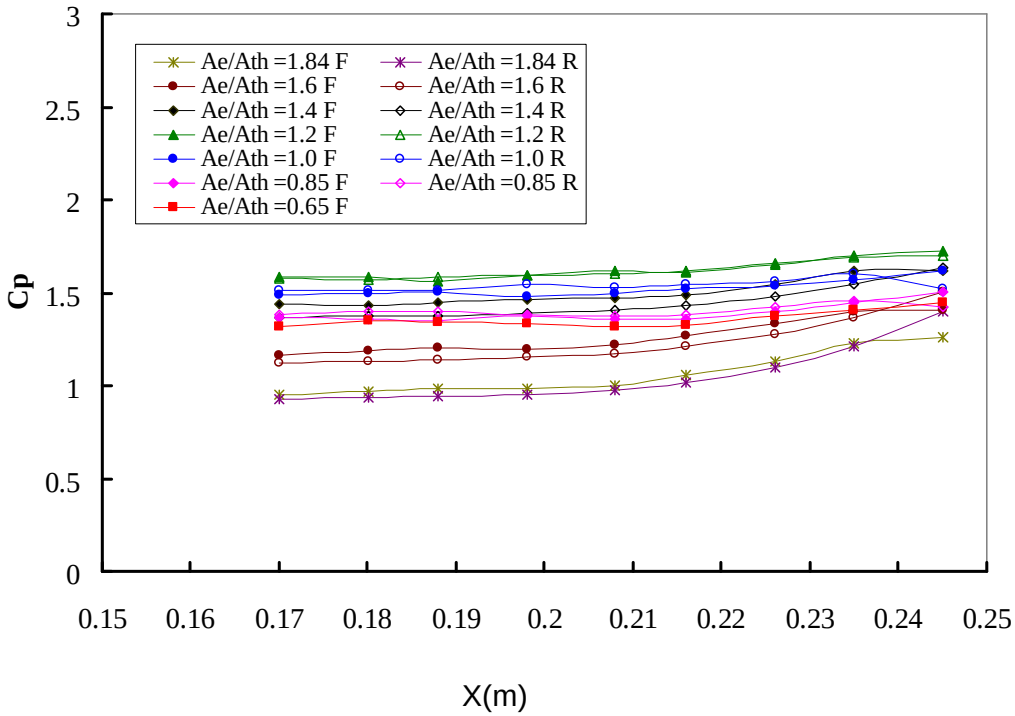

Fig. 7.3b Pressure distribution on Side-Plate, M =3.0

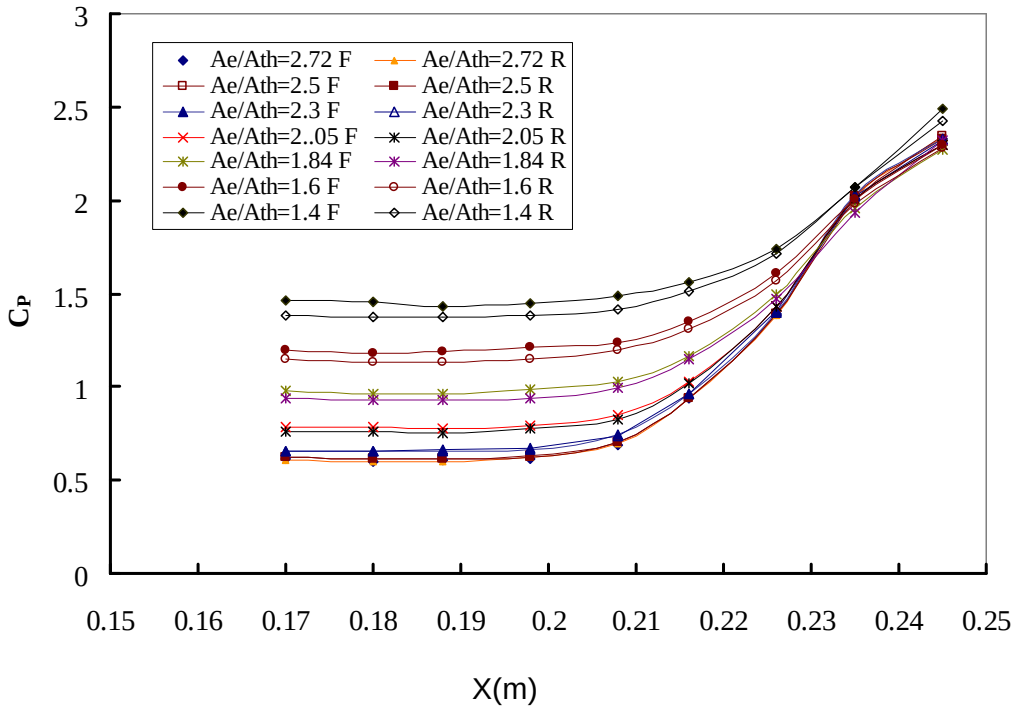

Fig. 7.4a Total pressure distribution in dump-Plane, M =3.0

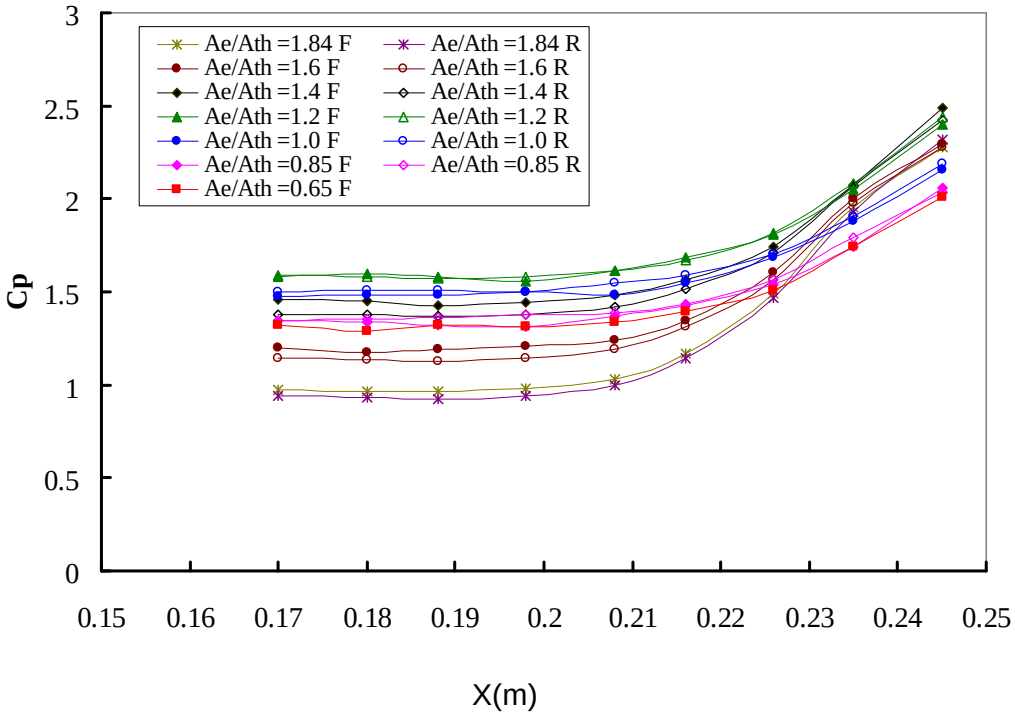

Fig. 7.4b Total pressure distribution in dump-Plane, M =3.0

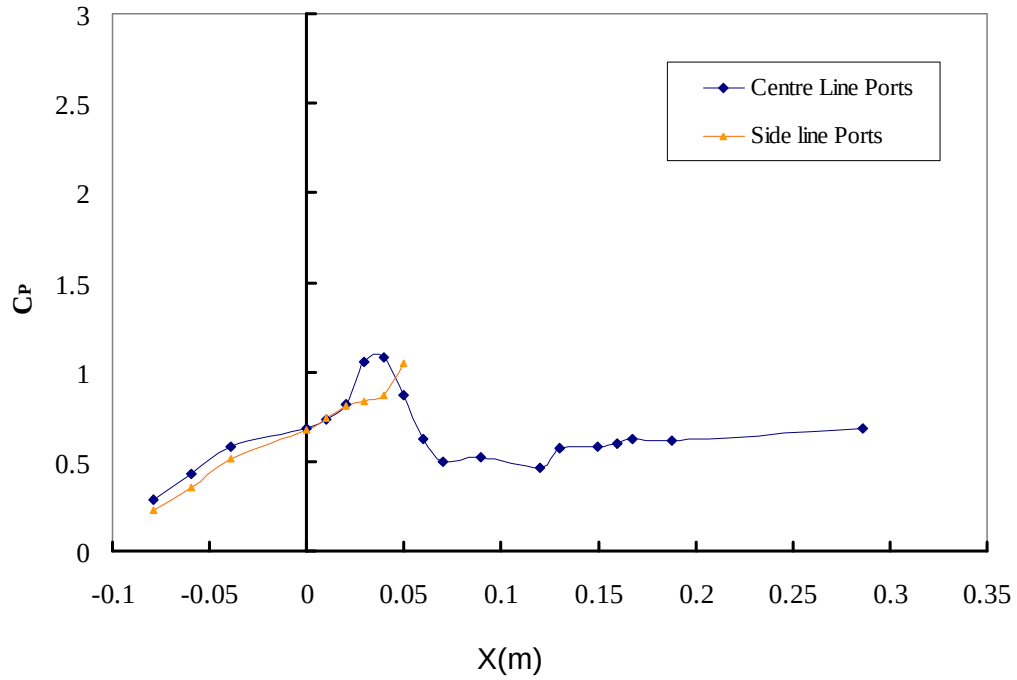

Fig. 7.5a Comparison of pressure distribution on Ramk, M = 3.0, A_e/A_{th} = 2.72

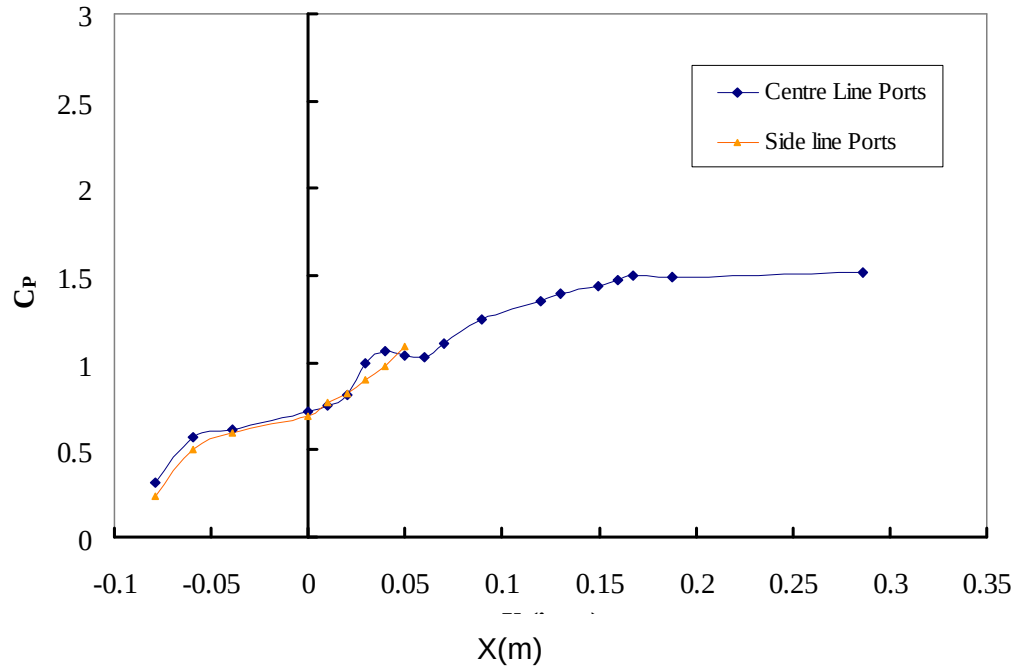

Fig. 7.5b Comparison of pressure distribution on Ramk, M = 3.0, A_e/A_{th} = 1.0

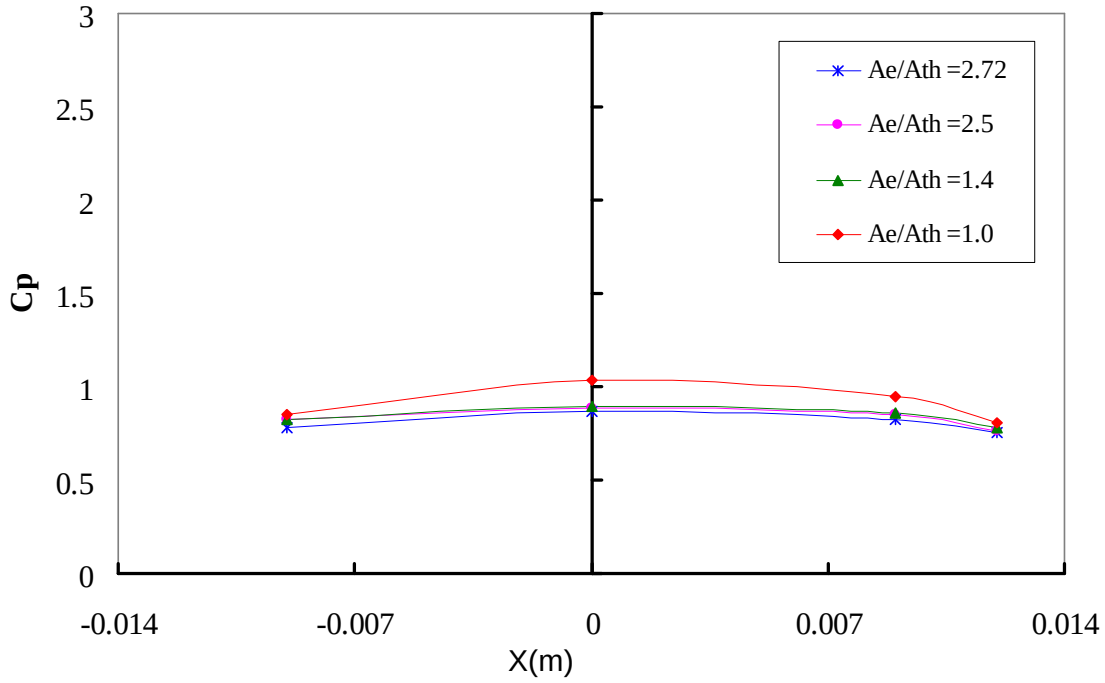

Fig. 7.6 Pressure distribution across Ramp surface at X = 0.039m for various A_e/A_{th}, M = 3.0

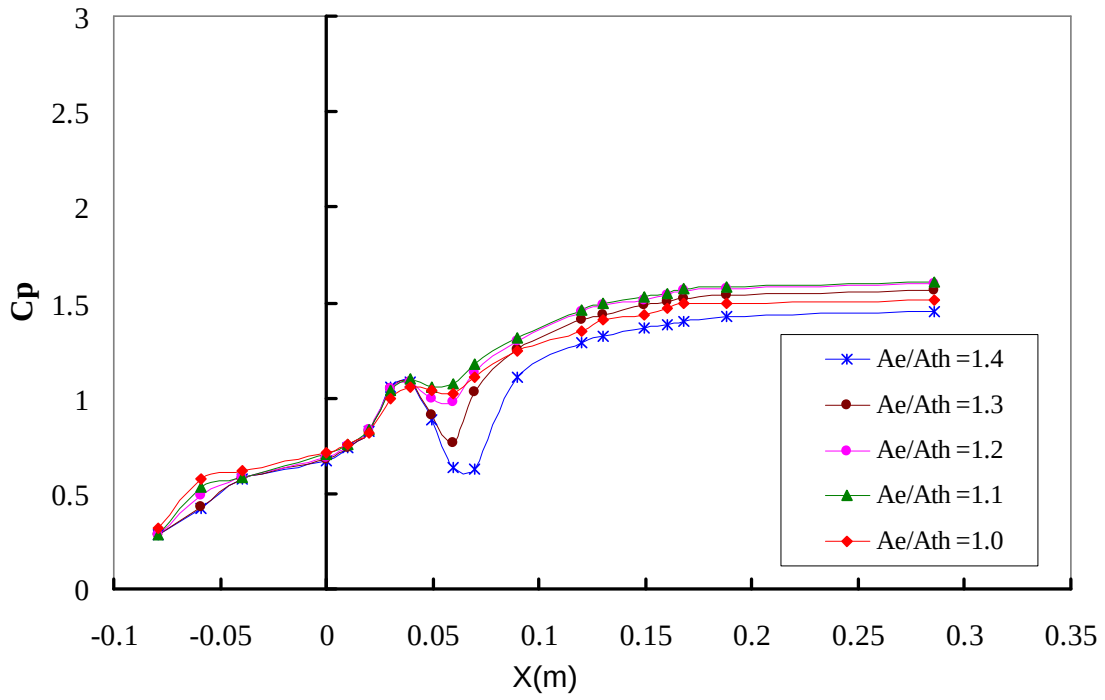

Fig. 7.7a Pressure distribution on Ramp centre line in closer steps of area, M = 3.0

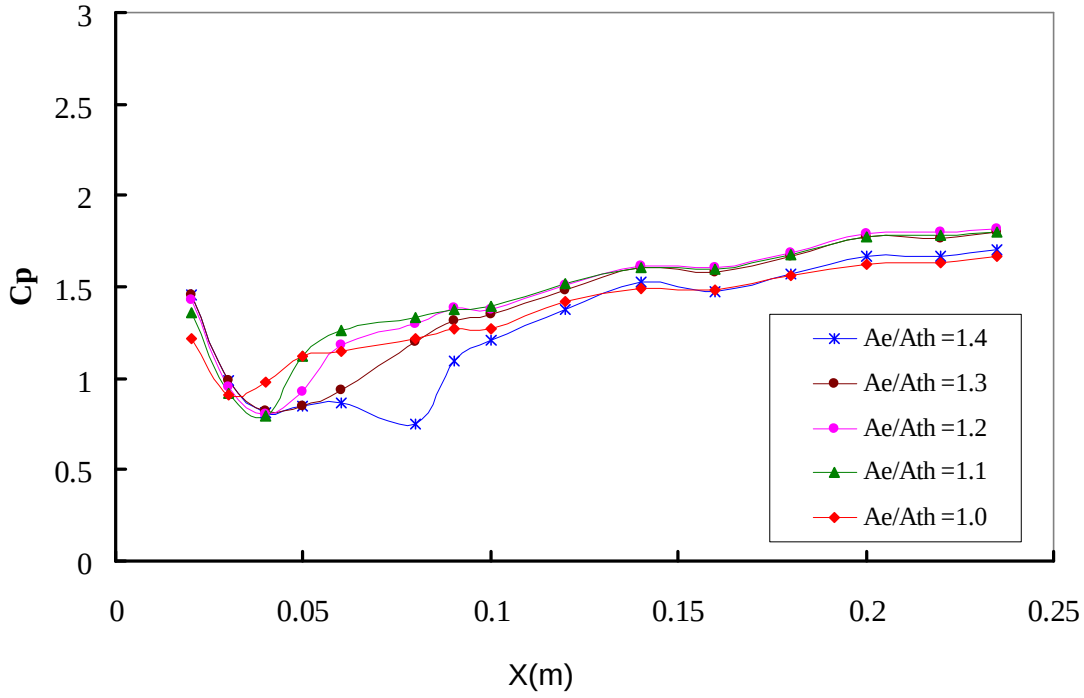

Fig. 7.7b Pressure distribution on Cowl centre line in closer steps of area, M = 3.0

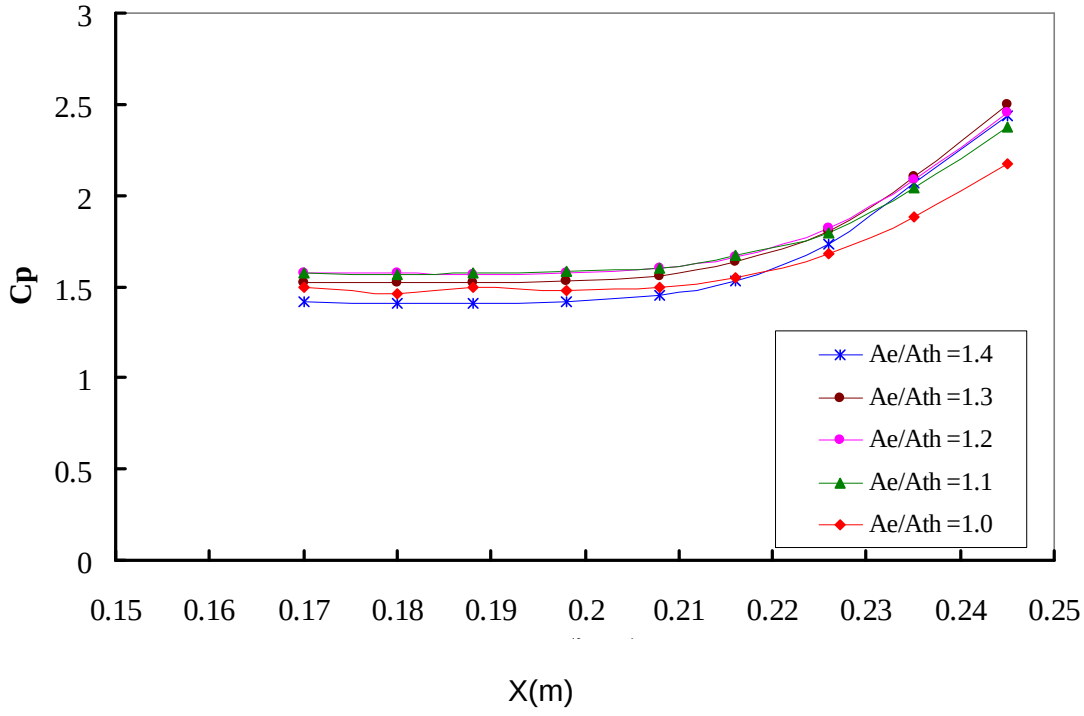

Fig. 7.7c Pressure distribution in dump-plane in closer steps of area, M = 3.0

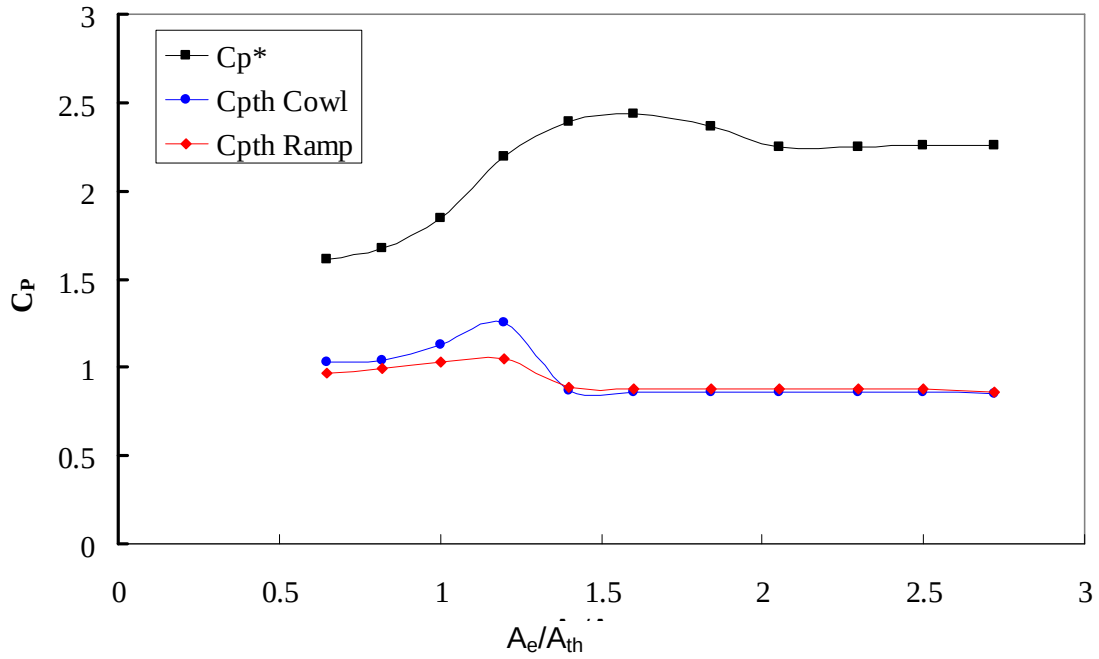

Fig. 7.8 Variation of Cp and Cp* with area ratio

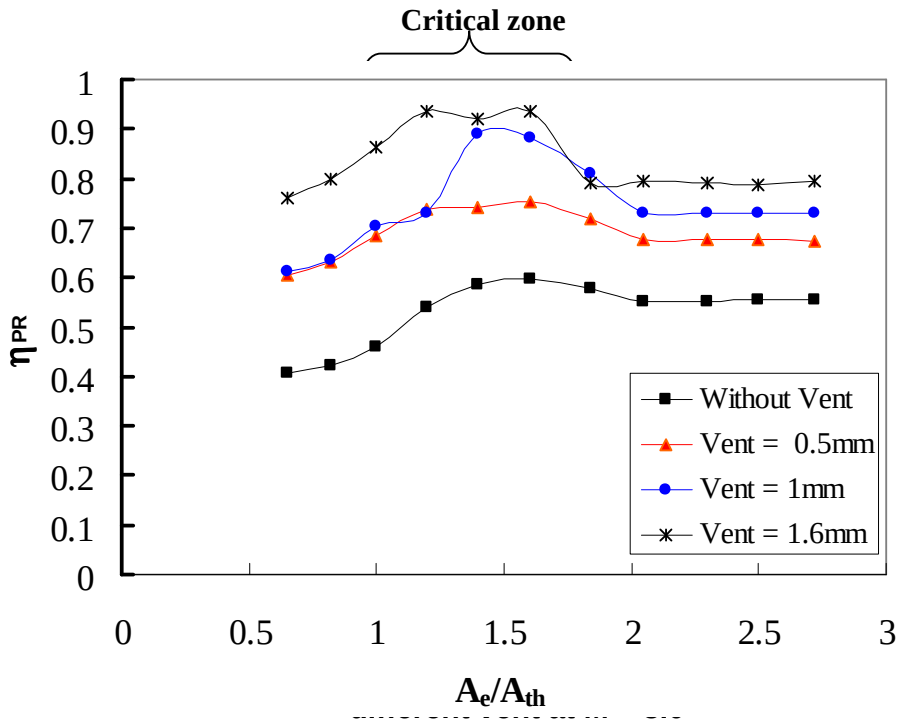

Fig. 7.9: Pressure distribution on ramp and pressure recovery efficiency, M = 3

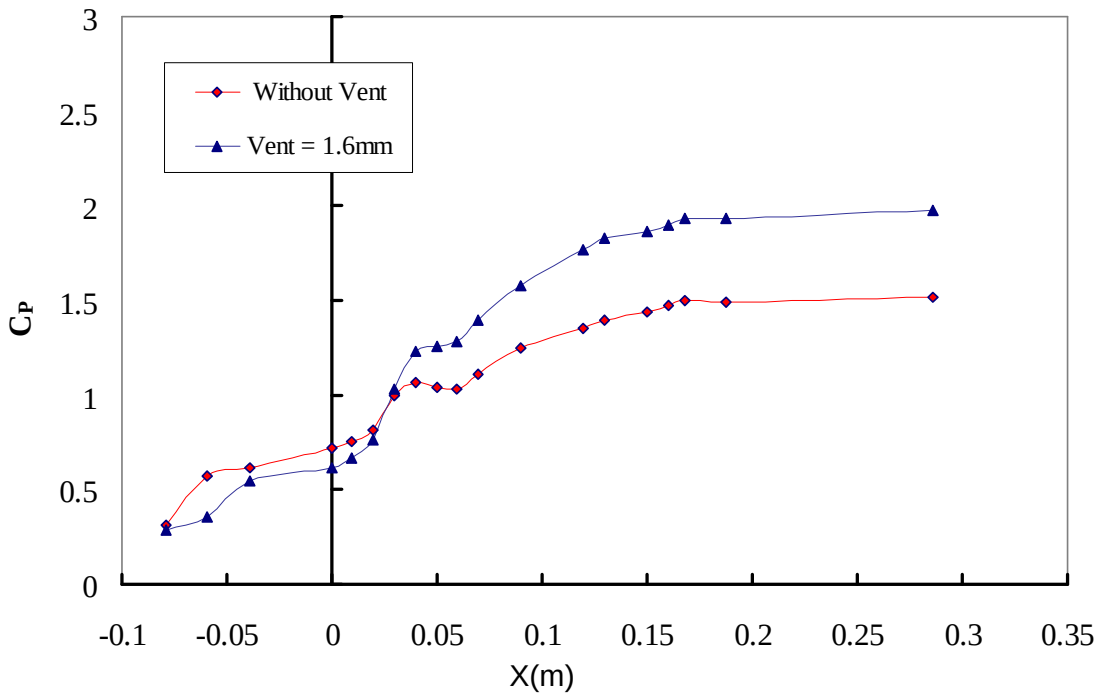

Fig. 7.10a Comparison of pressure distribution on ramp center line, A_e/A_{th} = 1, M = 3.0

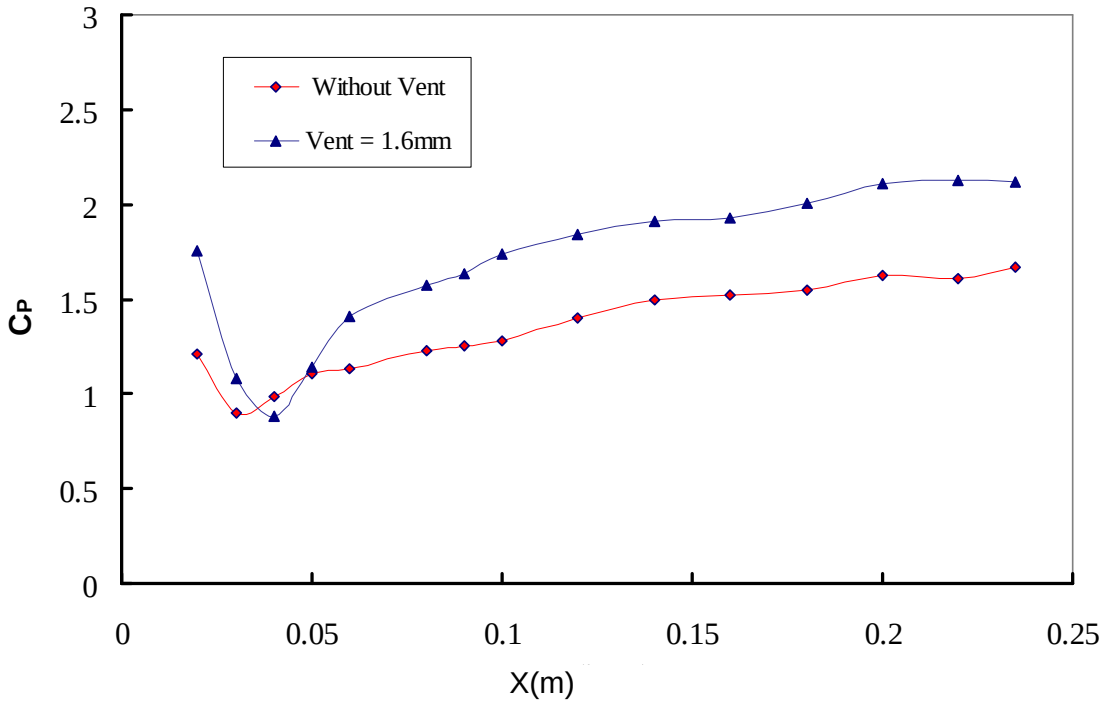

Fig. 7.10b Comparison of pressure distribution on cowl center line, A_e/A_{th} = 1, M = 3.0

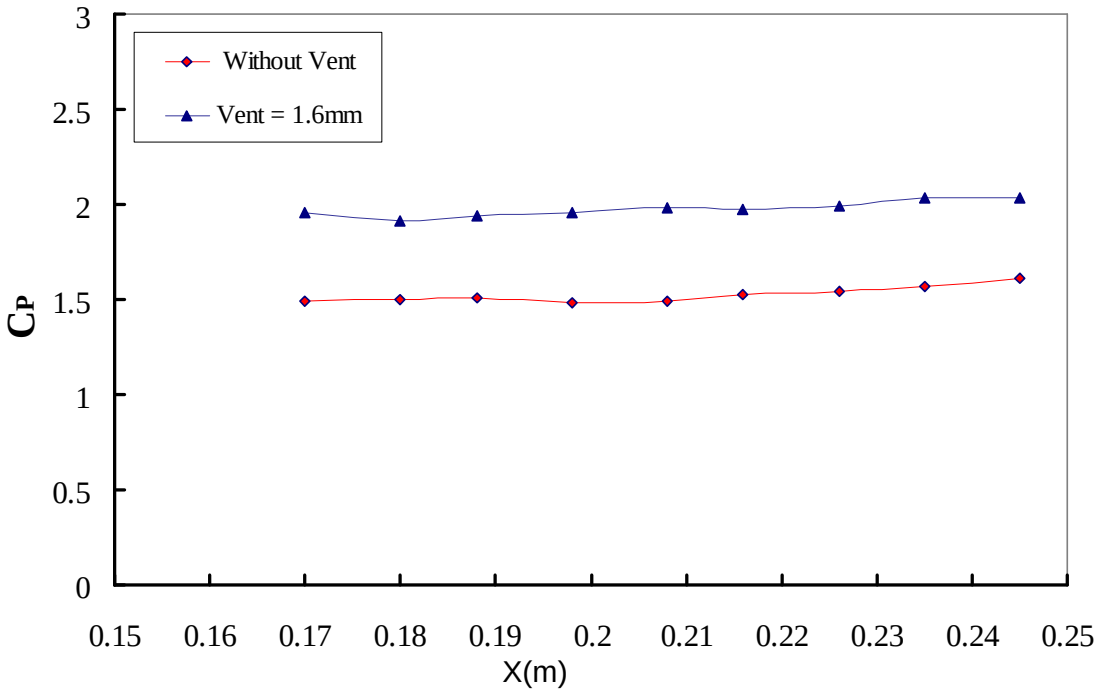

Fig. 7.10c Comparison of pressure distribution on side-plate, A_e/A_{th} = 1, M = 3.0

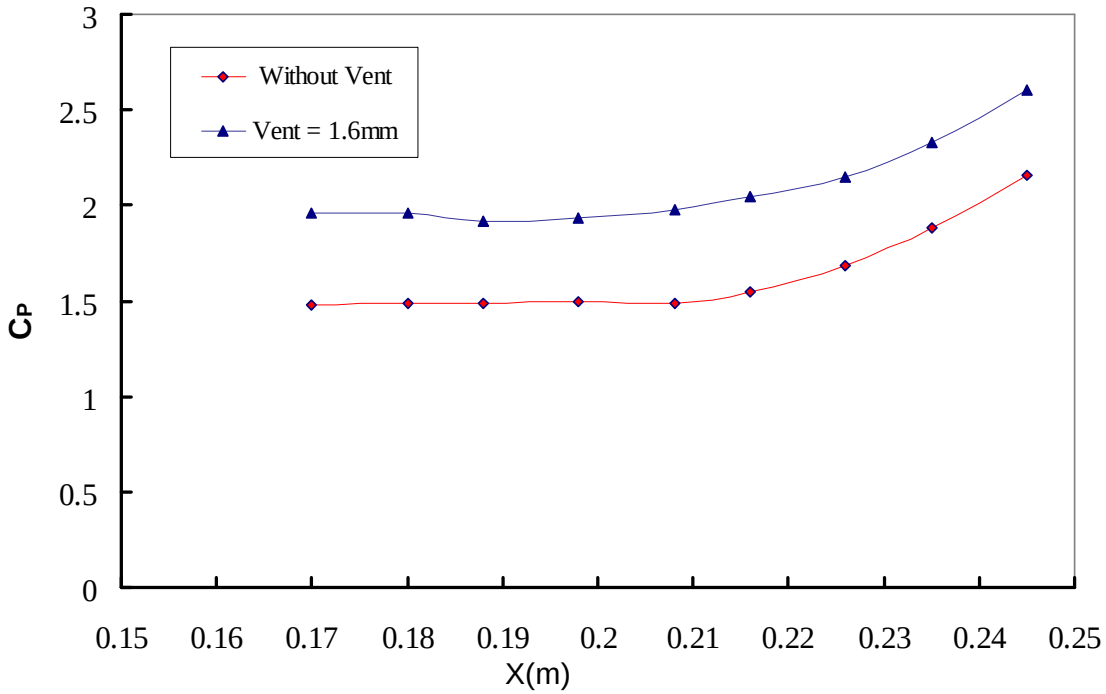

Fig. 7.10d Comparison of pressure distribution in dump-plane, A_e/A_{th} = 1, M = 3.0

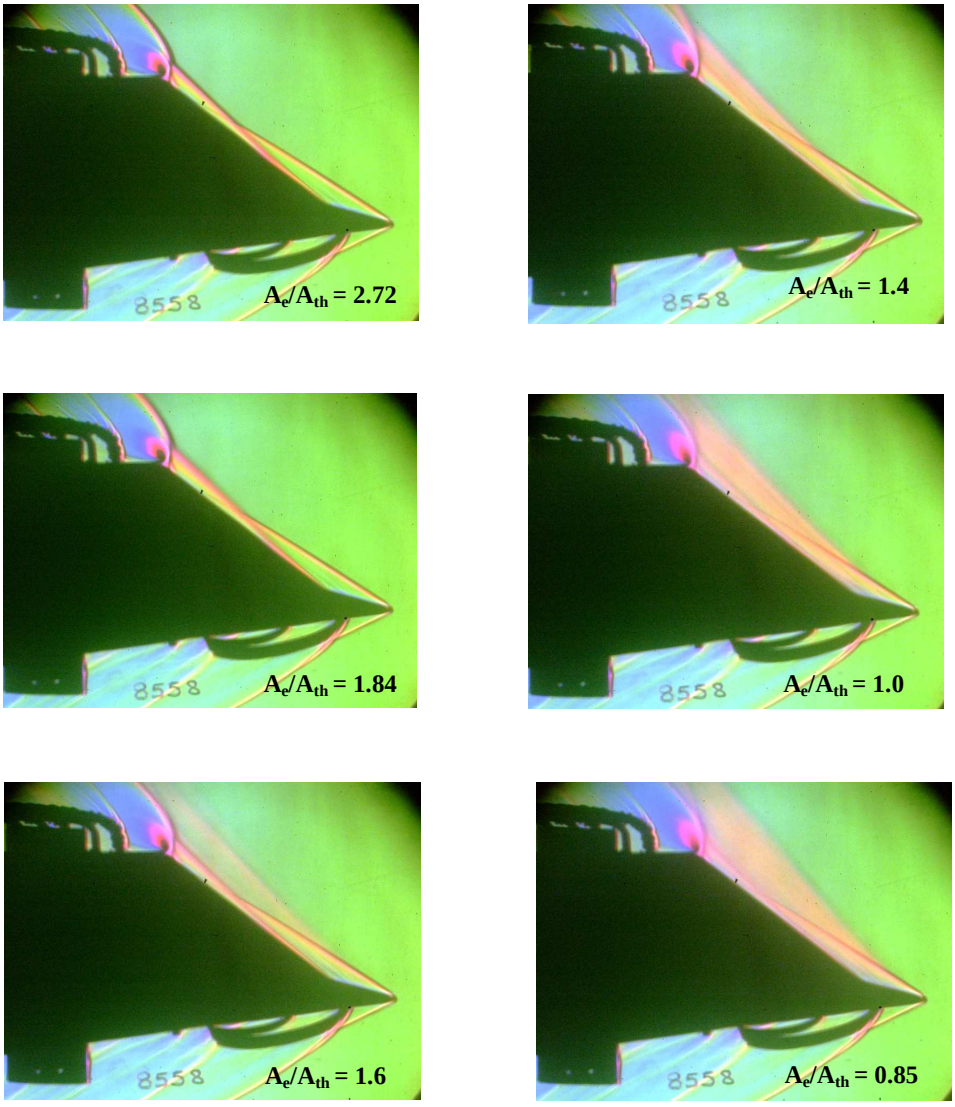

Fig. 7.11a: Schlieren photographs for various area ratios, M = 3.0

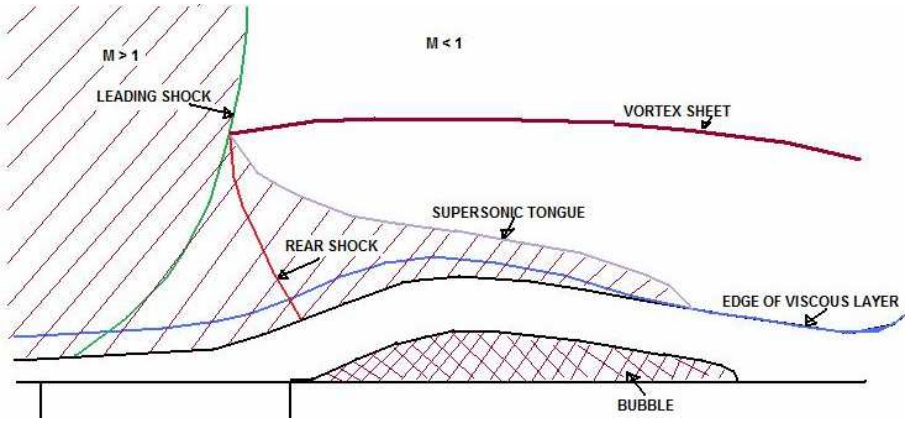

Fig. 7.11b: Features of interaction of shock and boundary layer interaction

A_e/A_{th} = 2.72

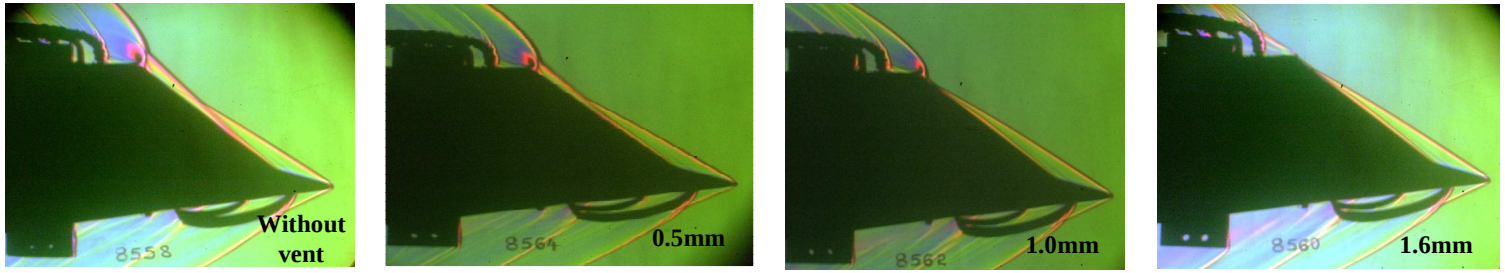

A_e/A_{th} = 1.84

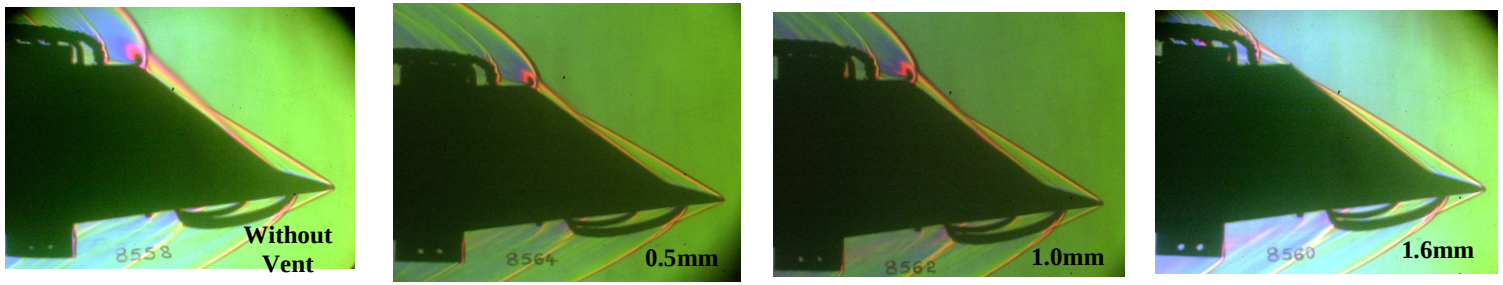

A_e/A_{th} = 1.1

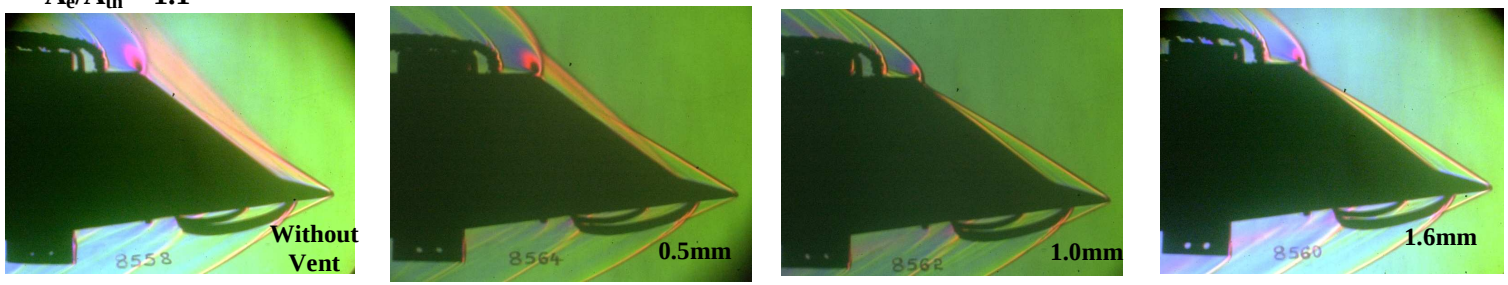

Fig. 7.11c: Schlieren photographs for various vent gaps at various area ratio, M = 3.0

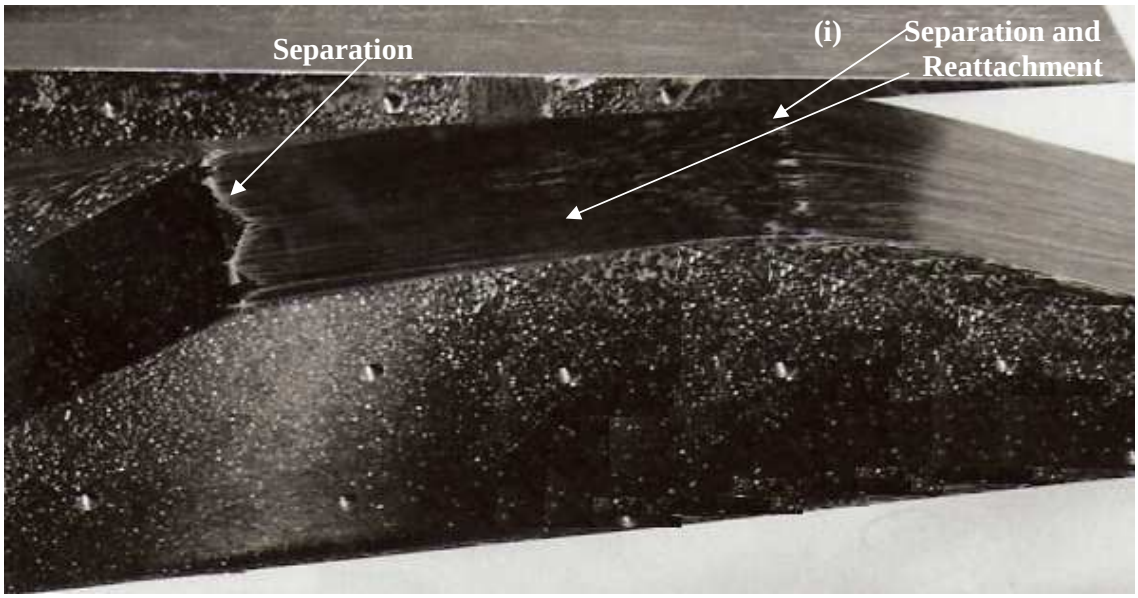

Fig. 7.12a Surface flow patterns on ramp at M = 3.0, Mach 3 ramp A_e/A_{th} = 2.98

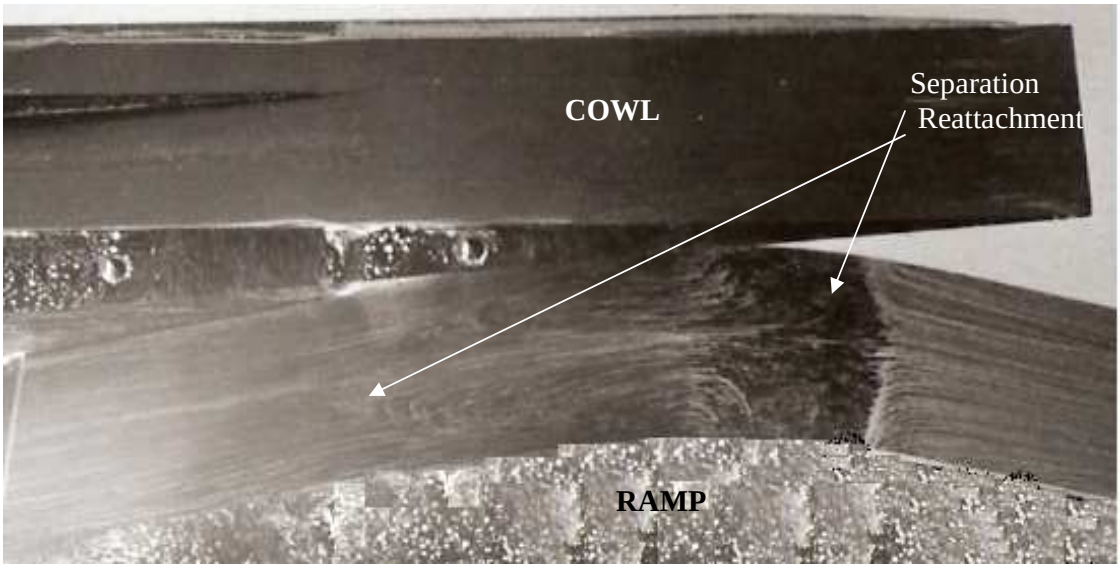

Fig. 7.12b Surface flow patterns on ramp at M = 3.0, Mach 3 ramp A_e/A_{th} = 1.0

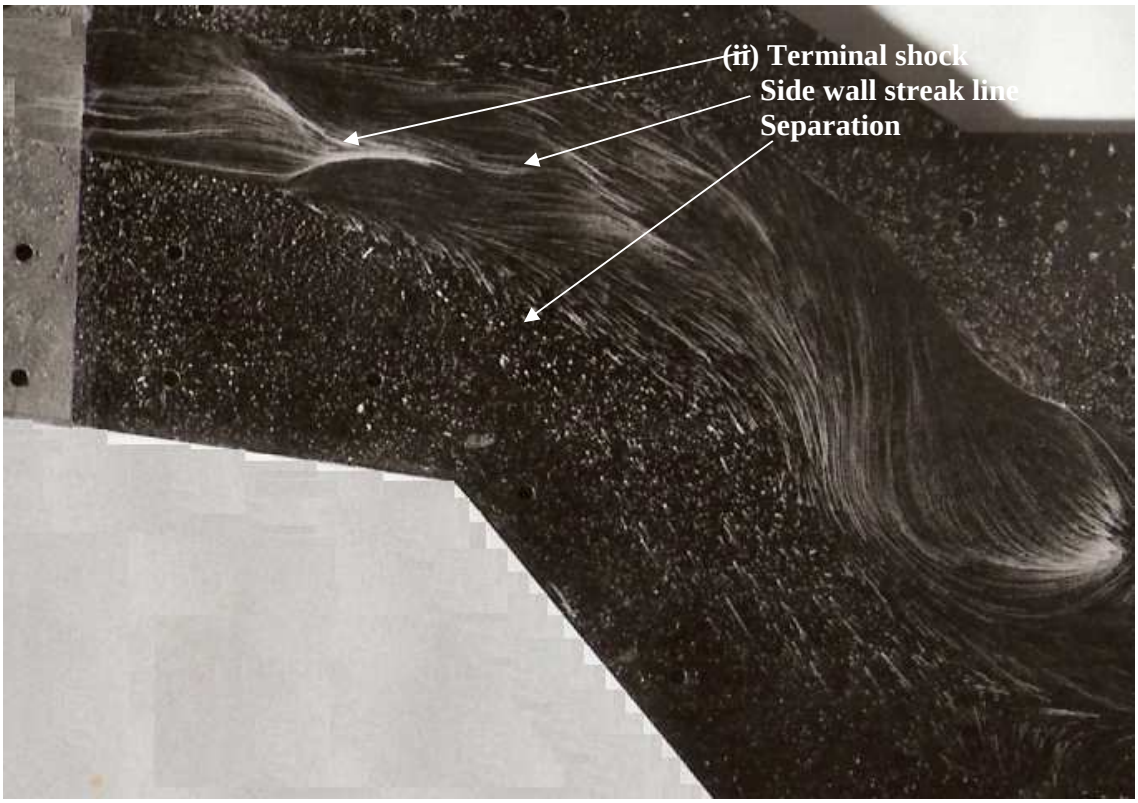

Fig. 7.12c Surface flow patterns on side wall at M = 3.0, Mach 3 ramp A_e/A_{th} = 2.98

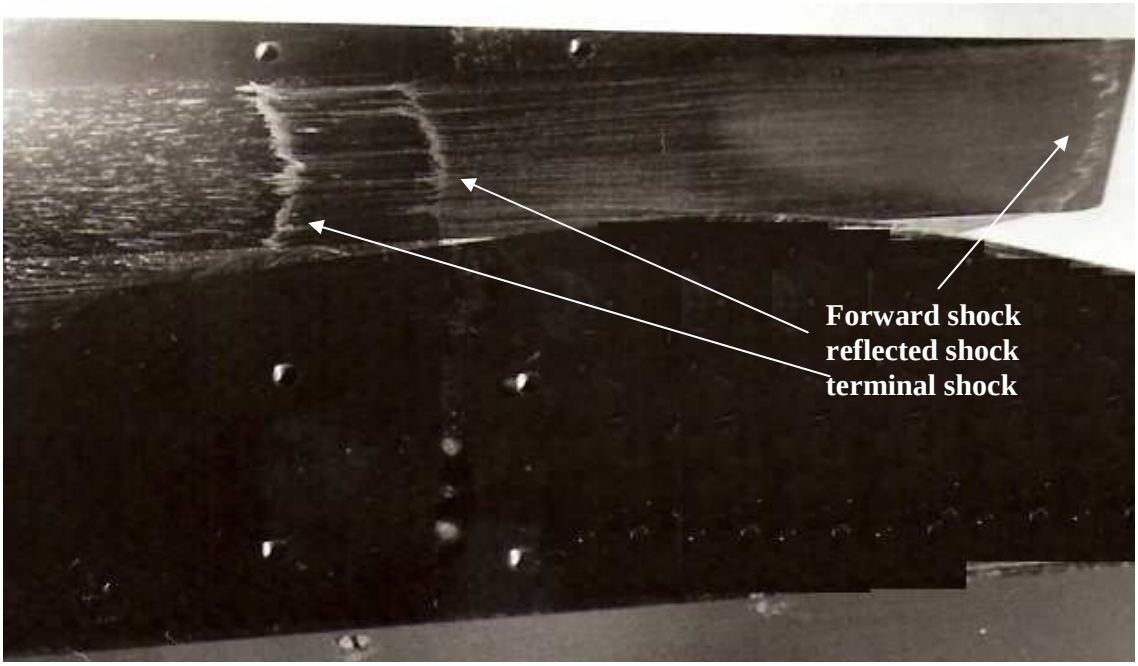

Fig. 7.12d Surface flow patterns at M = 3.0, Mach 3 ramp A_e/A_{th} = 2.67

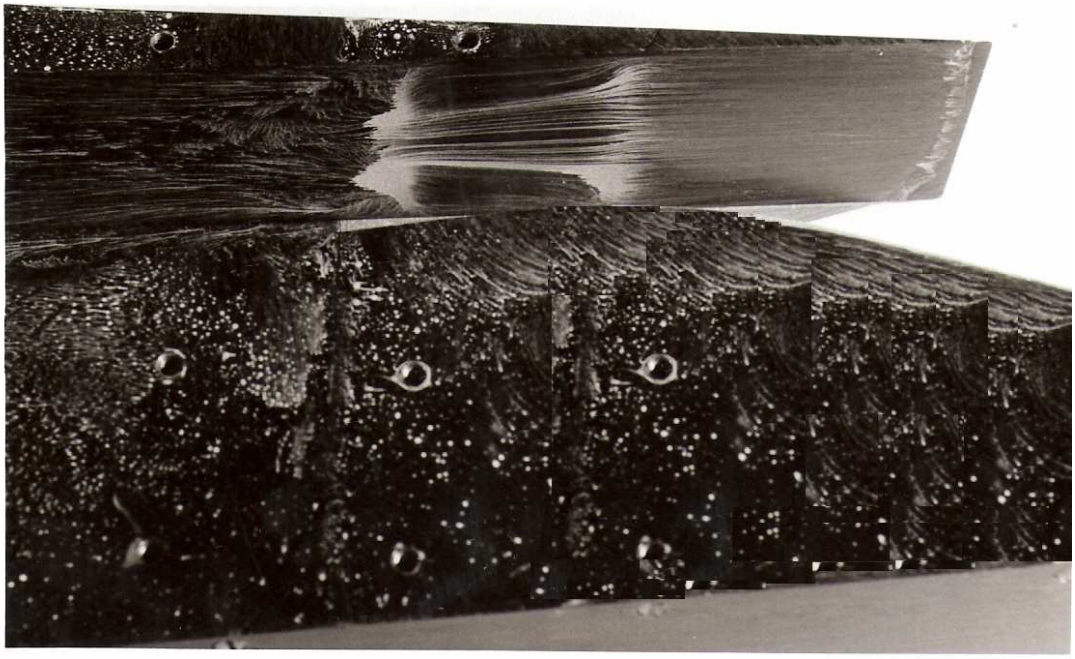

Fig. 7.12e Surface flow patterns at M = 3.0, Mach 3 ramp A_e/A_{th} = 0.99

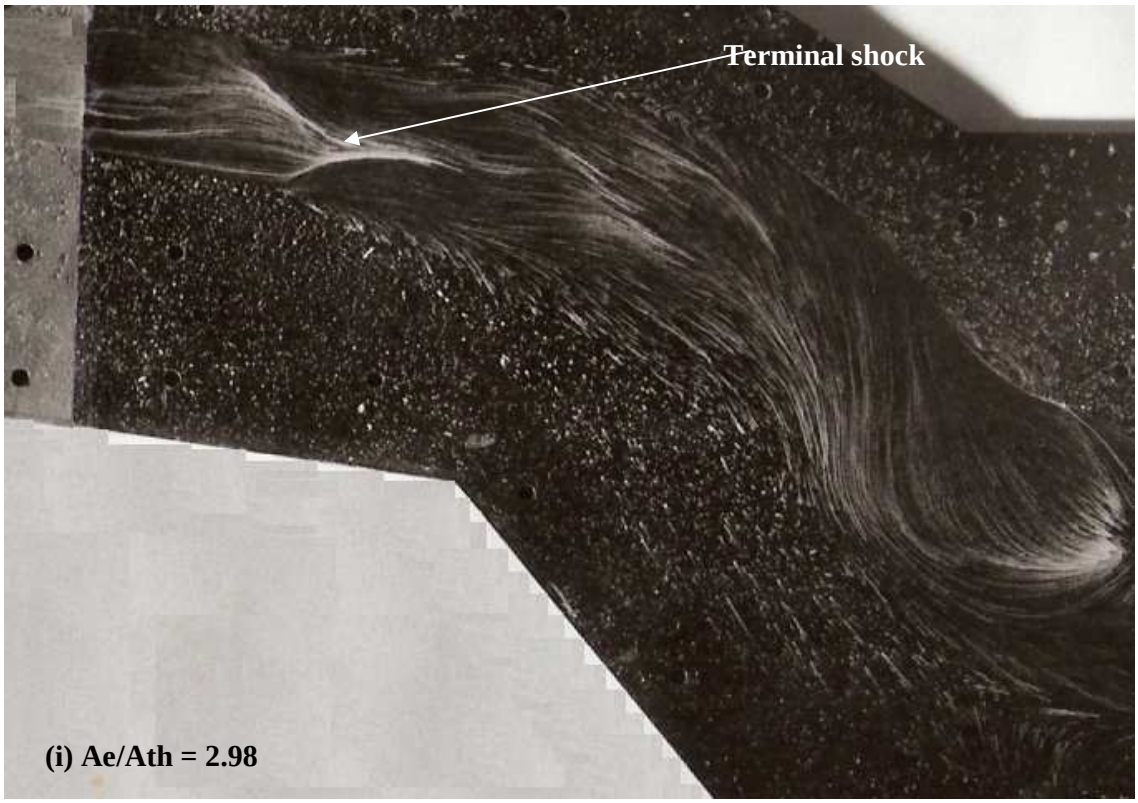

(i) Ae/Ath = 2.98

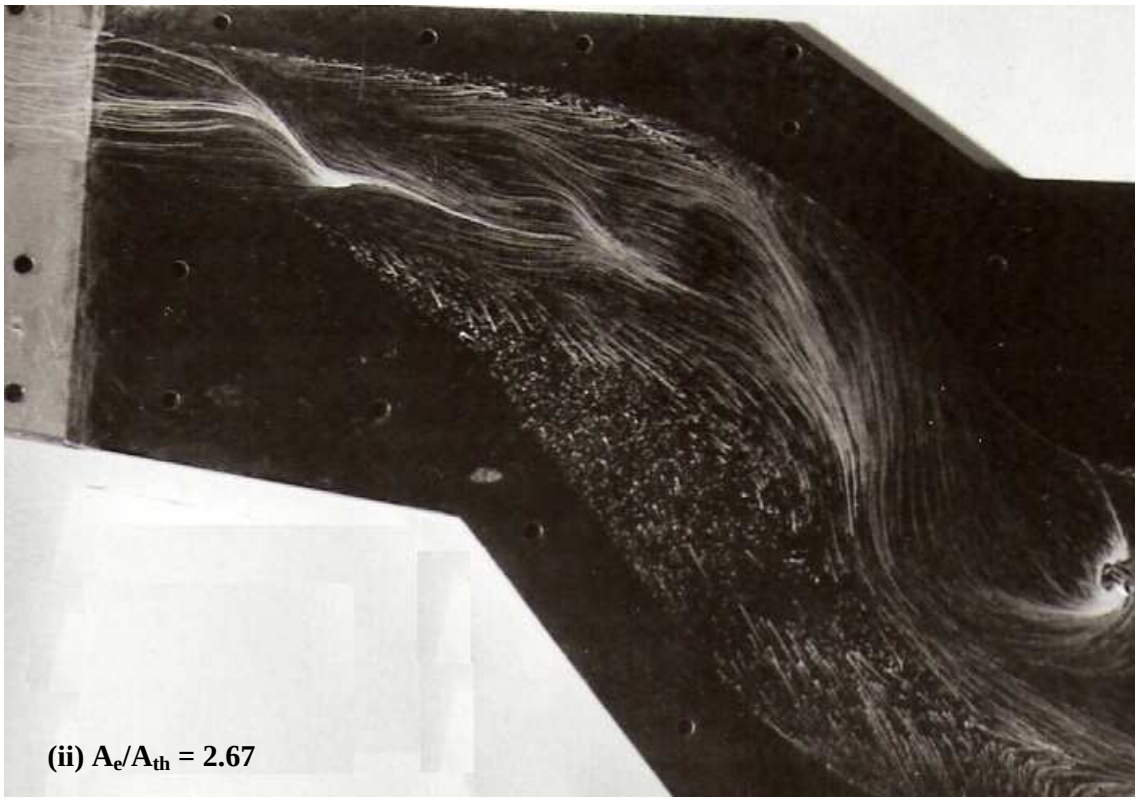

(ii) A_e/A_{th} = 2.67

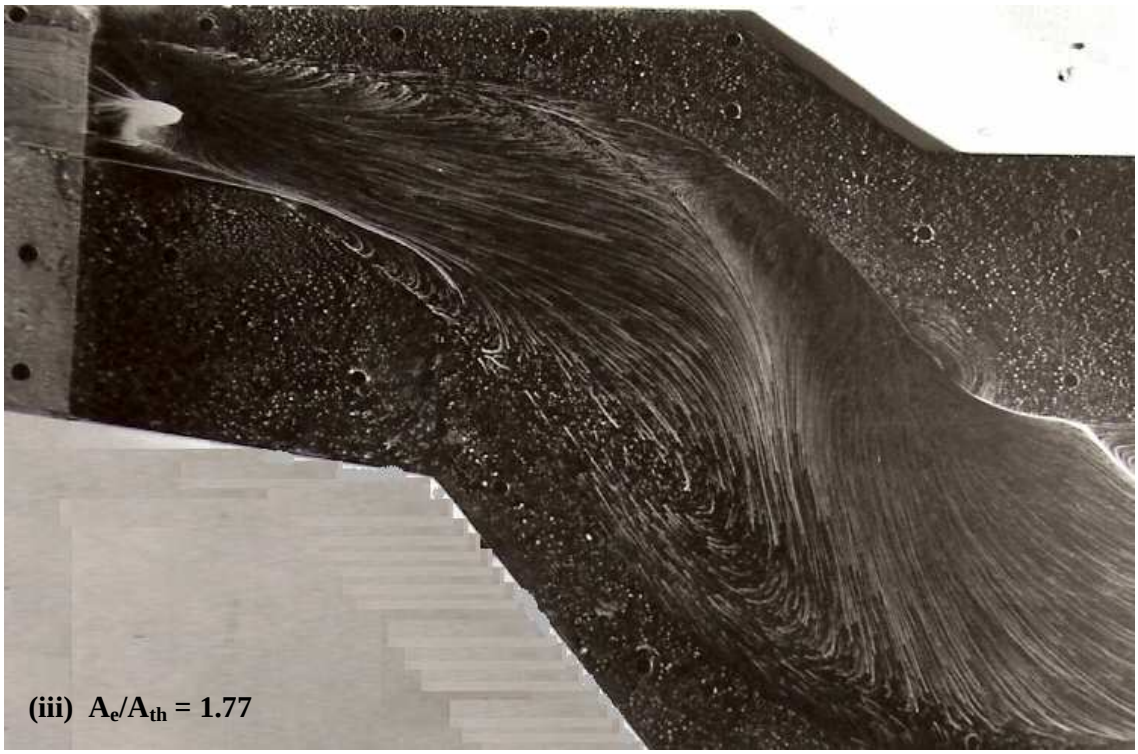

Fig. 7.12f Traces of terminal shock for different area ratios, M = 3.0

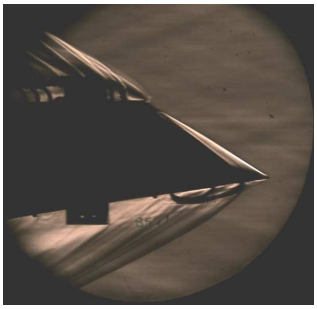

t = 0

t = 3 msec

t = 6.5 msec

t = 1 msec

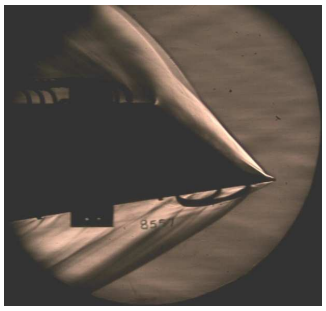

t = 4 msec

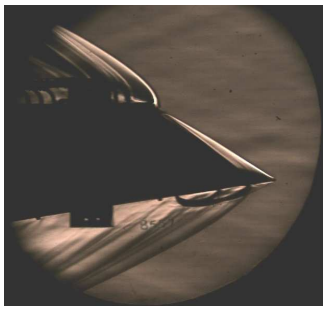

t = 8 msec

t = 2 msec

t = 5 msec

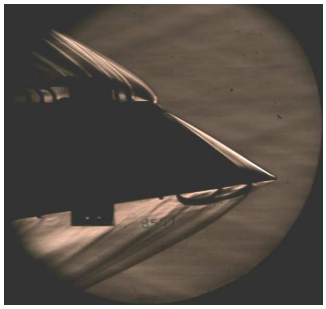

t = 9 msec

t = 2.5 msec

t = 6 msec

t = 10 msec

Fig. 7.13 Shock oscillation for sub critical operation at different time instant

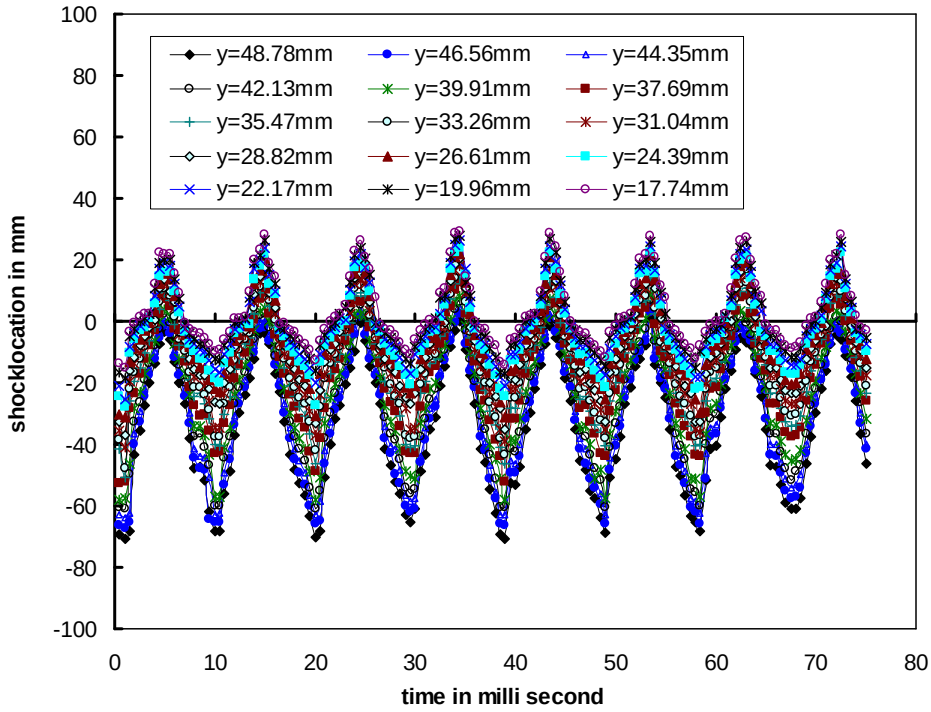

Fig. 7.14a Shock location from the cowl lip at different time instants

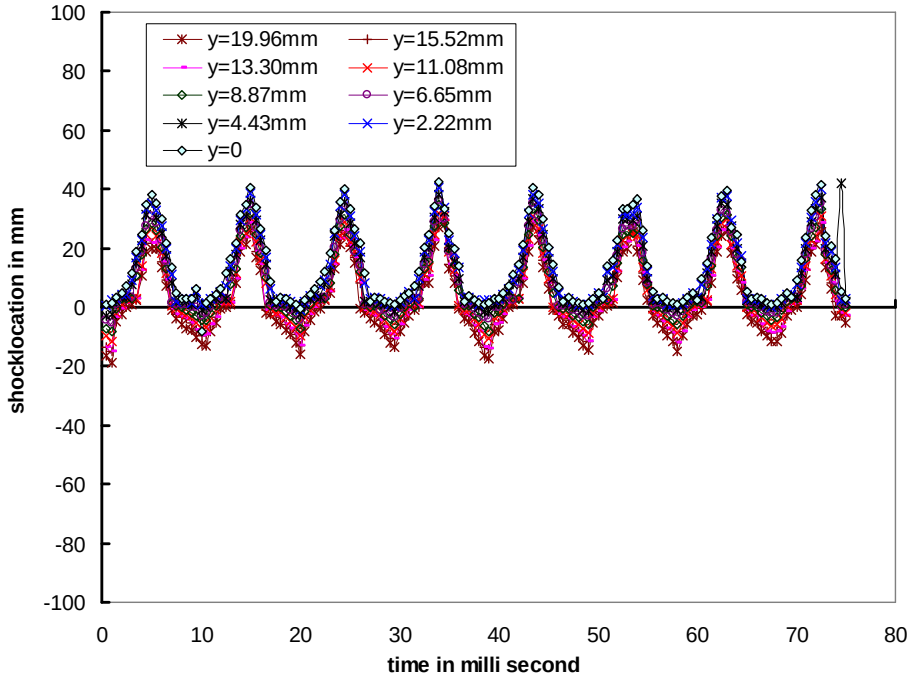

Fig. 7.14b Shock location from the cowl lip at different time instants

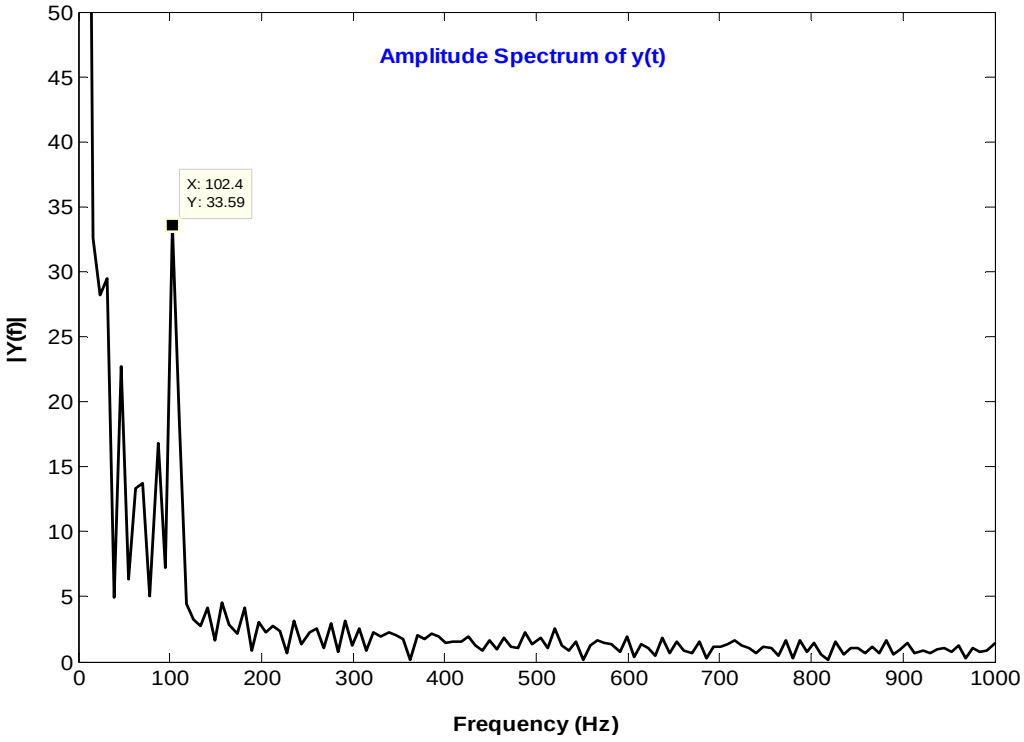

Fig. 7.14c Amplitude spectrum

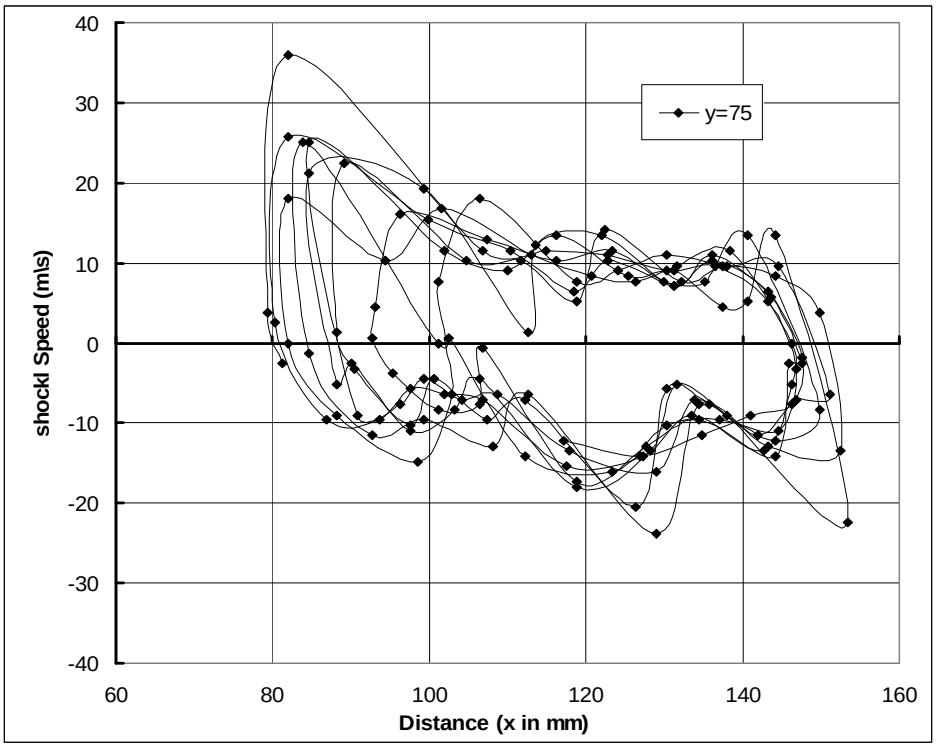

Fig. 7.14d Limit cycle oscillation

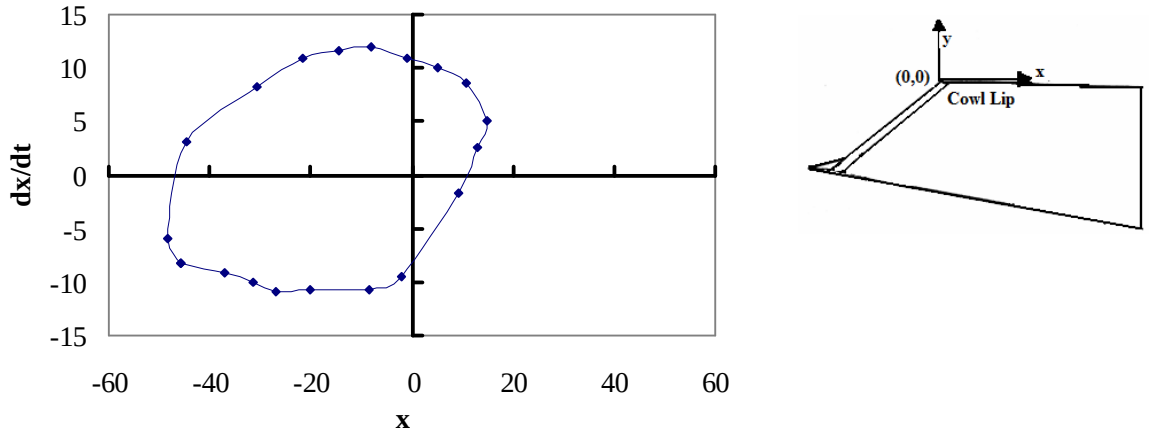

Fig. 7.14e Phase plane diagram for buzz by averaging seven cycles

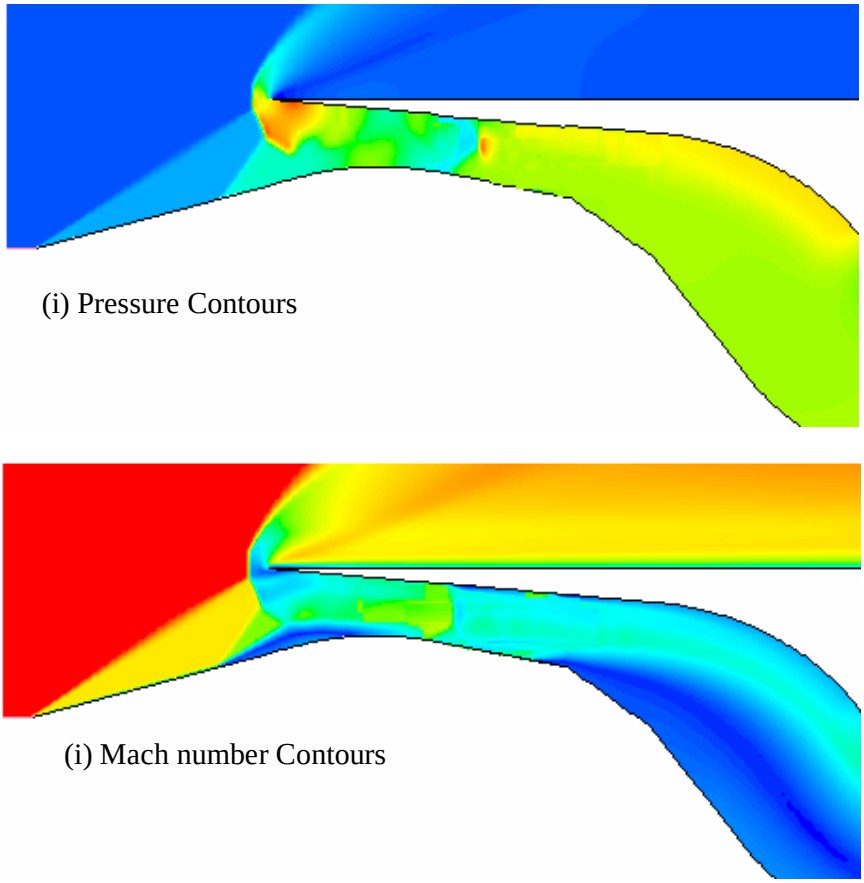

(i) Pressure Contours

(i) Mach number Contours

Fig. 7.15a Contours of static pressure and Mach number, M = 3, Pb =10Pi

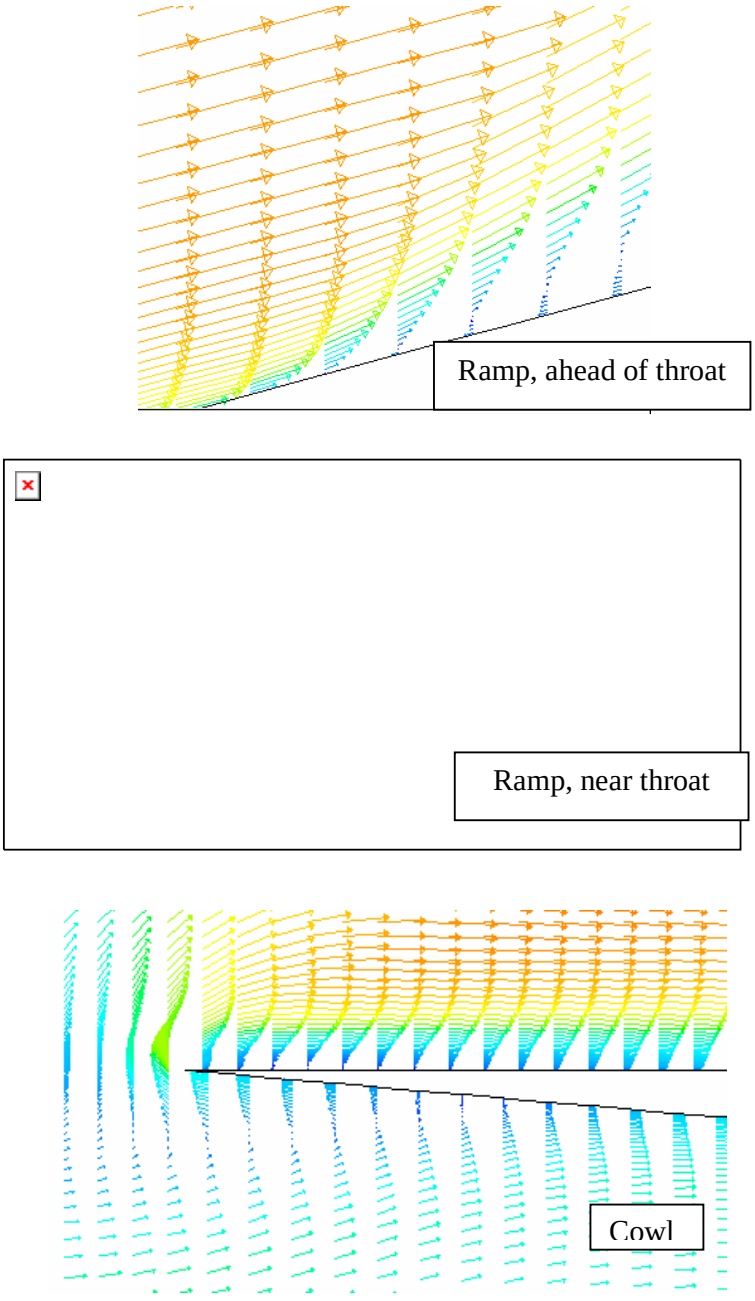

Fig. 7.15b Velocity vector at the ramp and cowl, Pb = 10Pi

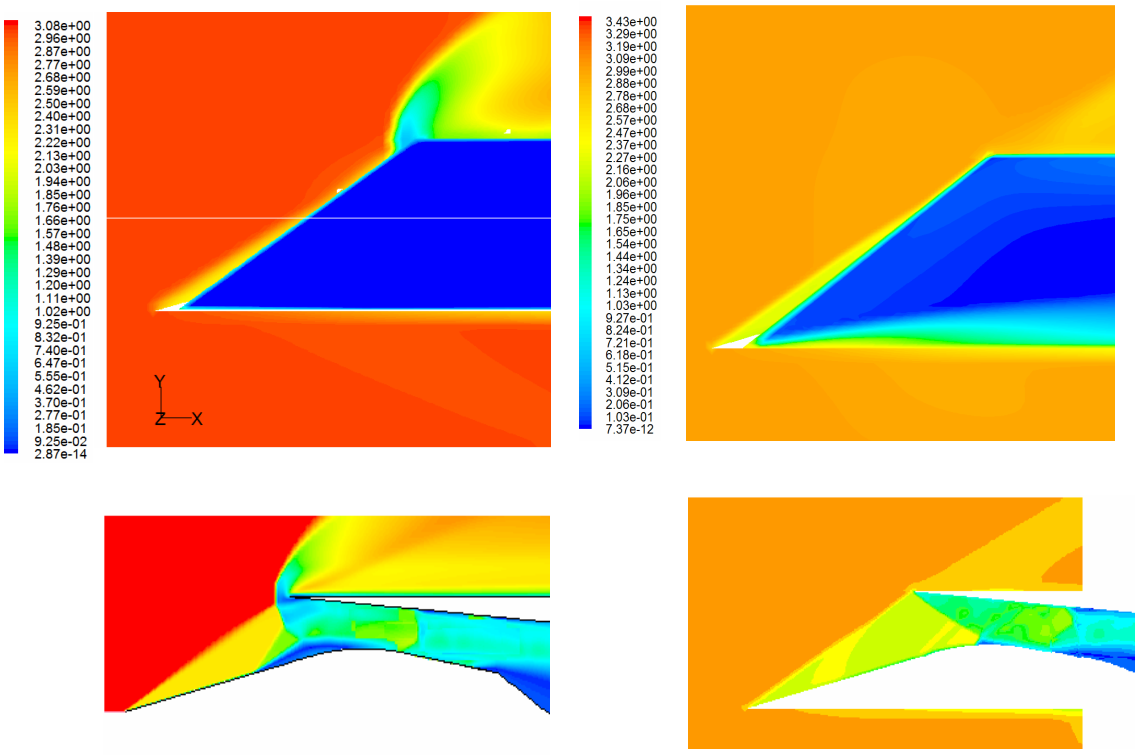

Without vent With 1.6mm vent

Fig. 7.15c Mach contours with and without ventilation: M = 3, Pb = 10Pi

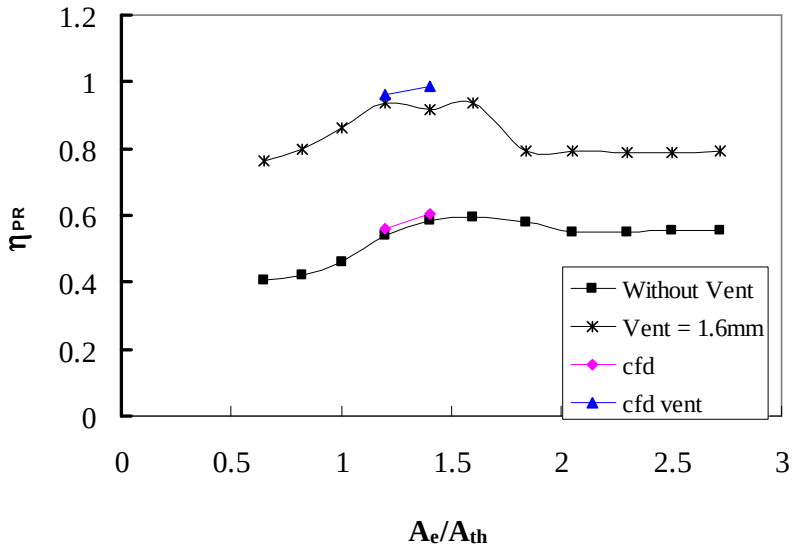

Fig. 7.15d Comparison of pressure recovery with and without ventilation, M =3

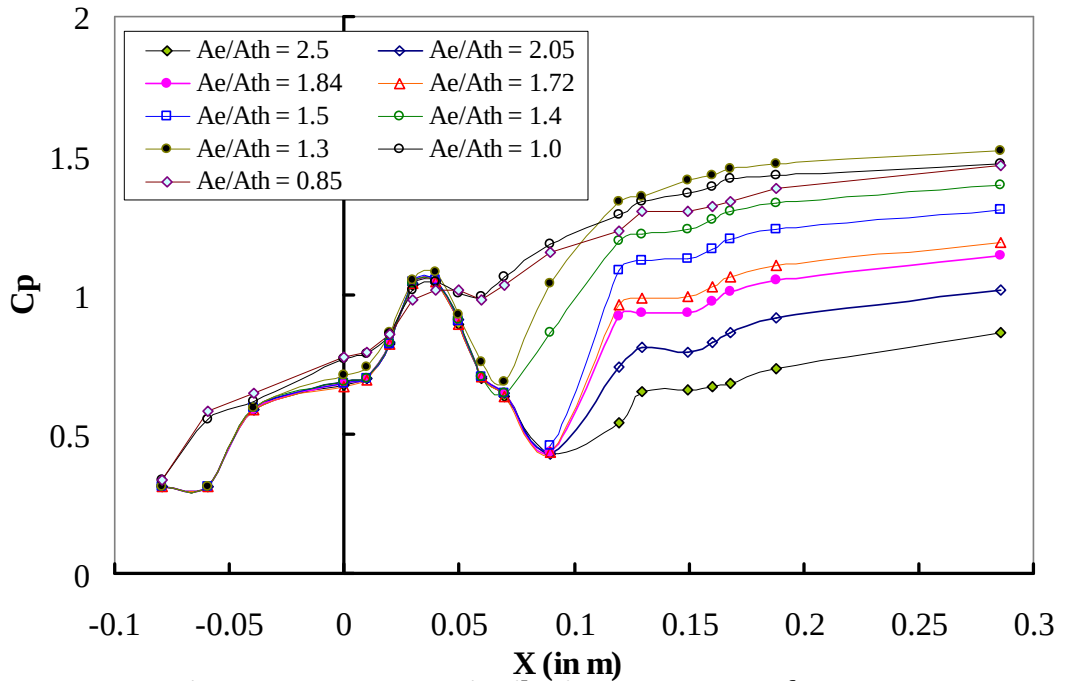

Fig. 7.16a Pressure distribution on ramp surface, M = 2.5

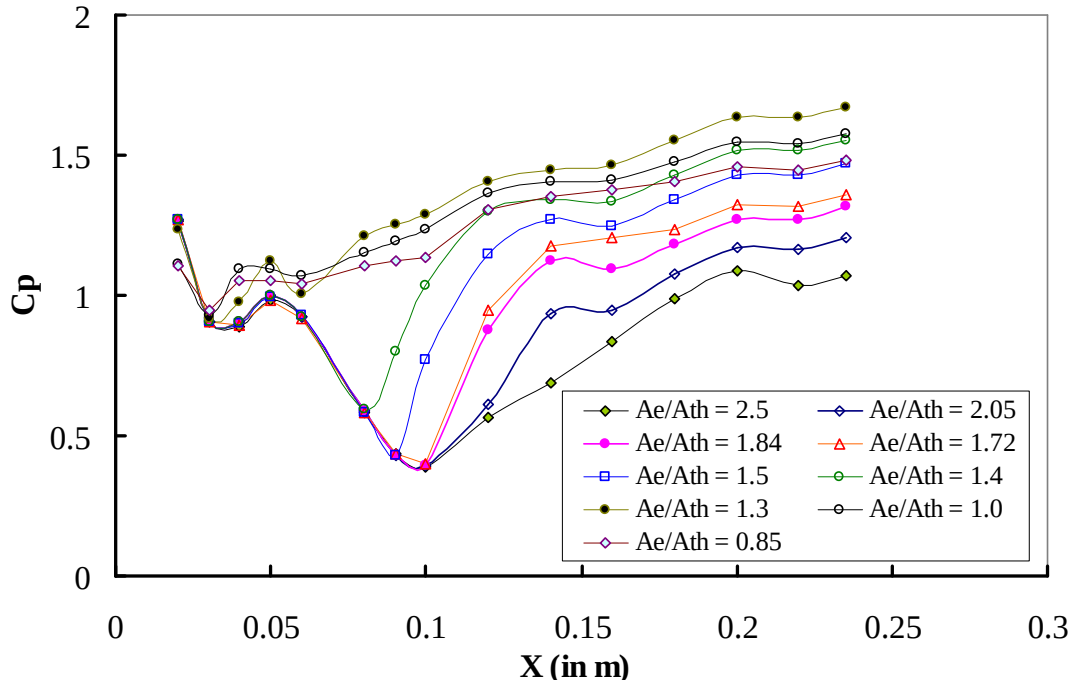

Fig. 7.16b Pressure distribution on cowl surface, M = 2.5

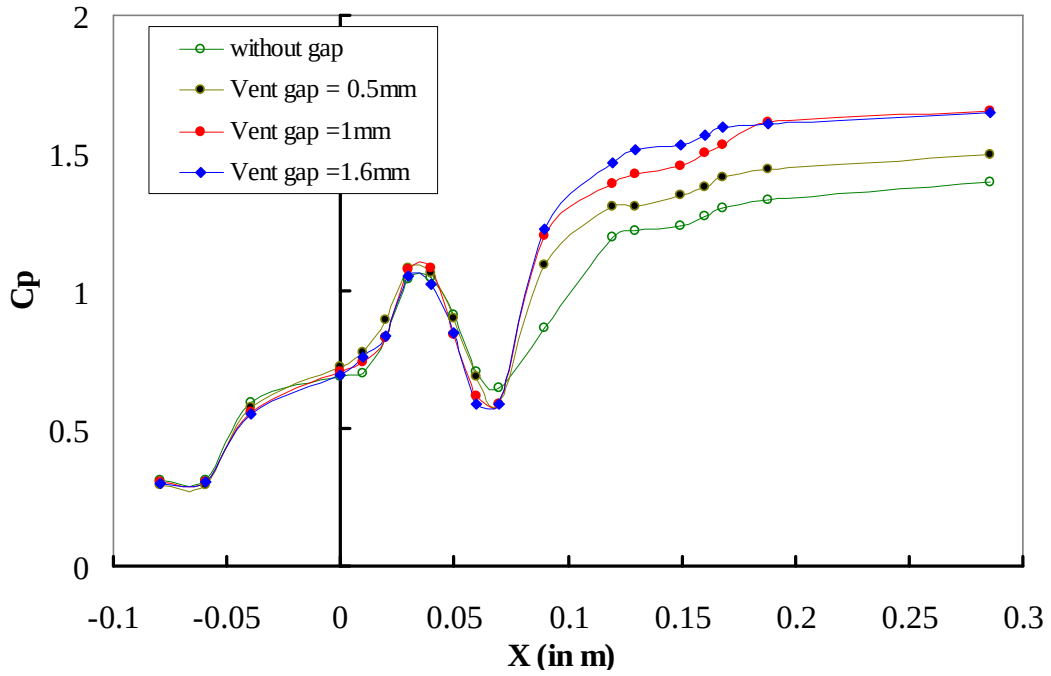

Fig. 7.17a Effect of ventilation on pressure distribution at ramp surface, A_e/A_{th} = 1.4

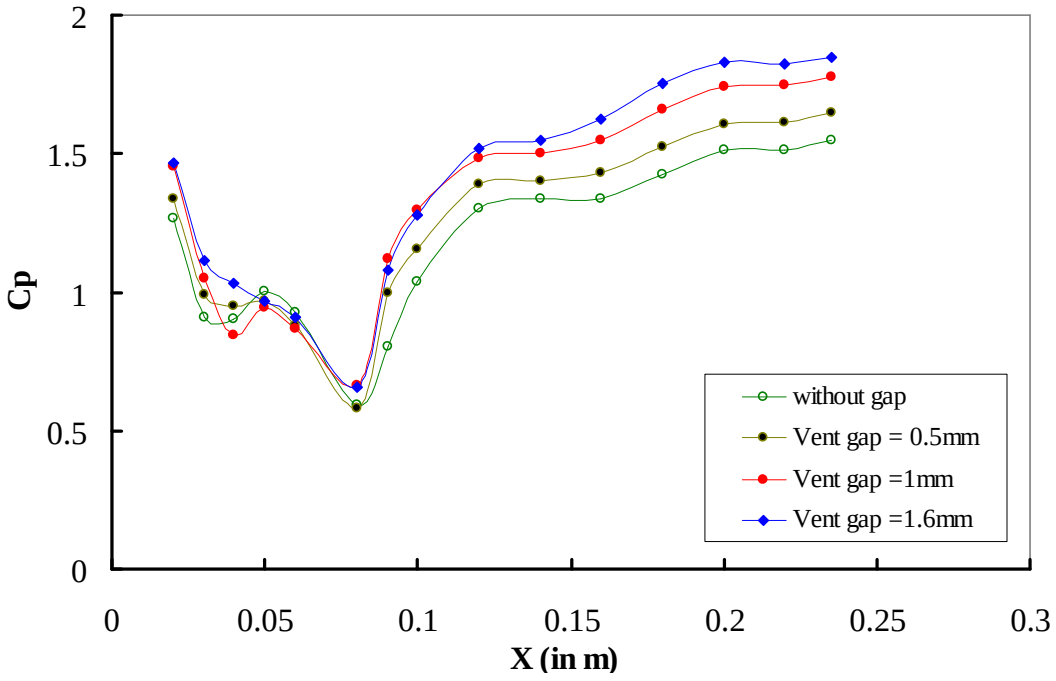

Fig. 7.17b Effect of ventilation on pressure distribution at cowl surface, A_e/A_{th} = 1.4

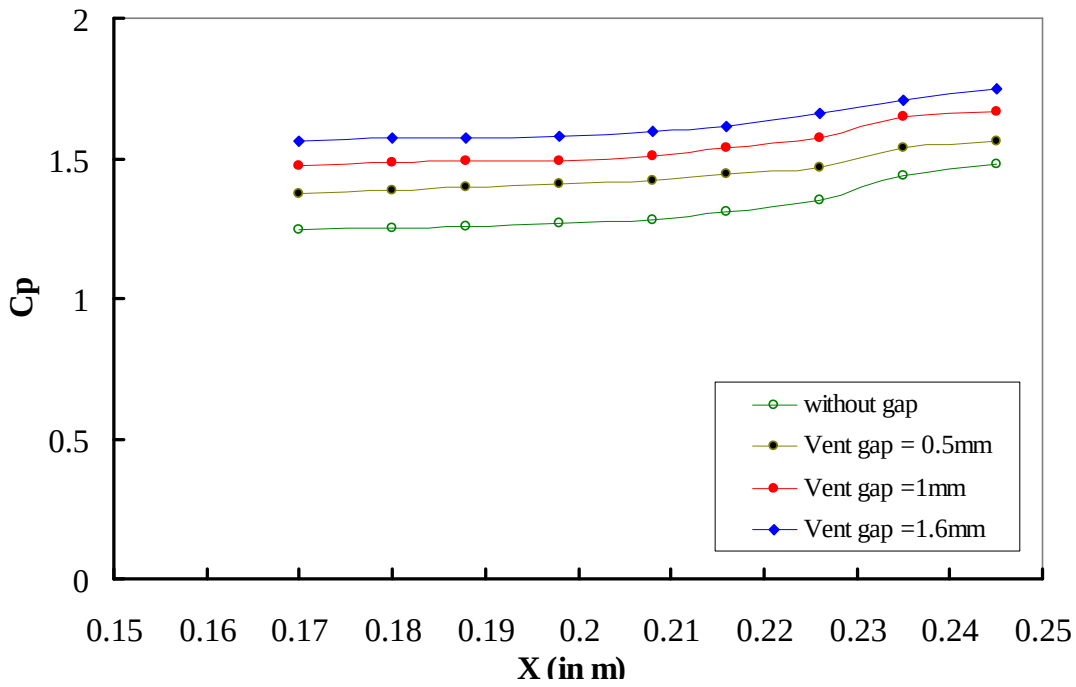

Fig. 7.17c Effect of ventilation on pressure distribution at side plate, A_e/A_{th} = 1.4

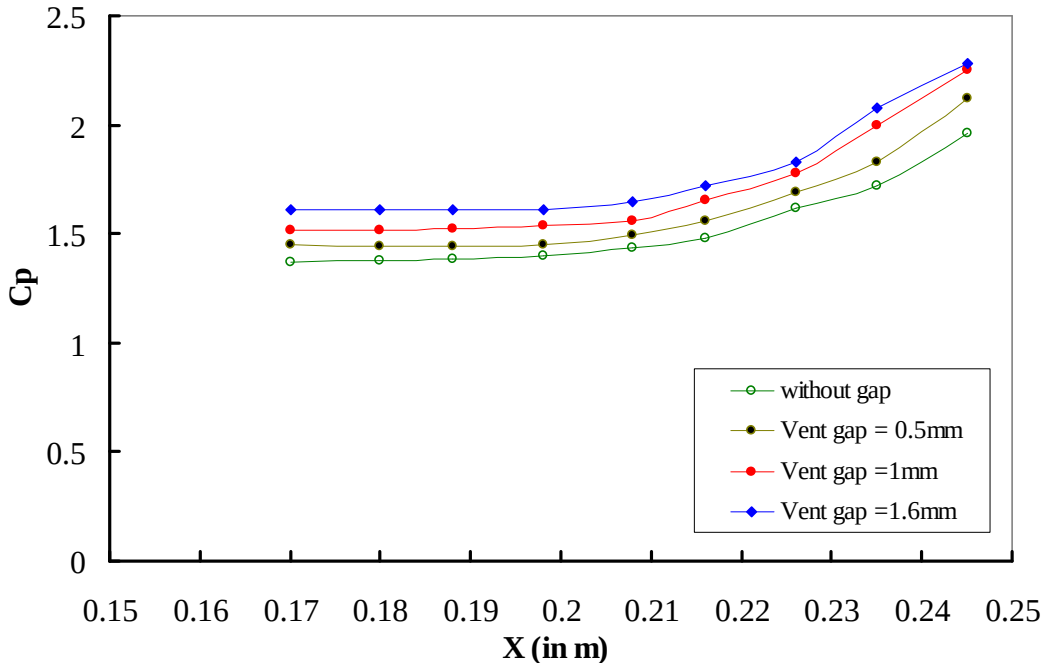

Fig. 7.17d Effect of ventilation on pressure distribution in dump plane, A_e/A_{th} = 1.4

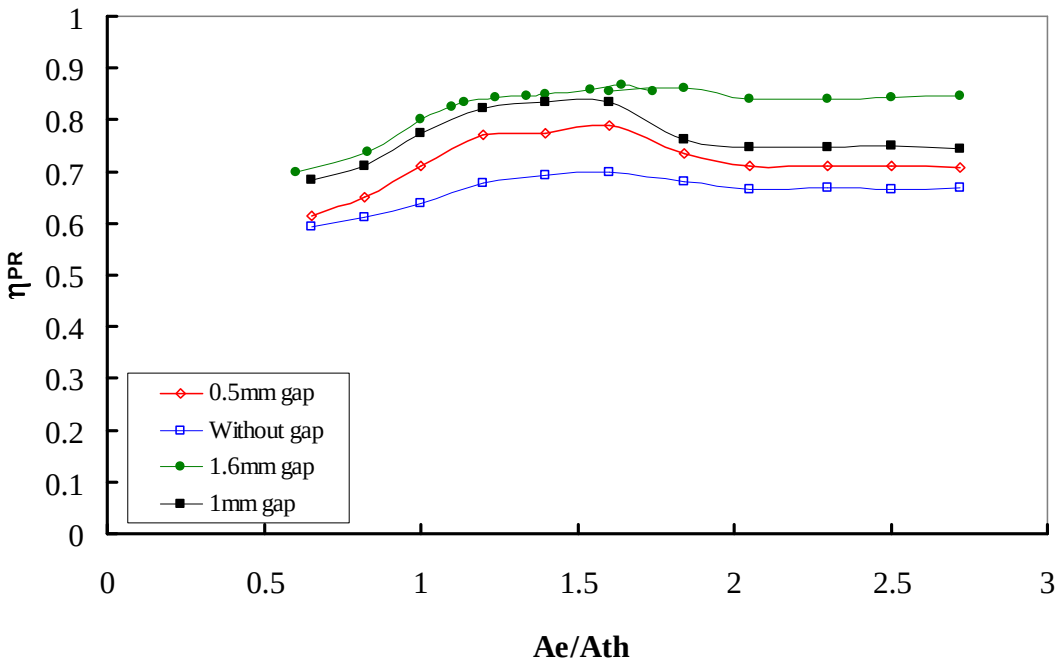

Fig. 7.17e Effect of ventilation on pressure recovery for various area ratio

A_e/A_{th} = 2.72

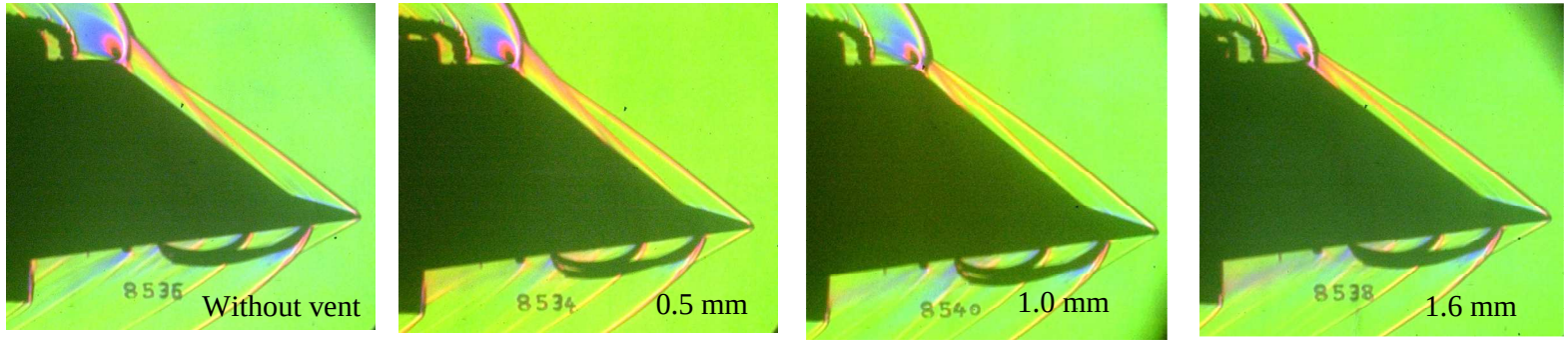

A_e/A_{th} = 1.6

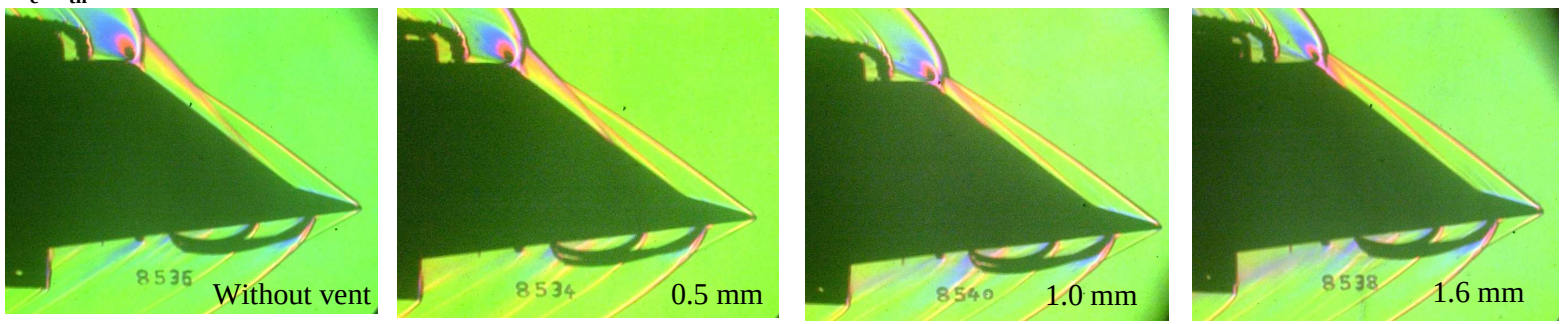

A_e/A_{th} = 1.0

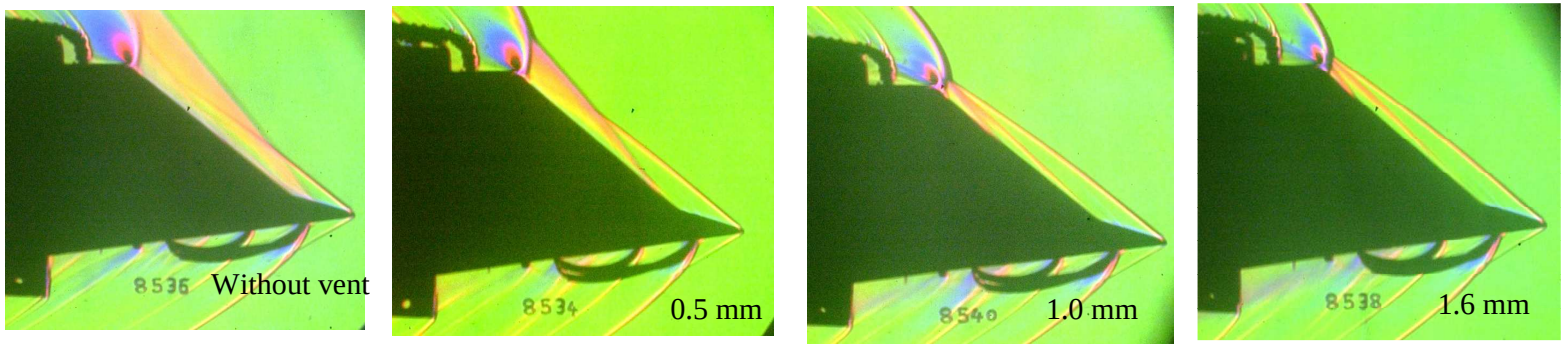

Fig. 7.18: Shock pattern obtained from schlieren for different vent gap at selected area ratios, M=2.5

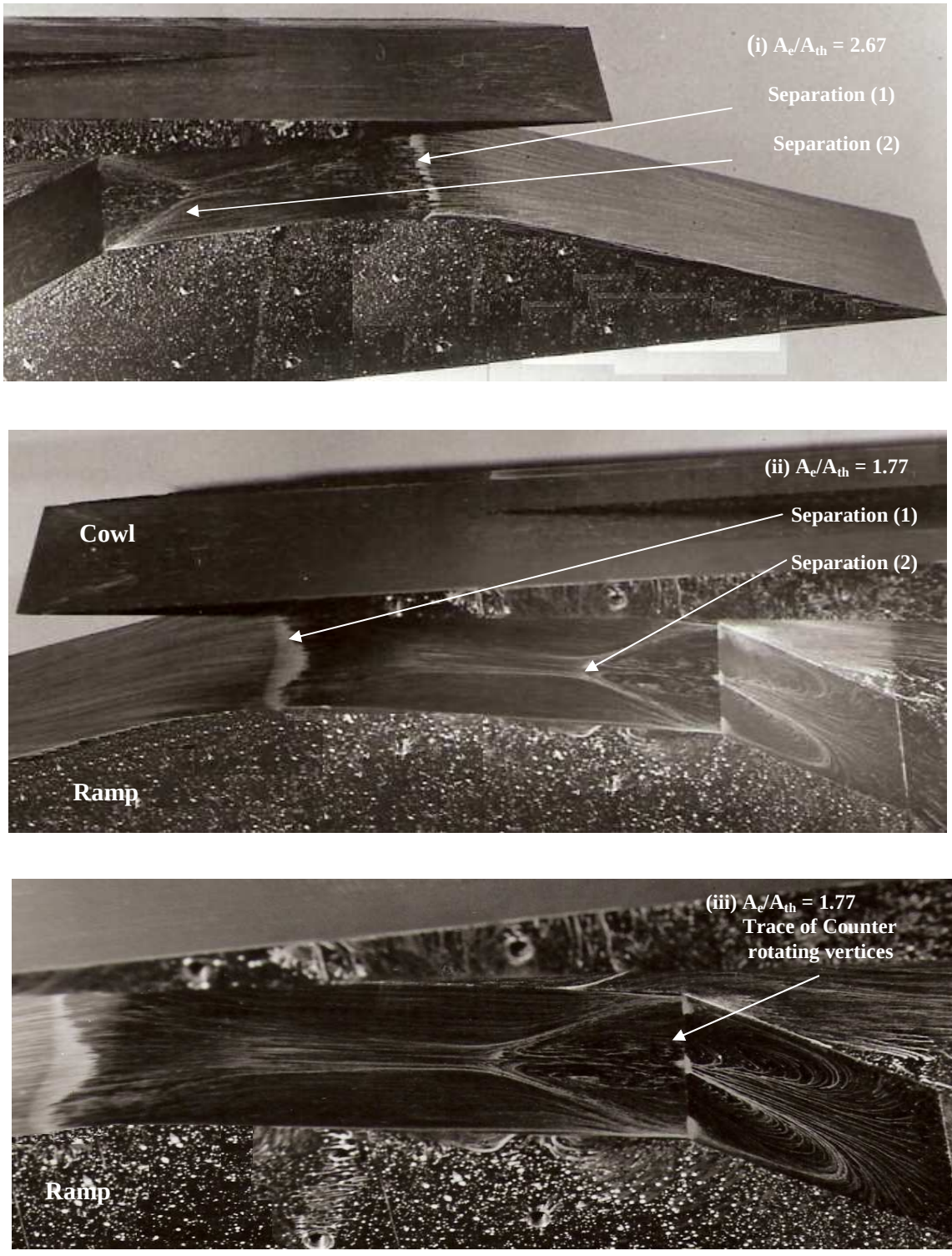

Fig. 7.19a : Surface oil flow patterns on ramp M = 2.5, Mach 3 Ramp

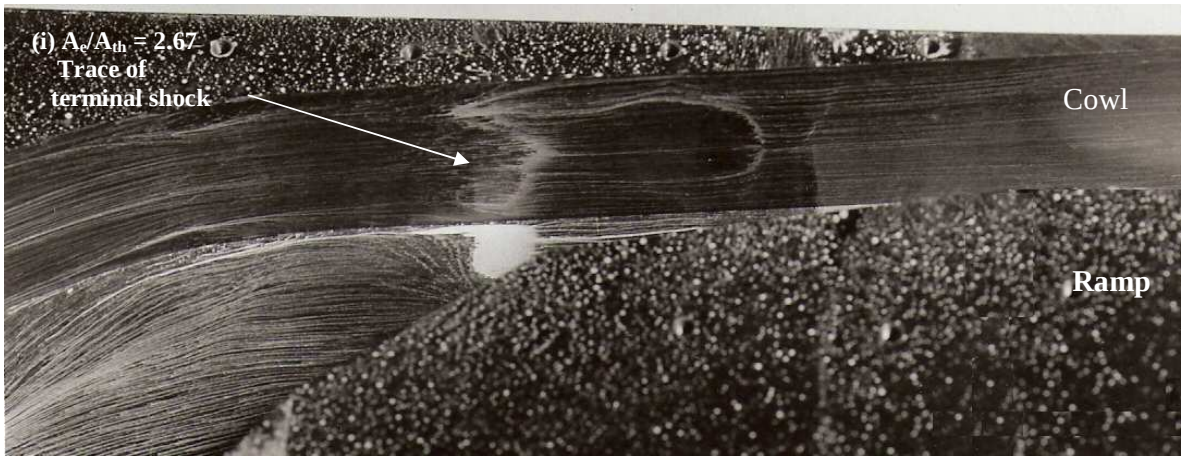

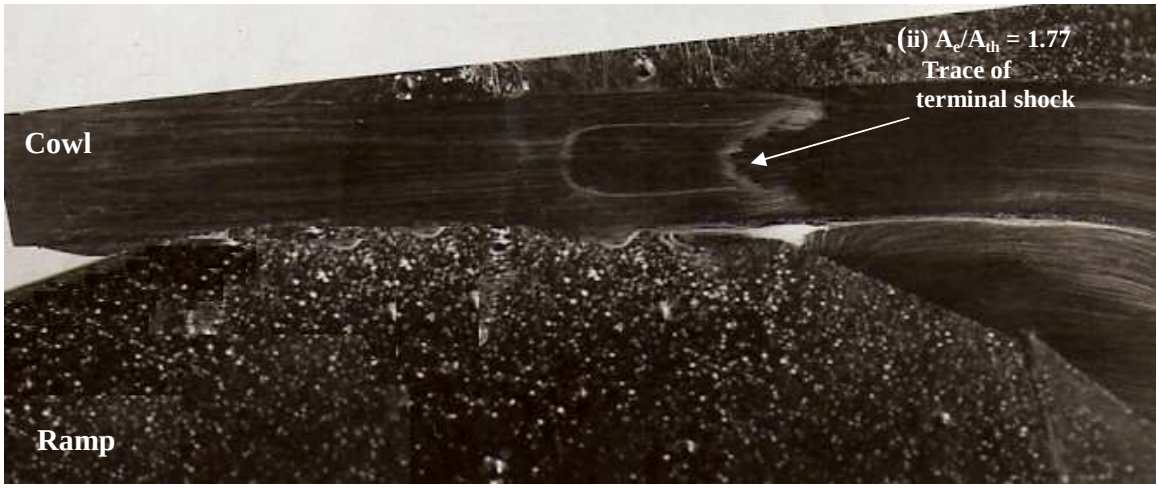

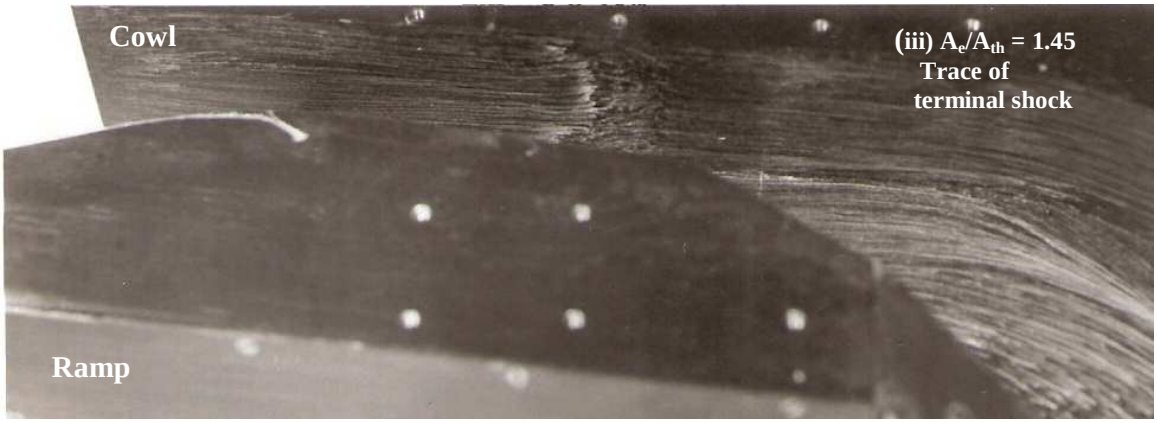

Fig. 7.19b : Surface oil flow patterns on cowl M = 2.5, Mach 3 Ramp

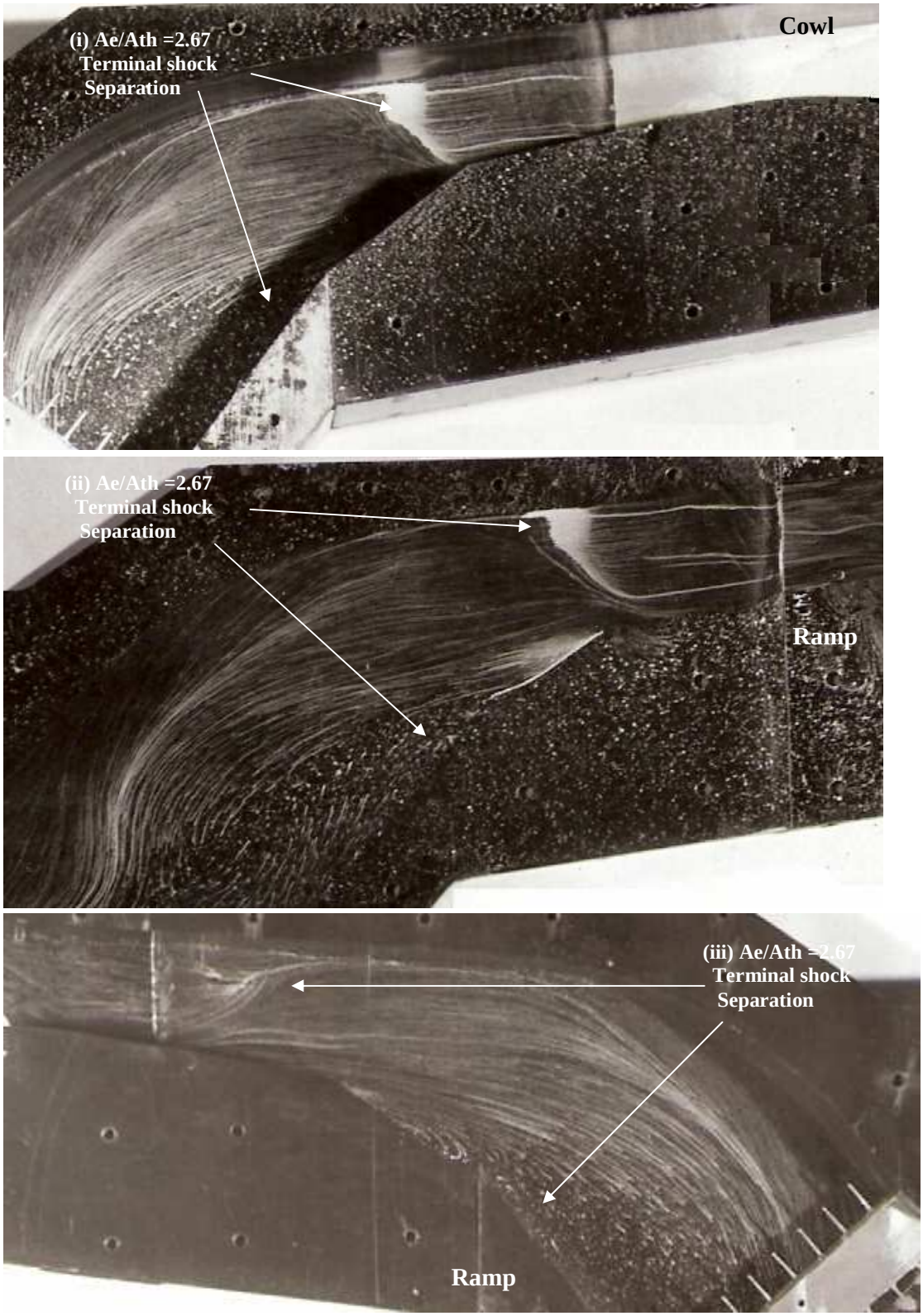

Fig. 7.19c : Surface oil flow patterns on side-plate M = 2.5, Mach 3 Ramp

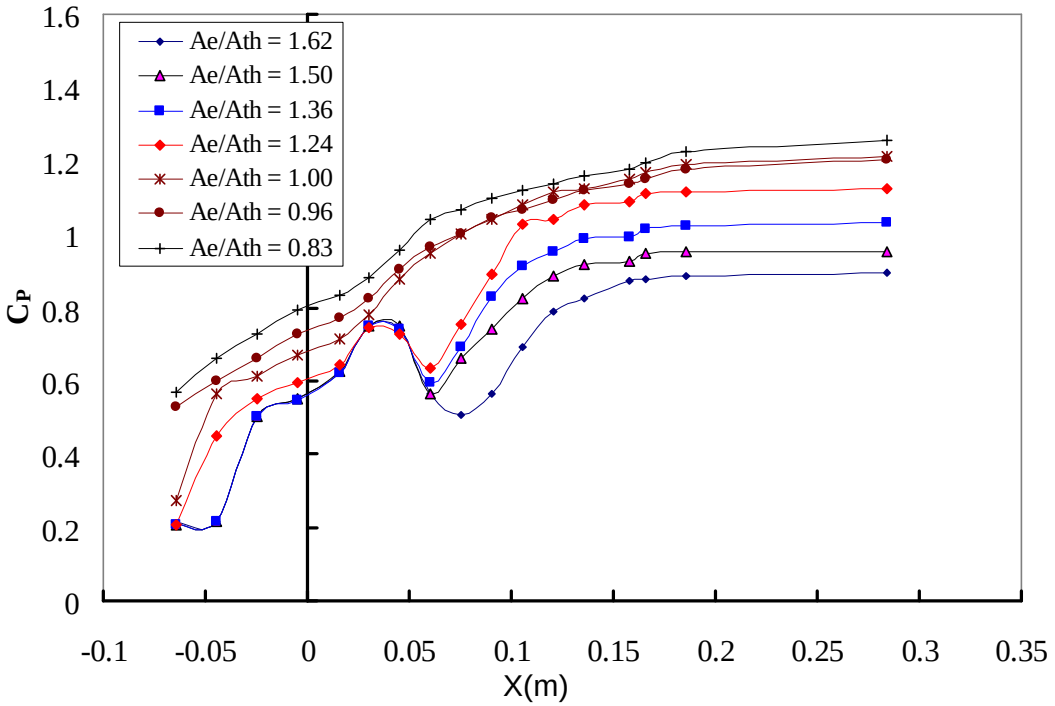

Fig. 7.20a: Pressure distribution on ramp center line, M = 2.0

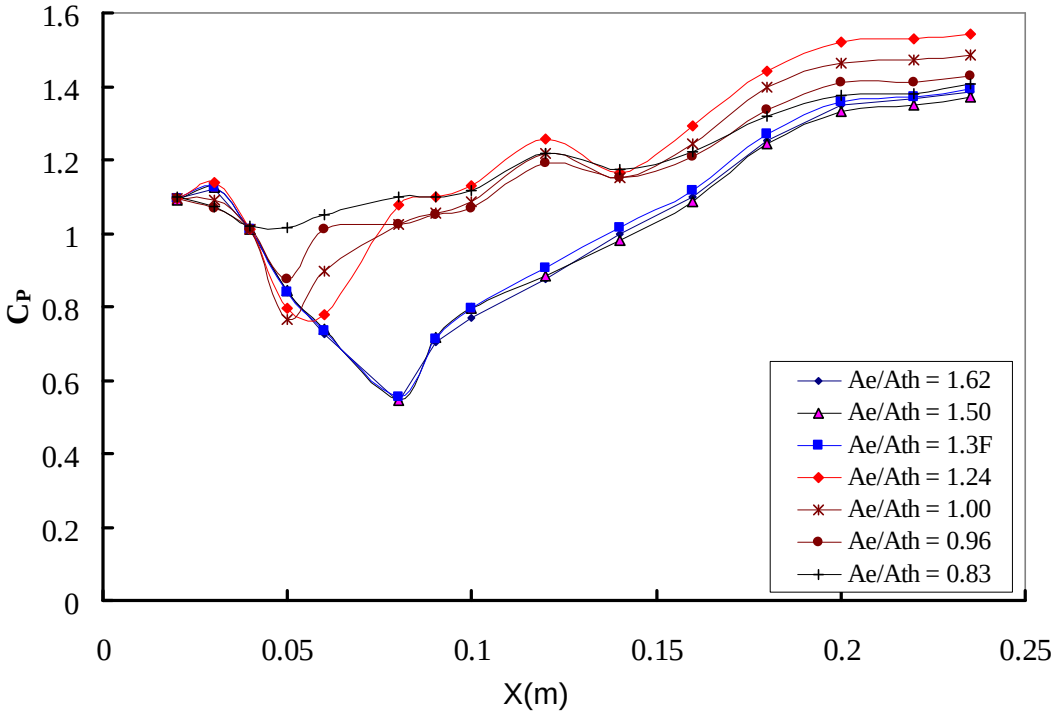

Fig. 7.20b: Pressure distribution on cowl center line, M = 2.0

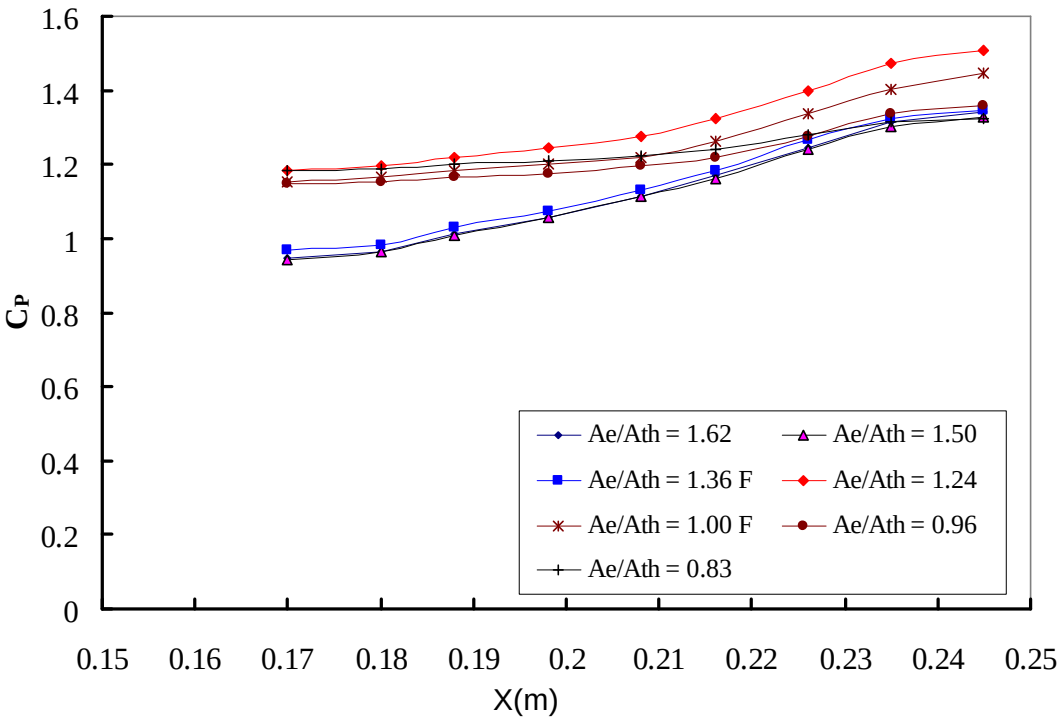

Fig. 7.20c: Pressure distribution onside-plate, M = 2.0

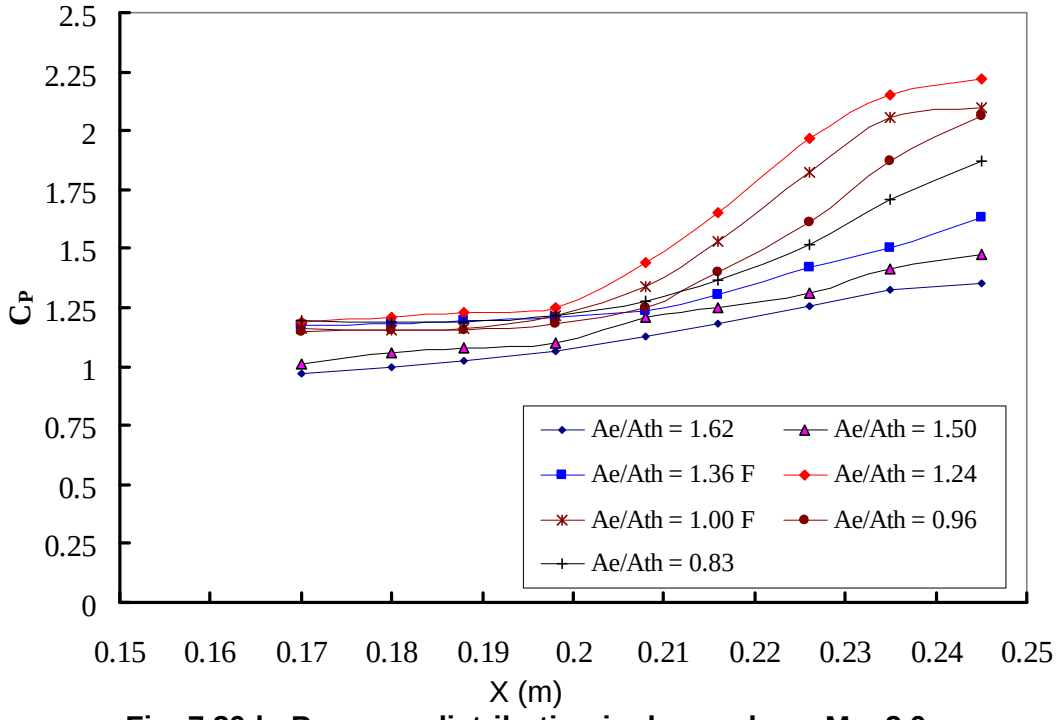

Fig. 7.20d: Pressure distribution in dump-plane, M = 2.0

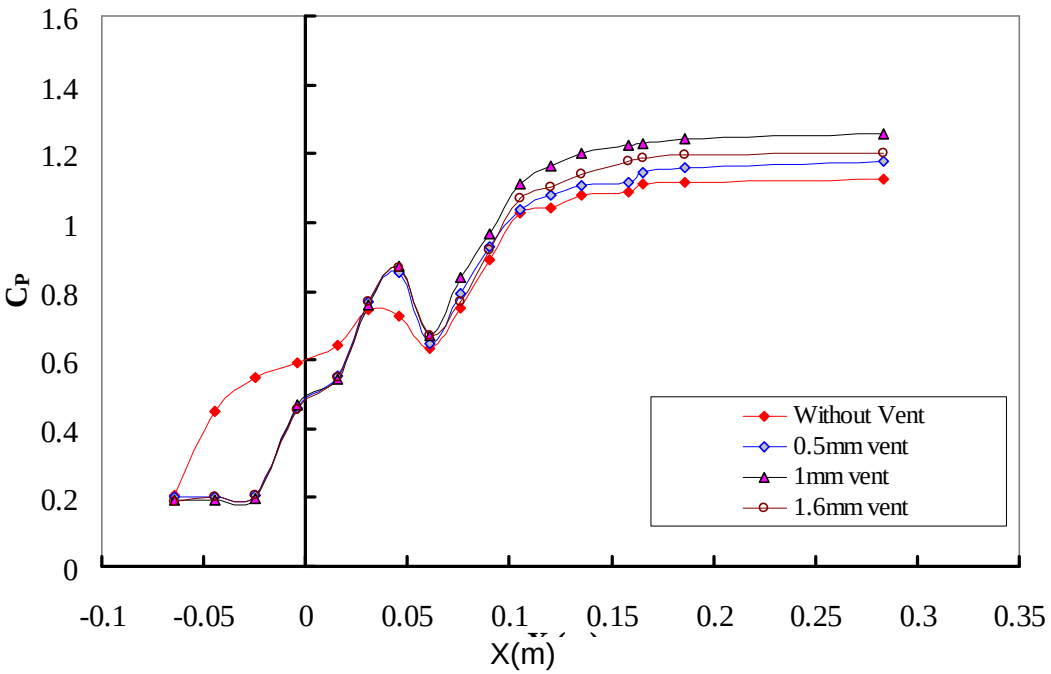

Fig. 7.21a: Effect of ventilation on ramp pressure distribution, A_e/A_{th} = 1.24, M = 2

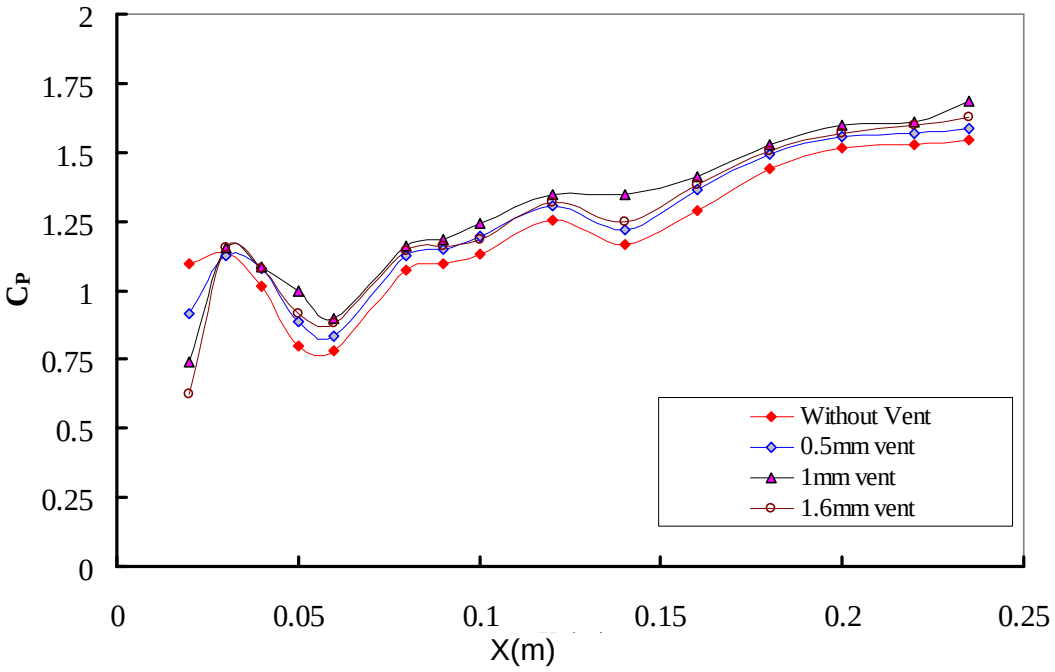

Fig. 7.21b: Effect of ventilation on cowl pressure distribution, A_e/A_{th} = 1.24, M = 2

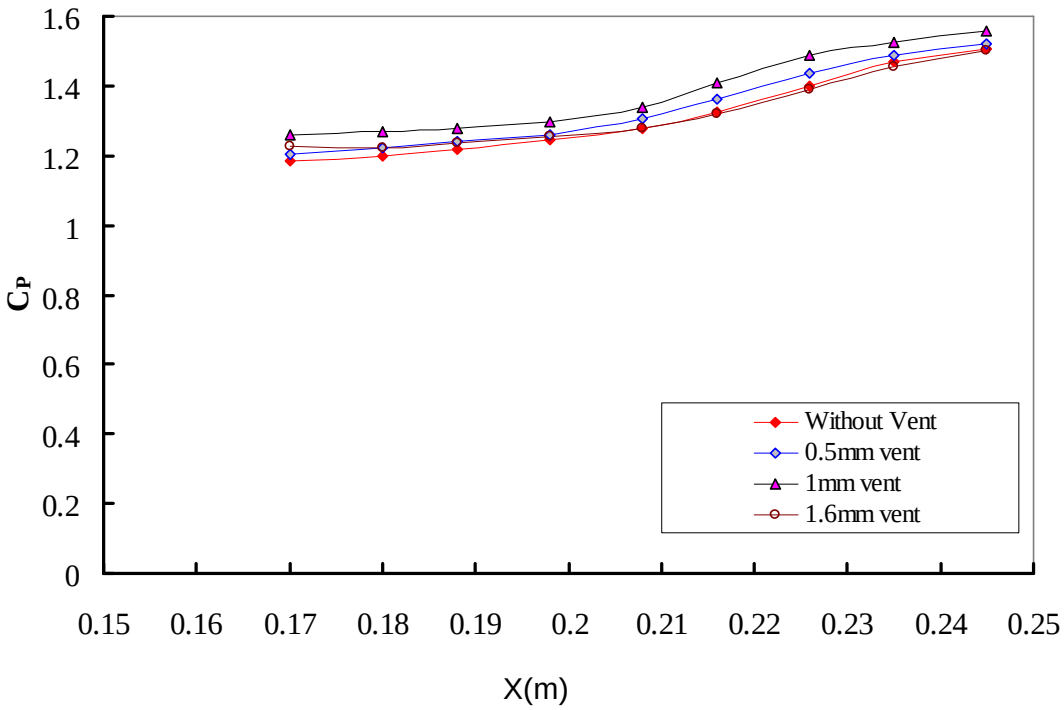

Fig. 7.21c: Effect of ventilation on side-plate pressure distribution, A_e/A_{th} = 1.24, M = 2

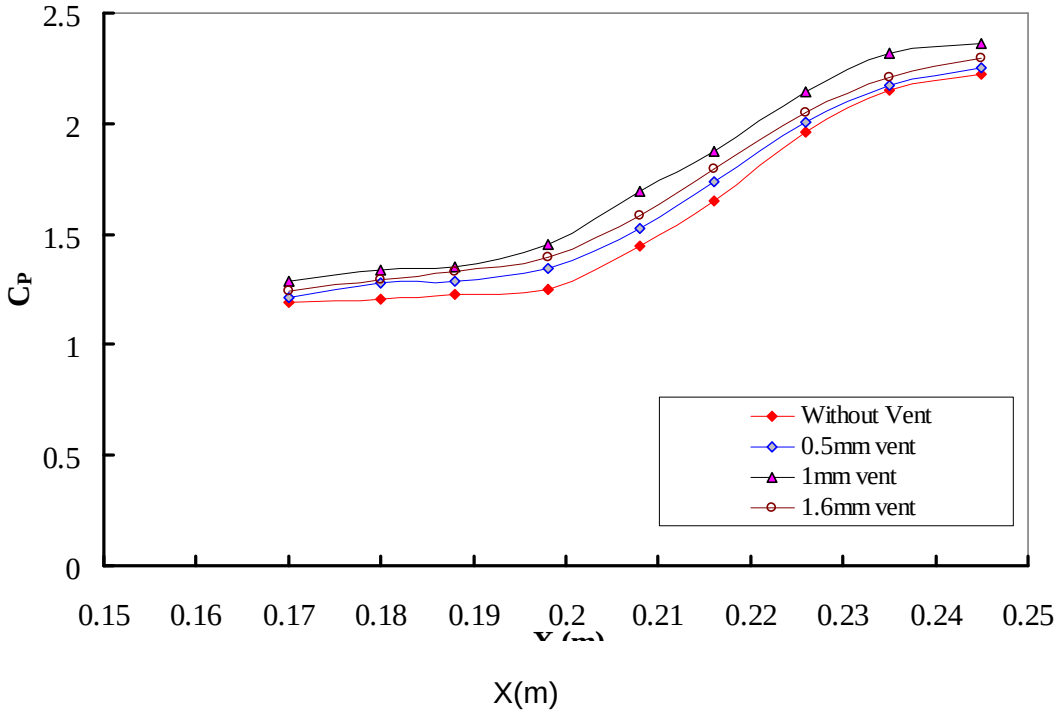

Fig. 7.21d: Effect of ventilation in dump-plane pressure distribution, A_e/A_{th} = 1.24, M = 2

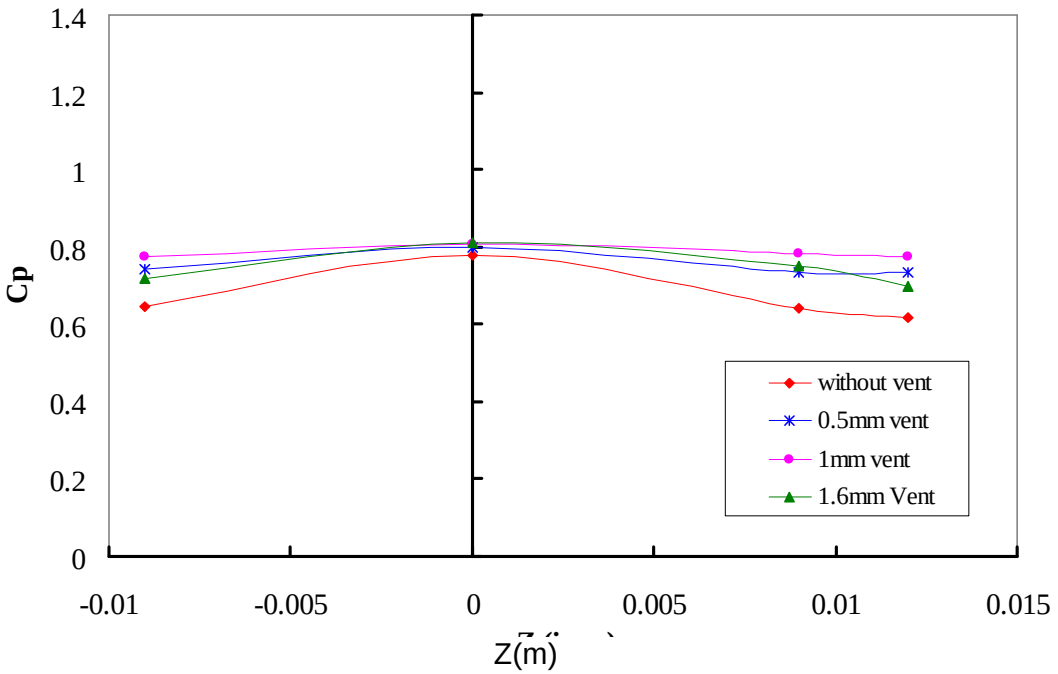

Fig. 7.21e: Pressure distribution across the ramp surface at X = 0.0455m for various vent gap, A_e/A_{th} = 1.24, M = 2

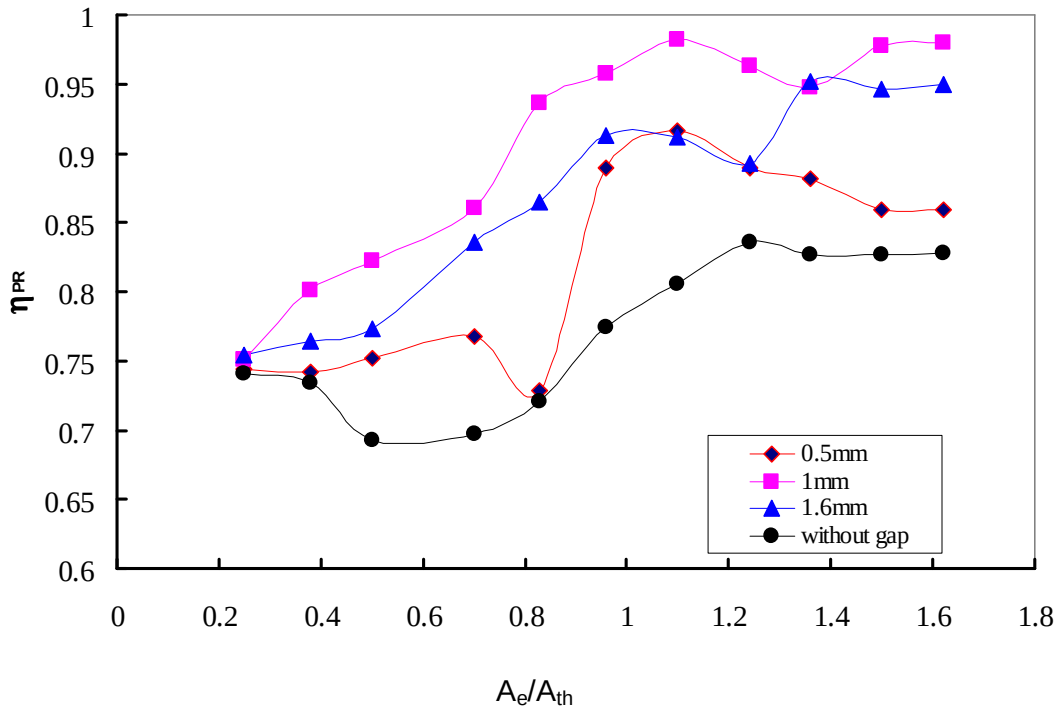

Fig. 7.21f: Effect of ventilation on pressure recovery efficiency vs area ratio, M = 2

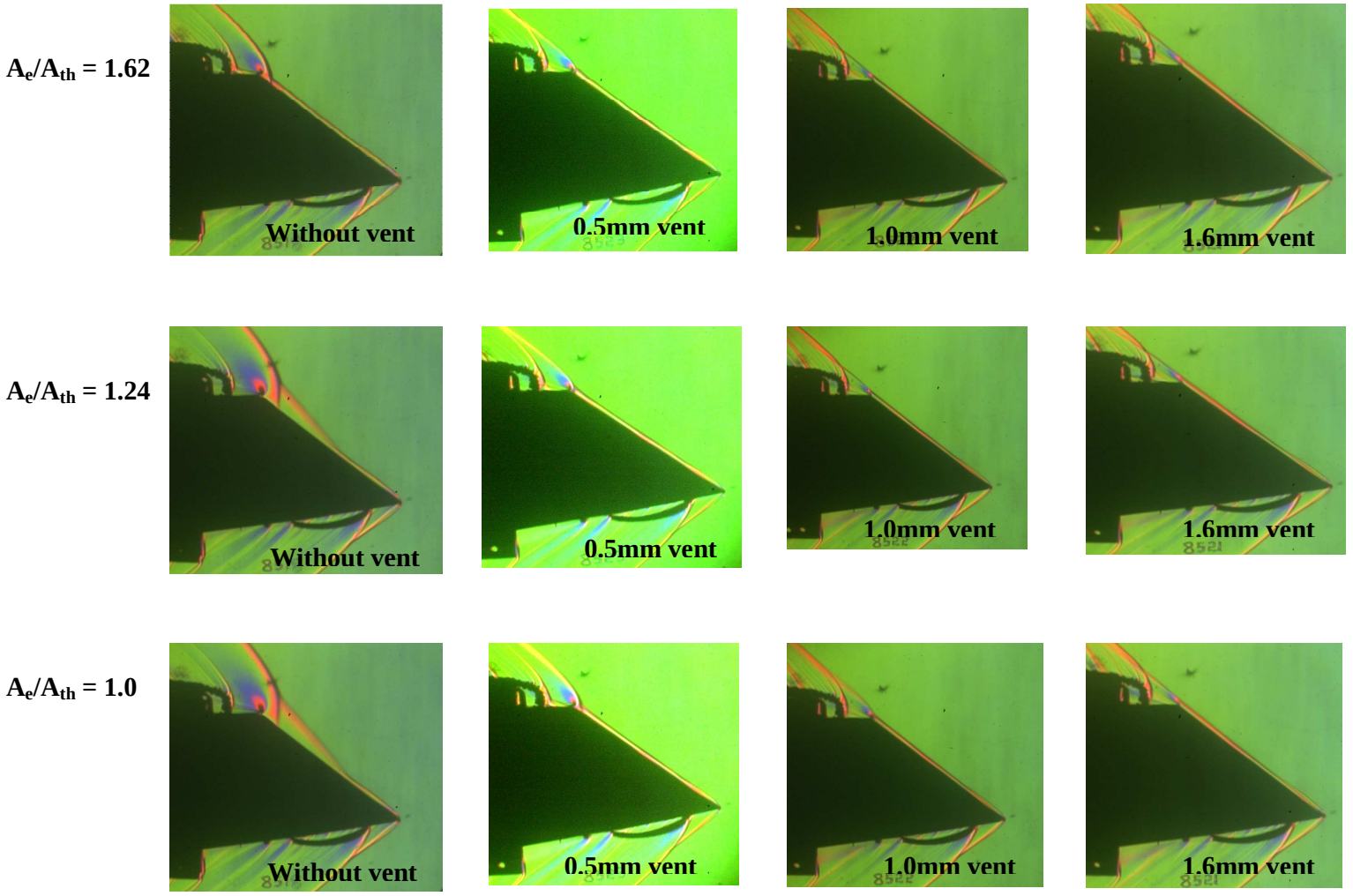

Fig. 7.22: Effectiveness of various vent gaps in controlling the intake flow, M = 2.0

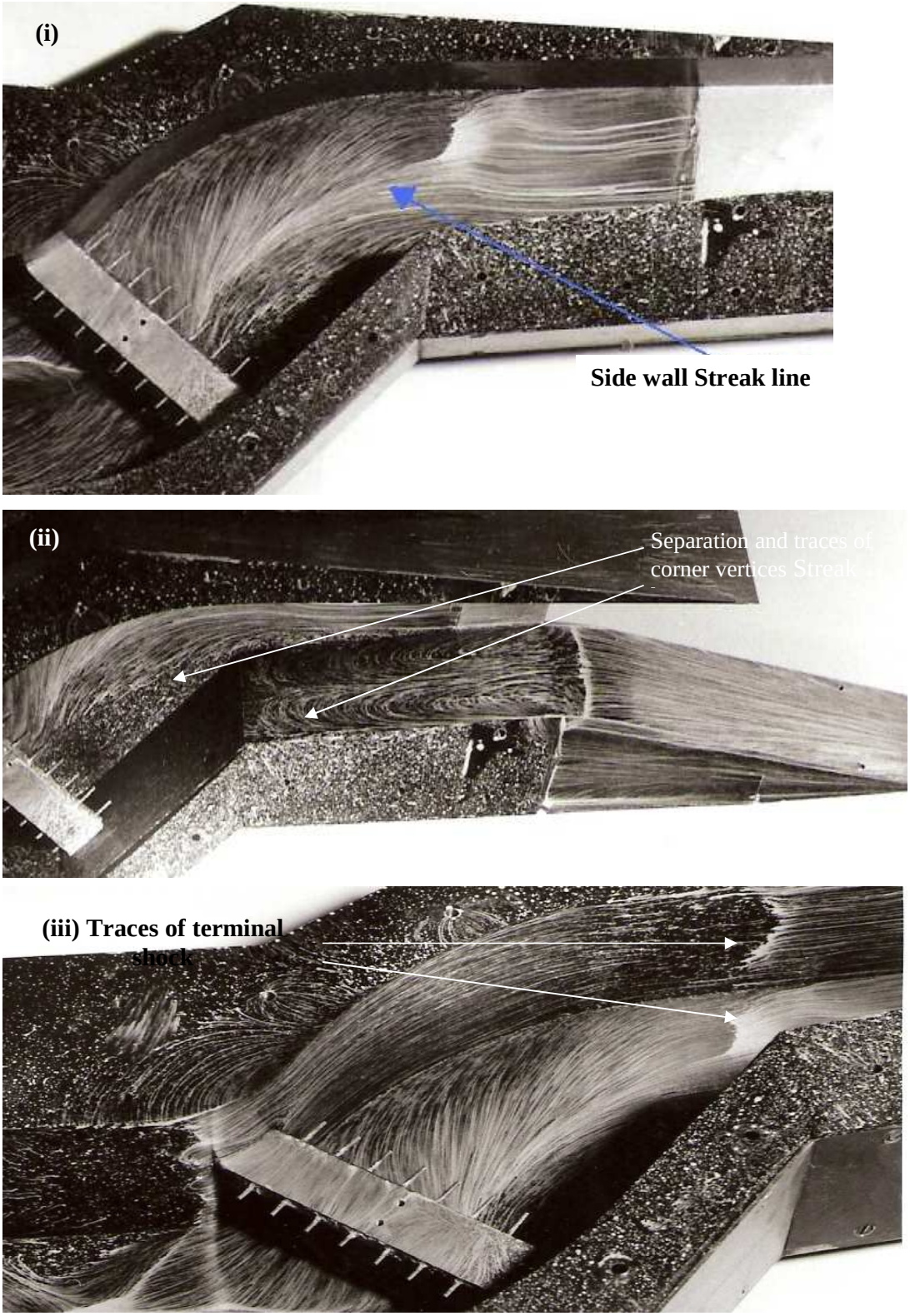

Fig. 7.23a: Surface flow patterns at M = 2.0; Mach 2 ramp; A_e/A_{th} =1.77

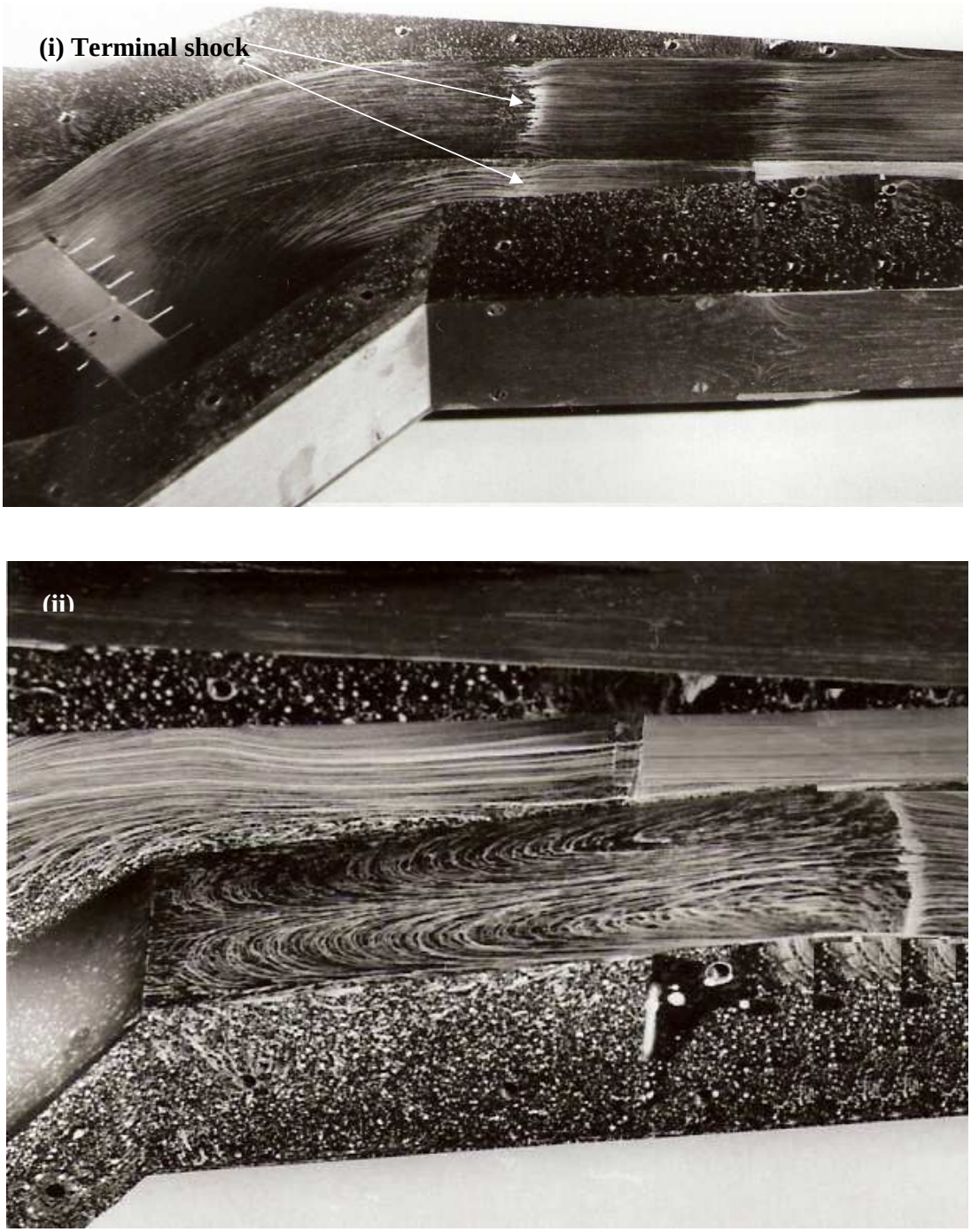

Fig. 7.23b: Surface flow patterns at M = 2.0, Mach 2 ramp; A_e/A_{th} =1.59

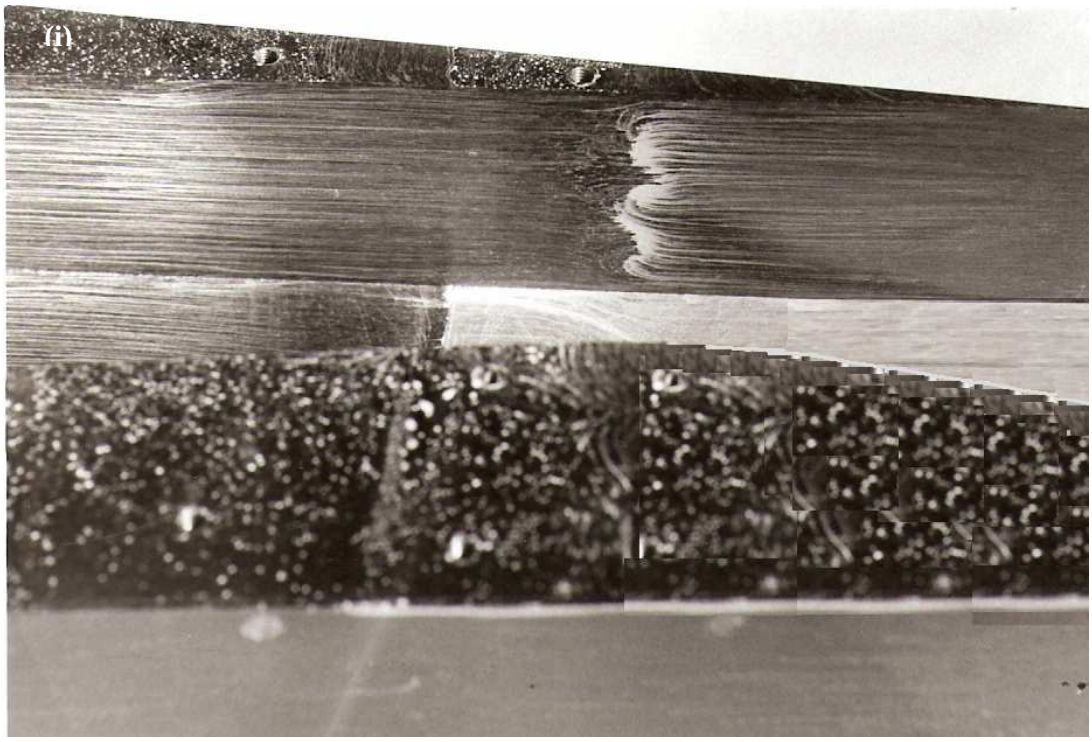

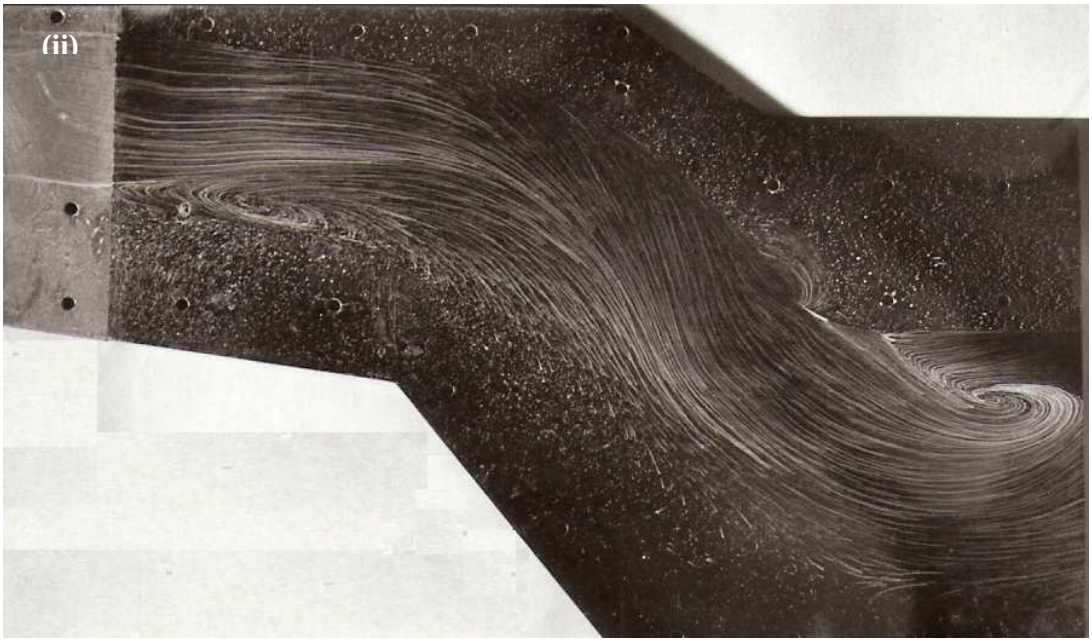

Fig. 7.23c: Surface flow patterns at M = 2.0, Mach 2 ramp; A_e/A_{th} = 1.45

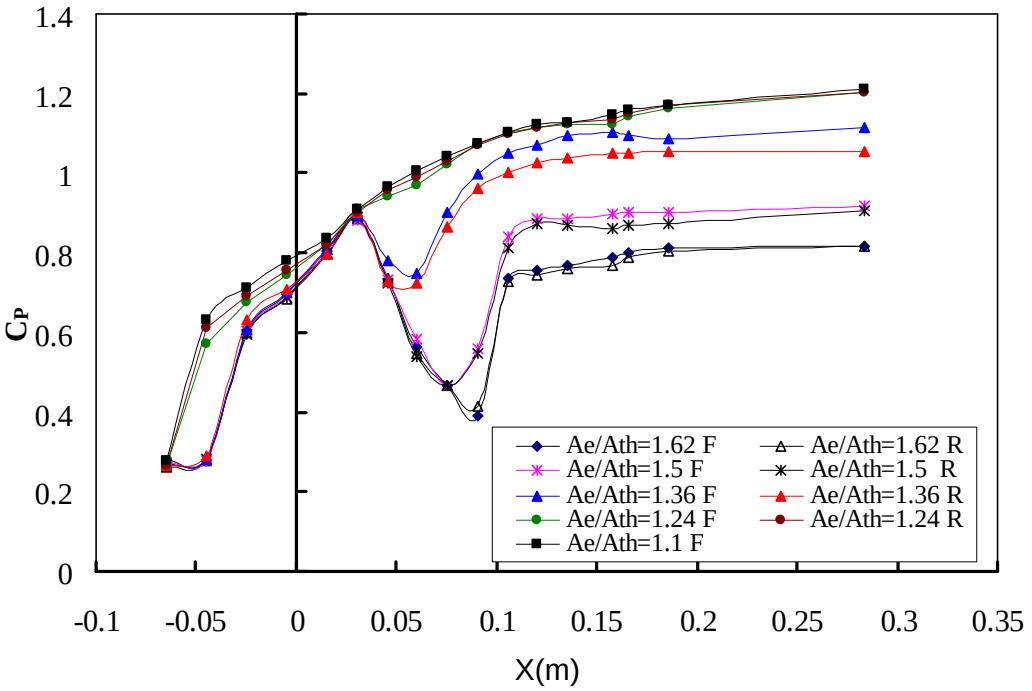

Fig. 7.24a: Pressure distribution on ramp center line, M = 1.8

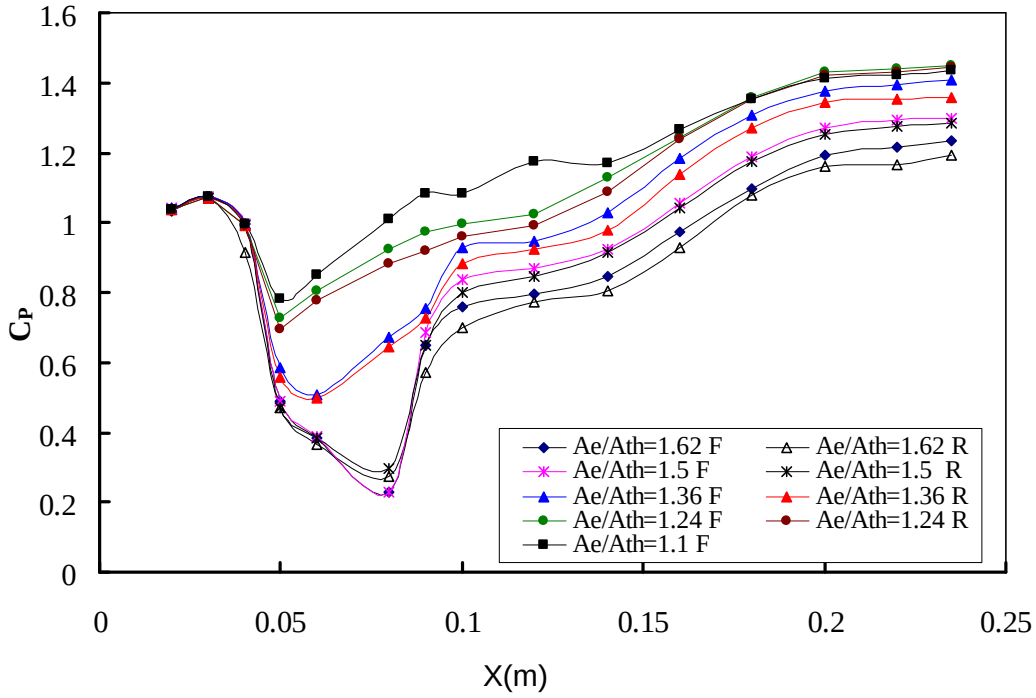

Fig. 7.24b: Pressure distribution on cowl center line, M = 1.8

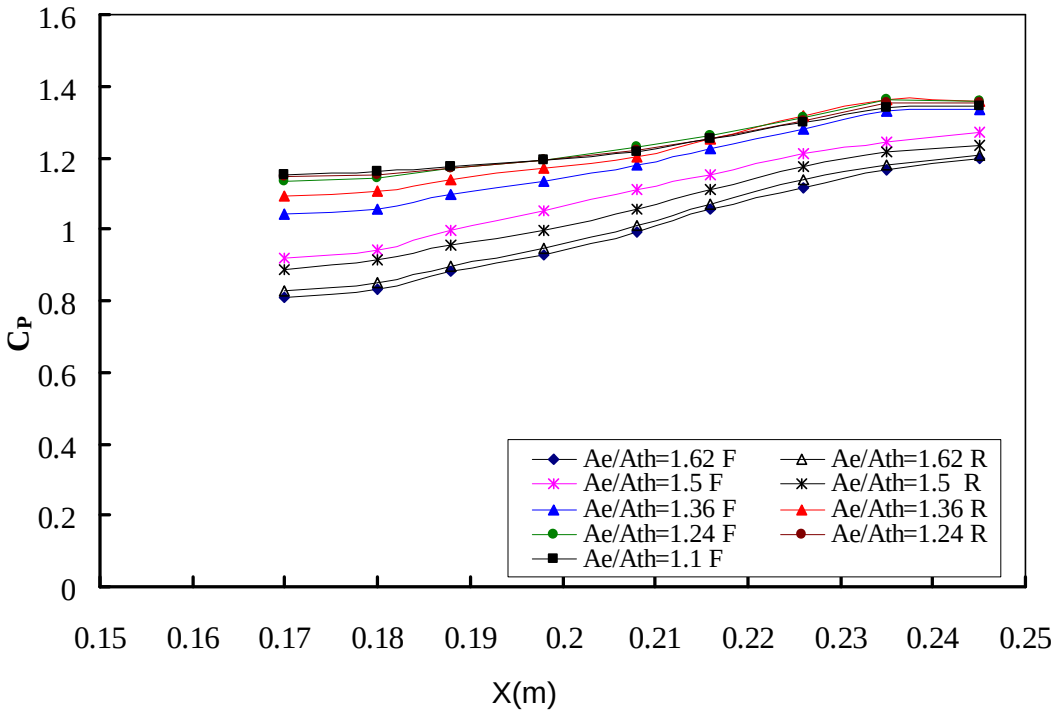

Fig. 7.24c: Pressure distribution on side-plate, M = 1.8

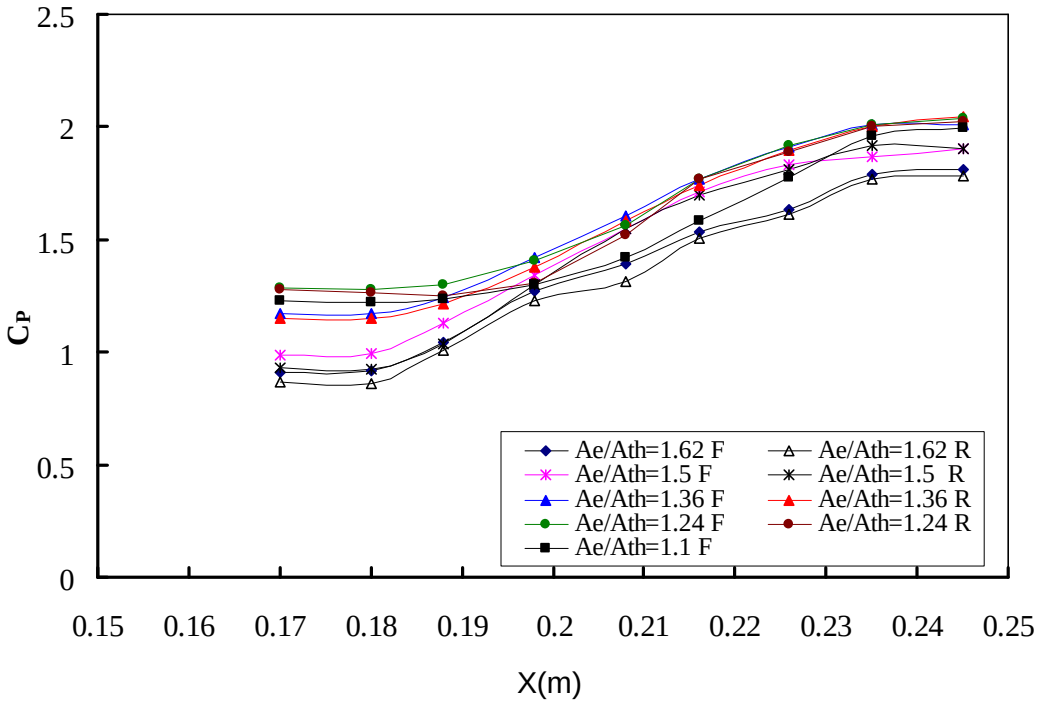

Fig. 7.24d: Pressure distribution in dump-plane, M = 1.8

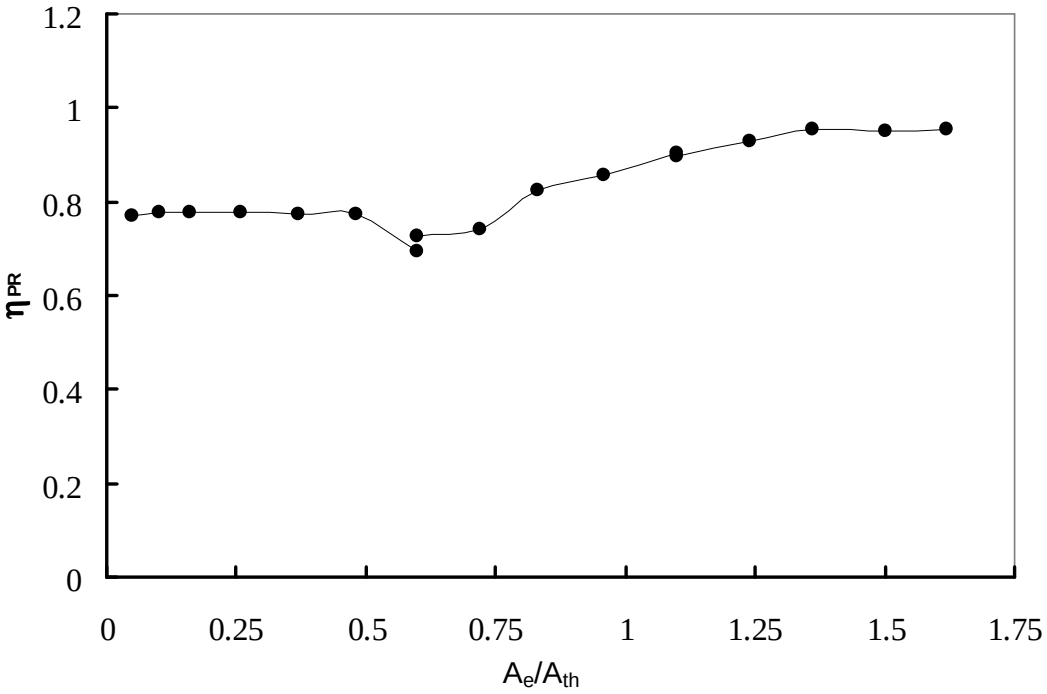

Fig. 7.24e: Efficiency of pressure recovery vs area ratio, M = 1.8

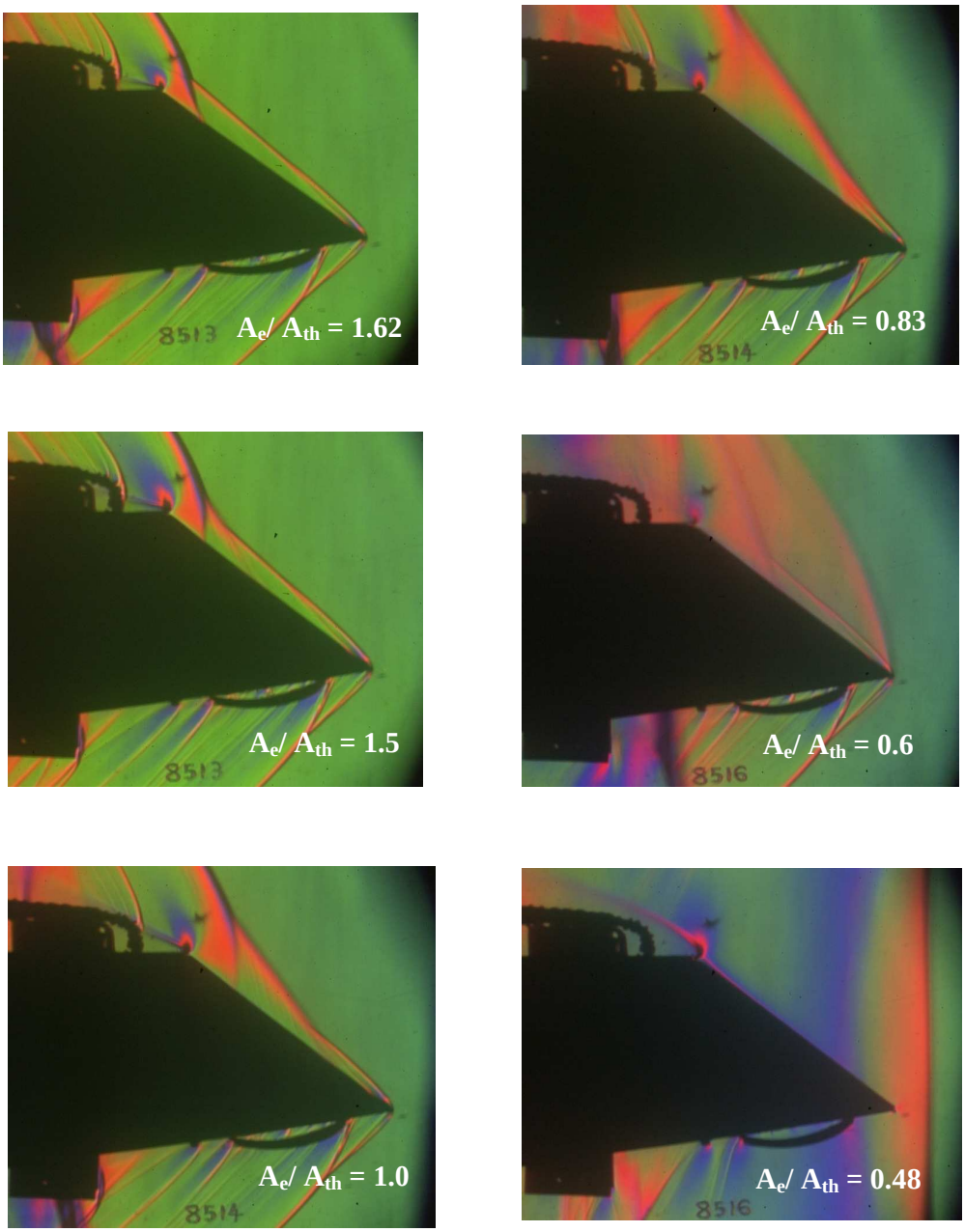

Fig. 7.25: Flow visualization for various area ratios, M = 1.8

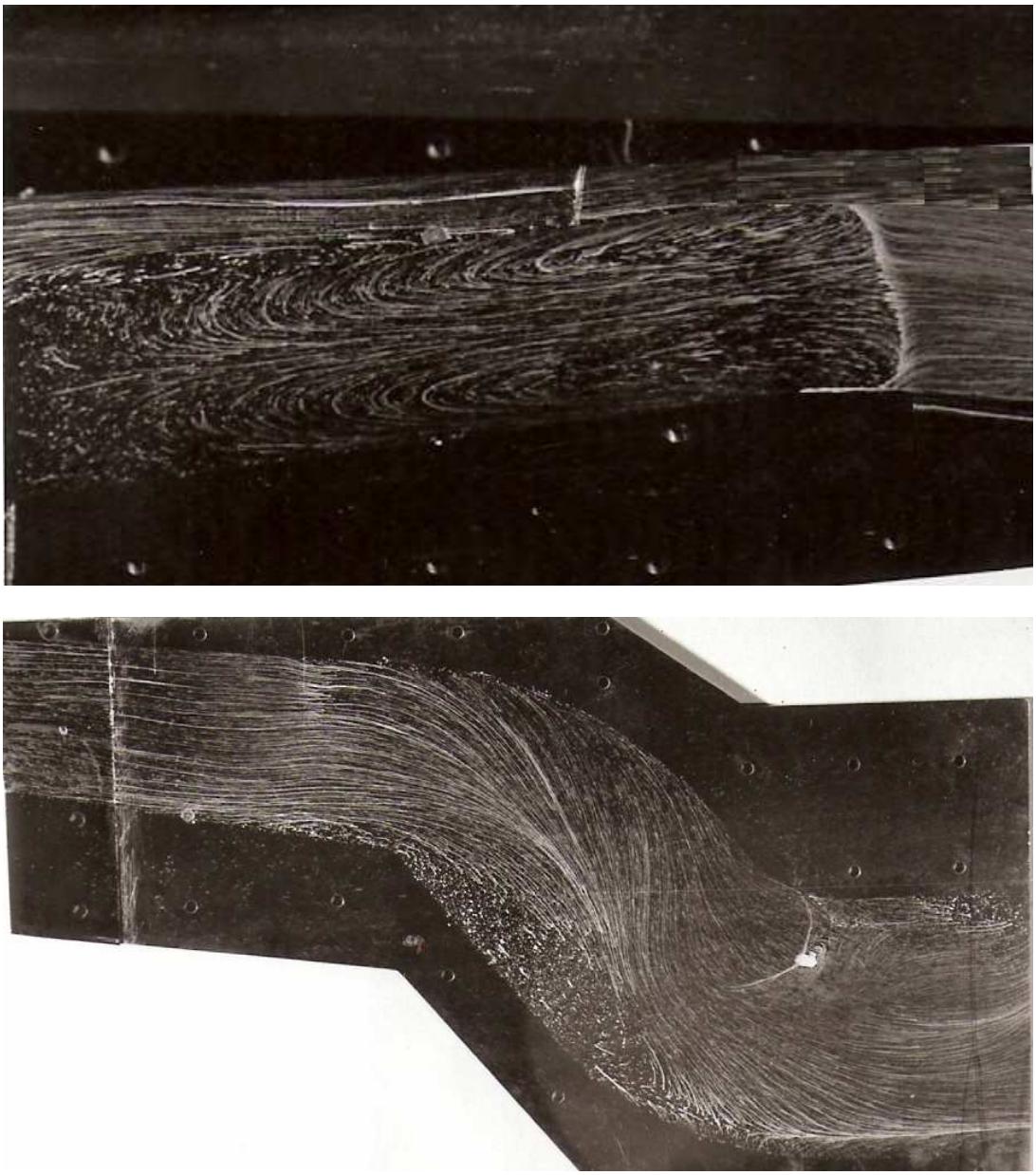

Fig. 7.26a: Surface flow patterns at M = 1.8, Mach 2 ramp; A_e/A_{th} =1.59

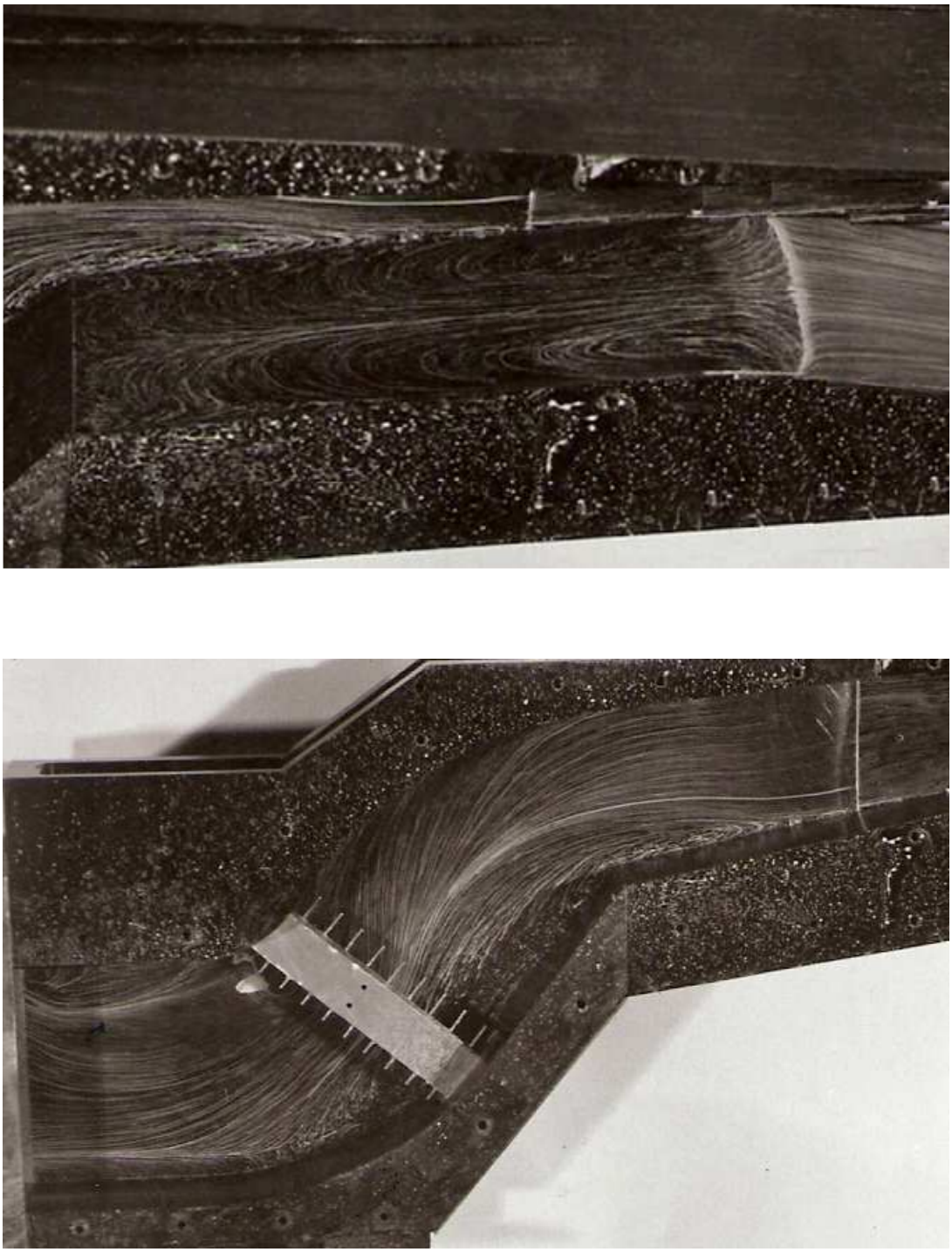

Fig. 7.26b: Surface flow patterns at M = 1.8, Mach 2 ramp; A_e/A_{th} =1.32

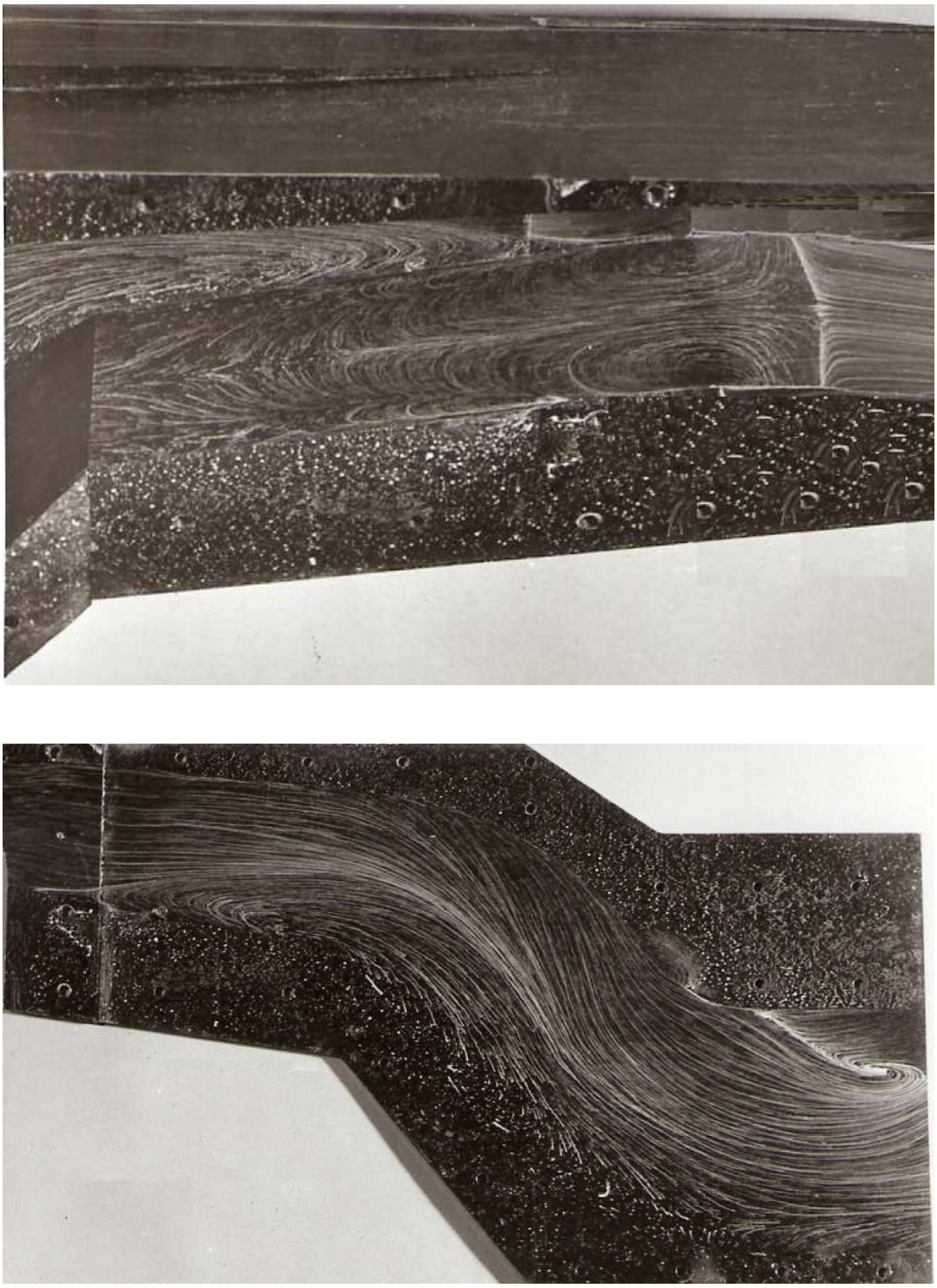

Fig. 7.26c: Surface flow patterns at M = 1.8; Mach 2 Ramp; A_e/A_{th} =1.06

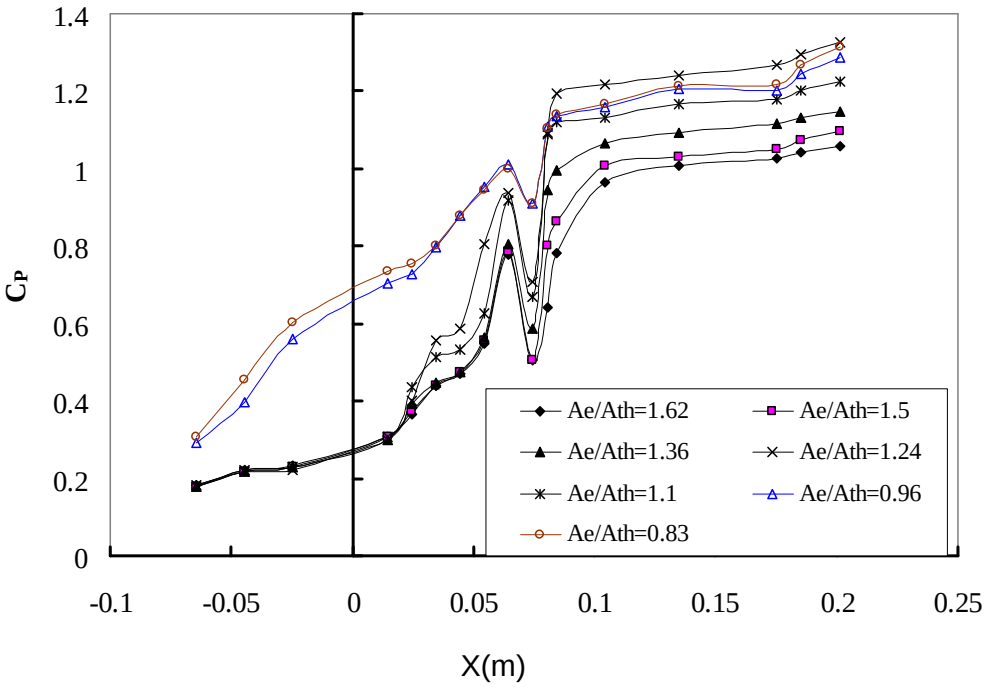

Fig. 7.27a: Pressure distribution on ramp, M = 2.5, Mach 2 Ramp

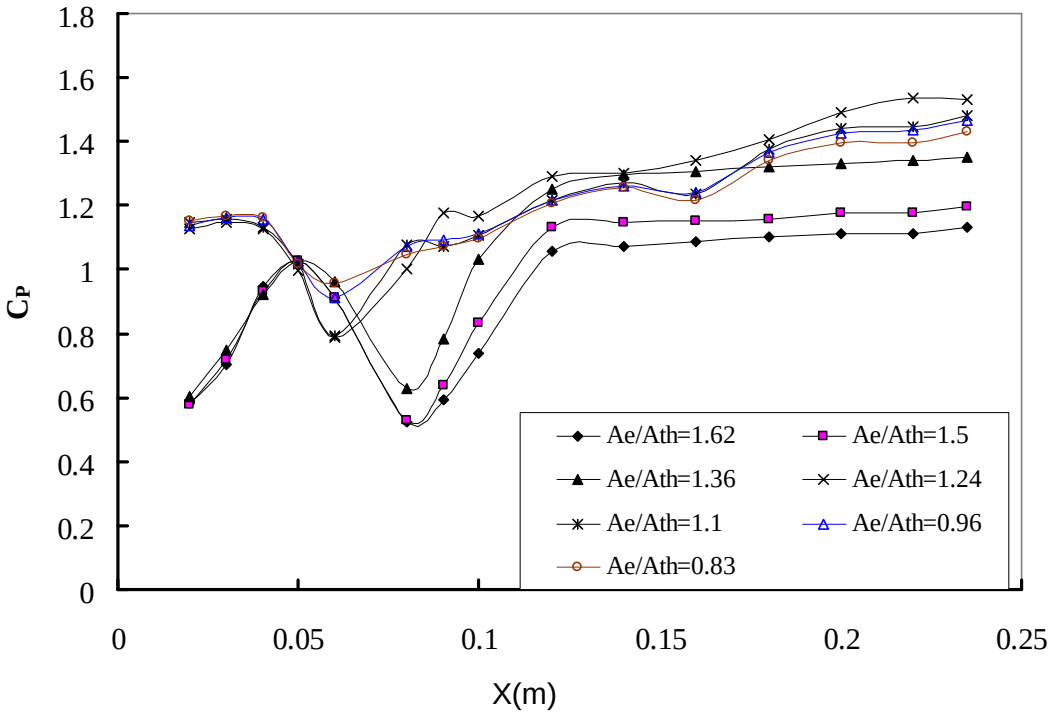

Fig. 7.27b: Pressure distribution on cowl, M = 2.5, Mach 2 Ramp

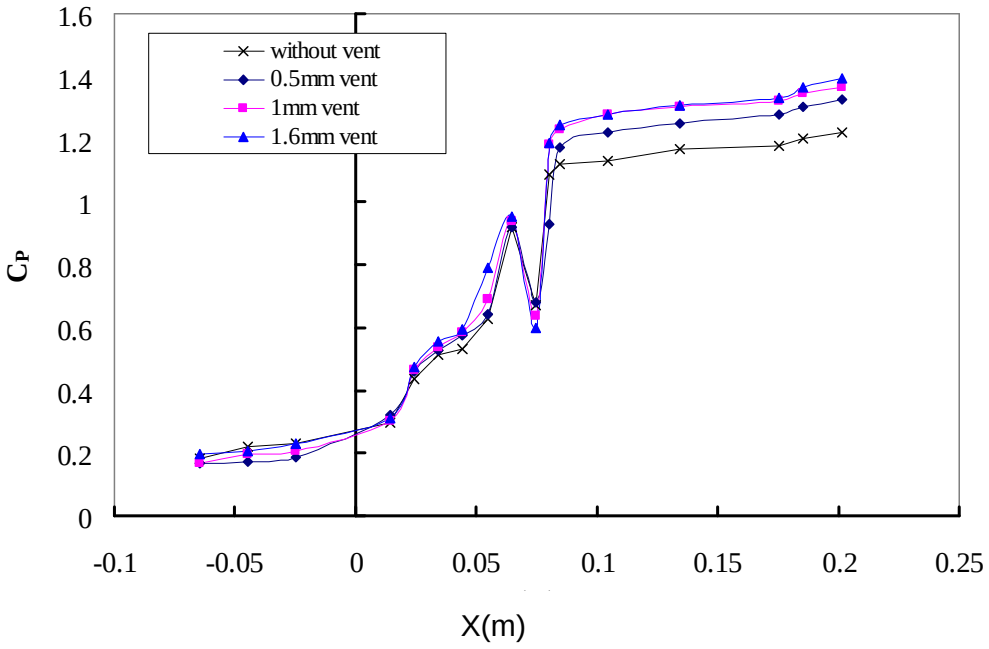

Fig. 7.27c: Pressure distribution on ramp with vent, M = 2.5, A_e/A_{th} = 1.1

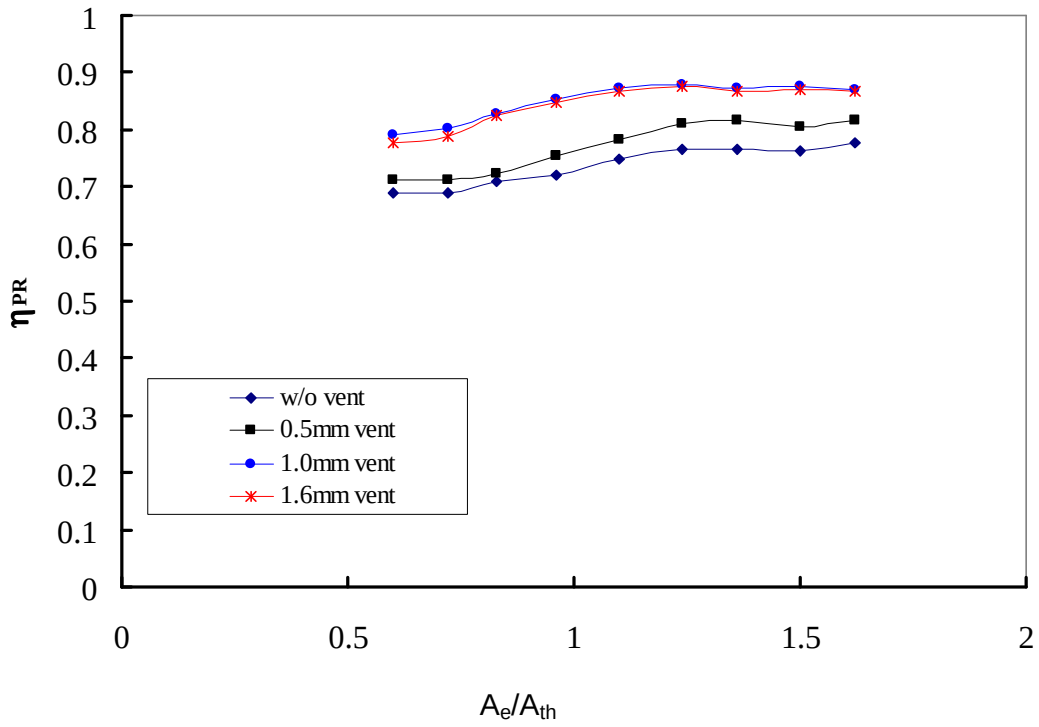

Fig. 7.27d: Efficiency of pressure recovery, M = 2.5

Documentation Sheet

National Aerospace Laboratories	**Class Unrestricted**
	No. of copies *15*

Title	Effect of natural ventilation of internal boundary layer on the flows Characteristics of a Supersonic Air-intake
***Author(s)* :**	**Ritu Kanchan Dubey, Dr. G. K. Suryanarayana**

Division	**NTAF**	***NAL Project No.***	N-8-496
Document No.	TM-NT-0110	***Date of issue***	June 2010

Contents:	91	Pages	103	Figures	08	Tables	9	References

External Participation ***- NIL***

Sponsor- NAL, Bangalore

Approval - Head, NTAF

Remarks ***- Nil***

Keywords **-** Supersonic air-intakes, Buzz, Boundary layer control

Abstract.

Experiments were carried out on the model of an isolated supersonic air-intake to study the effect of natural ventilation of the internal boundary layer on the overall pressure distribution, total pressure recovery, intake buzz oscillations and surface-flow patterns in the Mach number range of 2 to 3 at design and off-design conditions. The intake was stared in supercritical condition with benign back-pressure condition; the back-pressure was gradually increased using a butterfly valve driven by a PC-controlled stepper motor. The tests were carried out at the 0.3m supersonic blowdown wind tunnel at the Experimental Aerodynamics Division, NAL, Bangalore. The results show that with ventilation, significant improvement in the total pressure recovery occurs at all back-pressure conditions, with the optimum vent gap of 1.6mm indicating improvement in the pressure recovery efficiency from about 60% to 90% at Mach 3; improvement was observed at Mach 2 also, though of reduced magnitude. Schlieren visualizations suggest a clear delay in the occurrence of critical condition of the intake. Ventilation created a stable oblique shock at the intake cowl lip, in contrast to the bow-wave without ventilation, indicating reduced spillage and improved pressure recovery of the entry flow. Image analyses of video pictures suggest a limit-cycle oscillation of the oblique shock just past the critical region. Numerical simulation for some selected cases was carried out with and without ventilation using a CFD code FLUENT. Reasonable agreement with the experimental data was observed.

Distribution

Copy No.	1 to 2	: Head & Dy. Head
	3 to 6	: Sponsors / Coordinator
	7 to 8	: Author(s)
	9 to 16	: Project Office